SUPERGLASS DYNAMICS OF SOLID HELIUM

A Dissertation

Presented to the Faculty of the Graduate School

of Cornell University

in Partial Fulfillment of the Requirements for the Degree of

Doctor of Philosophy

by

Ethan Jesse Pratt

February 2010

SUPERGLASS DYNAMICS OF SOLID HELIUM

Ethan Jesse Pratt, Ph.D.

Cornell University 2010

Although solid ^{4}He may be a supersolid, it also exhibits many phenomena unexpected in that context. In order to measure the finely resolved time-dependent inertial response of this exotic quantum material, we constructed a vibrationally-isolated millikelvin cryostat with automated data acquisition and temperature control, and used a high-dynamic range DC-SQUID-based displacement sensor to detect its rotational susceptibility.

We observed ultra-slow evolution towards equilibrium of the relaxation dynamics in the resonance frequency $f\,(T)$ and dissipation $D\,(T)$ of the oscillator with the appearance of the 'supersolid' state at low shear velocity v. One possibility is that such amorphous solid ^{4}He represents a new form of supersolid in which glassy dynamical excitations within the solid control the superfluid phase stiffness, with the microscopic nature of those excitations yet to be conclusively observed.

Within driven materials, high shear agitation (or velocity v) tends to inject energy into dissipative motion and reduces the amount of heat required to equivalently agitate the system, with exquisite dependence on the microscopic physics that remain unknown in ^{4}He . We therefore observed the effect of increased shear agitation as a concurrent decrease in the thermal activation necessary to disrupt the putative supersolid.

To measure this disruption, we developed a new free-inertial-decay technique, mapping out the entire velocity-temperature "phase diagram" for rotat-

ing solid ^{4}He, and precisely observed the connection between shear agitation and temperature as the critical contour on the surface $f(v,T)$. We find that shear agitation acts indistinguishably from temperature within this material, an observation which strongly suggests that the microscopic excitations controlling the supersolid transition are in a jammed, glassy, "effective temperature" state. Furthermore, we observed power-law relaxation times in the material, which indicates the presence of a broad glassy distribution of microscopic excitations.

The fundamental open question about this material is whether a true superfluid component - associated with the anomalies in $f(v,T)$ and $D(v,T)$ - exists within it or not. Since torsion oscillators are not able to probe the possible DC flow of such a component, we have developed a new class of devices designed to directly generate and measure the flow of nanoporous liquid supercurrents through solid ^{4}He microcrystals.

BIOGRAPHICAL SKETCH

Ethan was born in Anaheim, California and grew up in Orange County. He graduated from El Toro High School in 1998, and entered Cal Poly, San Luis Obispo that fall as a mechanical engineering major, switching to physics in 2001 and graduating with a B.S. in 2003.

He worked rather obsessively on a 1967 Camaro in high school and early college, making a large number of experimental gasket-related mistakes in the process - which, in the end, proved to make the 327 engine only marginally operable (although it did run once at 130 MPH along the 101 freeway near Carpinteria) and finally ejected a pushrod through the wall of the #2 cylinder. Overall, the mostly constant mechanical defeat was an excellent mental training exercise for grad school, where entirely different types of mistakes were vigorously pursued, but hopelessness was mostly avoided.

He worked on stress relaxation dynamics in sheared wet foams as an REU student in Mike Dennin's group at UC Irvine during the summer of 2002, and joined the complex systems group of Eberhard Bodenschatz upon arrival at Cornell in Spring 2003.

Eberhard moved his group to Germany shortly thereafter, and a position opened up in the recently relocated (from Berkeley to Ithaca) group of Séamus Davis. After some initial work on a proposal to build a superfluid ^{4}He Josephson-junction qubit, the first widely reported talk on the new supersolid effect was delivered by Moses Chan at Cornell in the fall of 2003, and Ethan switched focus to study the new effects. He received a master's degree in physics from Cornell in January 2009 after finally taking an A-exam.

ACKNOWLEDGEMENTS

I'm thrilled to have gotten the chance to work closely with Séamus for several years, replete with many dozens of intense and long-running discussions that cumulatively added up to a large part of a generally treasured intellectual life at Cornell, and which were invaluable training. The intensity of his focus on only the most important questions reflects a scientific way of life I hope to emulate, and the literally tremendous, well-planned facilities in the A-wing are going to be missed.

Joan Hoffmann was my first mentor in the ways of making things cold, and is also a friend I hope to never need to repay for taking me to the emergency room and hanging out when my eyebrow was abruptly opened by a falling dewar late at night many years ago.

Minoru Yamashita is an experimentalist of forbidding productivity and precision, who designed and built a beautiful oscillator and rotating cryostat that he left in our hands, along with a collection of wise sayings in our lab notebooks that never failed to be inspire. "Do first, think later!"

In turn, I'm happy to see the cryostat turned over to Vikram Gadagkar and Sourin Mukhopadhyay, with Neal Harrington assisting in the imminent start of what promises to be several more high-impact years of literally solid results.

Eric Hickok, Dave Reese and Caroll Moya made my years at Cal Poly one and a half barrels of fun, and today they remain most of a barrelfull.

I enjoyed spending a few months harassing an impressionable Mohammad Hamidian before he was a master of all things heavy and fermi, but was just as glad to later know him as a friend who is unfailingly selfless. I also maintained anthropological contact with the far-flung corners of the Davis group: Andy Schmidt, Jacob Alldredge, Jinho Lee, Tien-Ming Chuang, and Milan Al-

lan never ceased to amuse during late-night lab shifts, and remain friends and collaborators. Also, I still owe Andy a ride to the Syracuse airport.

Arend van der Zande, Mark Buckley, Robert Rodriguez and Ellen Kong, Ali Schmidt, and Albert Bae made the first couple years of Ithaca bearable, while Mike Schuetz and Nate and Adriana Thomas made Orange County feel like home again when I returned for a few months, and Sophie McGough and I grew up together.

As for non-physicist friends from Ithaca, Pooneh Bagher and Sarah States are amazing and irreplaceable, though I usually tell them that they're not and that I'm looking. The Lincoln-street crew (which is less intimidating and accurate than it sounds) of Joe Kirtland, Jay Schweig, Steve Morris, Kioni Cho, Viviana Ruiz, James and Abby Mandel and Scott Verbridge made weeknights worth leaving lab - for poker, beer, parties, and general piano-moving shenanigans.

Within the supersolid community, I was lucky to have frequent updates and helpful hints from John Reppy in the supersolid lab several hallways over. Our fiery theorist collaborators Sasha Balatsky and Matthias Graf are great fun to talk to, and I always look forward to seeing John Beamish, John Saunders, Alan Dorsey, Moses Chan, Keiya Shirahama, Harry Kojima, Eunseong Kim, Massimo Boninsegni, and Jason Ho at conferences.

Eric Smith heroically liquefied our precious dewary fluids, and was an extremely knowledgeable resource of cryogenic techniques. Stan, Jeff and Chris in the machine shop built our most painstaking parts without (genuine) complaints, and were always willing to talk about designs.

Andy Mackenzie delivered priceless insights into physics as a career, and interesting perspectives from outside Cornell, and I really enjoyed hiking with him in Ithaca and drinking with him in England.

My parents have been a source of solid support as long as I've been in school - which is a long time - and they are mostly responsible for teaching me to try to communicate well in words and diagrams, a tendency for which I'm grateful. Noah and Sandy Pratt started a lively family that I looked forward to going home to when I had the chance, along with my grandparents, Bubbie and P-pop, who always knew when to duck.

Erich Mueller made cold atomic vapors the most interesting class I took at Cornell, and was ever eager to discuss data or theory with equal interest.

Jeevak Parpia let me live in his lab while I tried with mixed results to fix dilution refrigerators, and I really appreciate the collaboration. I learned a huge amount of vacuum techniques and gained years of troubleshooting wisdom, and could always count on his reassuring blend of sanguine humor during equipment failures.

Sarah Cowan attempted even as long ago as our undergraduate days to precaution me against following strange sleeping schedules, including helpful diagrams to avoid accidentally smothering myself with a pillow or using it for x-ray spectroscopy. These warnings were often unheeded in grad school, and she subsequently endured the many days and nights during which I generated figures and wrote this document. She glows with my deep love and hope, and sometimes with planktonic fluorescence from a predominantly sushi diet.

Finally, I benefited from an extremely close collaboration - and personal friendship with - Ben Hunt, who contributed substantially to virtually everything in this dissertation. Who could forget (much less navigate) the collaborative albatross of a Lab-VIEW control program we wrote to handle the ringdowns... who could remember the names and codependencies of the extended albatrossian family of Matlab scriptlings we swapped back and forth to process

data and generate figures? Hacking out strategic goals with Ben involved the most interesting scientific arguments I ever had at Cornell, and the couple of days on which we discovered real bits of new physics were the most fun. I hope to have a project worth another collaboration with Ben in the future, but can count on making Canadian currency jokes without cessation regardless of our professional paths or the exchange rate. Also - I haven't read his dissertation, and if you haven't either, I assume that it is the place to start.

CONTENTS

LIST OF TABLES

LIST OF FIGURES

CHAPTER 1

MACROSCOPIC QUANTUM PHENOMENA

Bose-Einstein condensation (BEC) is the prototypical example of a mechanism which allows large numbers of massive particles to gain a macroscopically coherent phase, and is known to be attainable starting from the liquid state (as in superfluid ^{4}He) or from a gas (as in dilute cold atomic gases). BEC for a gas species of mass m and density n occurs below a transition temperature

$$T_C \approx \frac{2\pi\hbar^2}{k_B m}\left(\frac{n}{2.612}\right)^{2/3} \tag{1.1}$$

Fermions paired by the BCS mechanism can also condense (from what is essentially a liquid state) either into a hydrodynamic superfluid such as ^{3}He, or into the common electronic Fermi liquid superconductors (such as aluminum).

Once condensed, all of these systems exhibit the fascinating hallmarks of macroscopic superfluid flow: flux quantization, persistent currents, and the Josephson effect. One of the fundamental questions of condensed matter physics remains: from what other many-body ground states can such coherent macroscopic quantum behavior be reached? On one hand, there are systems which are definitely superfluid but for which the nature of the underlying normal ground state remains unknown (such as the high-T_c copper oxides, which attain superconductivity starting from exotic non-Fermi liquid phases [14]). On the other hand, it remains an open question whether a material can condense into a superfluid from one of the most elementary phases of matter, and one in which we can envision directly driven superflow: the solid state.

1.1 Introduction to Supersolids

A 'classic' supersolid [15, 16, 17, 18, 19] is a bosonic crystal with an interpenetrating superfluid component. Solid ^{4}He has long been the focus of searches for this state [20], because the large zero-point motion of helium should most easily facilitate overlapping wavefunctions that develop into a macroscopic phase. To demonstrate its existence unambiguously, macroscopic quantum phenomena [21] such as persistent mass currents, circulation quantization, quantized vortices, or the superfluid Josephson Effect must be observed. None of these effects have been detected in solid ^{4}He.

1.1.1 Early theoretical proposals

The first proposals that presented a models capable of displaying superfluidity in concert with the solid phase focused on the role of defects, because a commensurate perfect solid lattice was shown to be incompatible with such condensation (essentially because there was no uncertainty in the particle number, which is conjugate to a macroscopic phase). However, Andreev and Lifshitz [16] considered the case of tunneling defects with large zero-point motions, while Reatto and Chester [17, 18] investigated the properties of the Jastrow wave functions (which were otherwise known to give good phenomenological fits to noble gas atoms), and all came to the conclusion that lattice defects might in principle be able to Bose condense within a solid. The Reatto/Chester approach is the most transparent, in that they effectively treat a population of defects (such as vacancies) as a dilute boson quasiparticle gas ensemble interpenetrating the solid, and effectively able to condense under its own statistics by Eq. 1.1.

Finally, Leggett's paper in 1972 marked the end of the beginning for supersolids, as it showed that if one could achieve BEC for a defect ensemble in a solid, the observable consequence would be a nonclassical rotational inertia (NCRI) [19] - in other words, an apparently disappearing ("inertially decoupled") component of the mass of a solid sample as it entered the condensed state.

1.1.2 Kim and Chan effect

Assuming a vacancy or other defect population could undergo condensation according to the original proposals of Andreev/Lifshitz [16] and Reatto/Chester, [17, 18] experimentalists sought evidence of supersolid behavior - typically in ^{4}He - over the following decades by searching for well-known superfluid phenomena in the solid state. These searches looked for hydrodynamic flow through a capillary-array superleak [22], thermodynamic signatures of a phase transition [23], acoustic modes of defects [24], and inertial decoupling from a torsion oscillator [25]. Until 2004, none of these experiments found evidence of macroscopic superfluid within the solid. The most promising results were the acoustic measurements of Lengua and Goodkind [24] that revealed a low-temperature ultrasound resonance consistent with a population of crystalline defects that might undergo Bose-Einstein condensation, but which did not determine whether such condensation had actually occurred.

In 2004, the first indications that this material could be a supersolid were reported by Moses Chan and Eunseong Kim at Penn State. They observed an increase in the resonance frequency $f\,(T)$ of a torsion oscillator containing solid

^{4}He embedded in porous Vycor glass at temperatures below a few hundred mK, which they attributed to a probable observation of the missing moment of inertia due to BEC [26]. Their discovery is shown in Fig. 1.1. Shortly after this report, several important control experiments, including the blocked annulus (which effectively extinguished the signal) were reported [8], and these torsion oscillator frequency-shift observations were thereafter labeled an NCRI fraction (NCRIF) using the Leggett notation. To attempt to give a more model-independent analysis and notation of low temperature solid ^{4}He, we typically refer to this frequency shift (and associated dissipation peak, reported in the second paper [8]) as an inertial anomaly or an inertial transition.

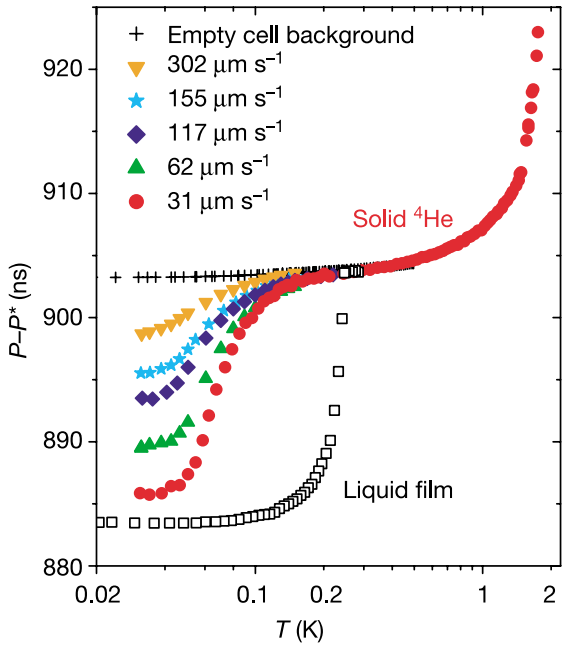

Figure 1.1: The Kim and Chan inertial anomaly.

The blocked annulus experiment - later verified by Rittner and Reppy [27] - remains perhaps the strongest evidence that some macroscopic quantum phase is indeed controlling the onset of the putative supersolid state, because it is hard to imagine a local strain field associated with a global flow path for the geometries, frequencies and viscosities considered.

These results (now widely reproduced [27, 28, 29, 30]) can be interpreted as a ^{4}He supersolid whose rotational inertia is reduced due to its superfluid component. Support for this interpretation comes from the reductions in the net frequency increase when the TO annuli containing solid ^{4}He are blocked [8, 27].

1.2 Unexpected observations in solid ^{4}He

But many phenomena inexplicable in the context of a classic superfluid are also observed in equivalent samples of solid ^{4}He. For one thing, an unexpected ^{3}He doping effect changes the putative transition temperature by a huge amount: the inertial anomaly is detectable below a temperature $T_C \sim 65\,\mathrm{mK}$ in the purest, most crystalline samples, below $T_C \sim 300\,\mathrm{mK}$ in more amorphous samples, and below at least $T_C \sim 500\,\mathrm{mK}$ when dilute concentrations of ^{3}He exist [26, 8, 11, 31].

A strong dissipation peak in $D(T)$ also occurs in association with the rapid rise of $f(T)$ [8, 11, 27] but their relationship has not been explained.

Other phenomena include maximum DC mass flow rates inconsistent with the TO dynamics [32, 33, 34], strong effects of annealing on the magnitude of TO frequency shifts [27, 35], velocity hysteresis in the frequency shift [28], and shear stiffening of the solid coincident with the TO frequency increase [10]. These phenomena indicate some unanticipated interplay between dynamical degrees of freedom of the solid and any superfluid component.

1.3 New theories of the solid ^{4}He inertial anomaly

In response, new theories have been proposed that solid ^{4}He is (i) a non-superfluid glass [36, 37, 38], (ii) a fluid of fluctuating quantum vortices [39, 40], (iii) a superfluid network at linked grain boundaries [41], (iv) a viscoelastic solid [42], or a superglass - a type of granular superfluid within an amorphous solid [43, 44, 45, 46]. To help discriminate between such ideas, we focus on the relaxation dynamics of solid ^{4}He which should distinguish a simple superfluid state from a purely glassy state.

CHAPTER 2

THE SQUID-BASED TORSION OSCILLATOR

2.1 Experimental Apparatus

Contrary to most engineering materials, all observations of solid helium must be performed in the very apparatus in which the sample is formed. This fact thereby drastically constrains the measurements which may be done on any single sample, because the pressurized cryogenic environment necessary for sample formation is not simultaneously conducive to inclusion of a wide array of materials science instrumentation. Samples which are grown in one lab with a single type of instrumentation (for example, a shear-modulus detector as in [10]) cannot be removed from the refrigerator and transported to another laboratory to facilitate comparison or different measurements under the same growth conditions.

To illustrate the inherent difficulty, note that the most successful recent attempt by anyone to achieve multi-laboratory measurements of a single sample required shipping a bottle of ^{3}He that had been used in Alberta as shear modulus sample material to Penn State where it was re-used to form torsion-oscillator samples [47]. In this way, the ^{4}He impurity concentration (1.35 ppm) was enforced to be identical for the two sets of measurements, but since the conditions of international freight required the solid helium samples to be vaporized for transit, other sample growth conditions were not necessarily identical. Even so, such transport remains the state-of-the-art approximation for measuring identical solid helium samples in separate facilities, and its demonstration was - quite apart from the resultant isotope-dependent observations - an impressive tech-

nical accomplishment by Josh West *et al*.

In addition, related to the many unexpected materials properties of solid helium in context of a classic supersolid transition as discussed in Sec. 1.2, we observed that is possible to slightly disturb the sample (inducing slight shifts to its inertial properties) by disturbing the cryostat mechanically (e.g transferring liquid helium to the dewar). These type of disturbances were also reported to affect the shear modulus of such samples, specifically by application of ~700 Pa stresses [48], and was there associated with introducing kinks to existing dislocations within the crystal. We therefore decided that sensitive data representing a single sample observation of publishable quality should be acquired completely without such disturbances - that is, specifically avoiding helium transfers, and also in an overall quiet vibration environment.

Acquiring sufficient data quickly enough to capture a complete set of observations without disturbing the sample enforced a high duty-cycle demand on our instrumentation, which required both a high degree of automation (to rapidly sweep control parameters) and high signal-to-noise detection technology (to reduce the demand for integration dwell time between data points). Therefore, to measure the finely resolved time-dependent inertial materials properties of solid helium, we constructed a vibrationally-isolated millikelvin cryostat with automated data acquisition and temperature control, and used a high-dynamic range DC-SQUID-based displacement sensor to detect the inertial response of an annular torsion oscillator containing the sample.

2.1.1 Torsion oscillator body

The construction of our torsion oscillator utilizes a novel displacement measurement scheme facilitated both by a current-amplified DC-biased parallel-plate capacitor (which is the traditional technique) and also by a high-sensitivity DC-SQUID detector. The samples are formed inside an annular chamber with a cross-section of 0.1 mm x 3 mm and mean radius of 4.5 mm, which corresponds to a surface-to-volume ratio of 200 cm^{-1}. The torsion rod - which provides restoring torque to the stycast body under rotation - is made of annealed beryllium copper (BeCu) and the chamber containing the solid helium is made of Stycast 1266 (see Fig 2.1). The resonant frequency of the empty cell at 300 mK is 575.018 Hz and that of the full cell at 300 mK is 574.452 Hz. The full-cell quality factor Q at 300 mK is $8x10^5$.

A thin annular geometry was chosen in order to provide a sample with a well-defined torsional radius, and also because Rittner and Reppy found that the amorphous samples assumed to form within tight annular confinement tend to display large inertial changes associated with the supersolid transition [49], and we therefore expected such a design to allow relatively higher signal-to-noise than open cylindrical samples.

Although this design goal was successful for our purposes (our putative NCRIF was roughly 5% - see sec. 4.1) we should note that in at least one case, a torsion oscillator that was constructed with tightly confined sample space (for the same design reason) did not in fact achieve a significant boost to the magnitude of the inertial signal [50] compared to an open cell geometry. Based on this observation, it seems clear that the effects of sample boundary conditions on the inertial anomaly are not well understood. Nonetheless, our samples exhibited

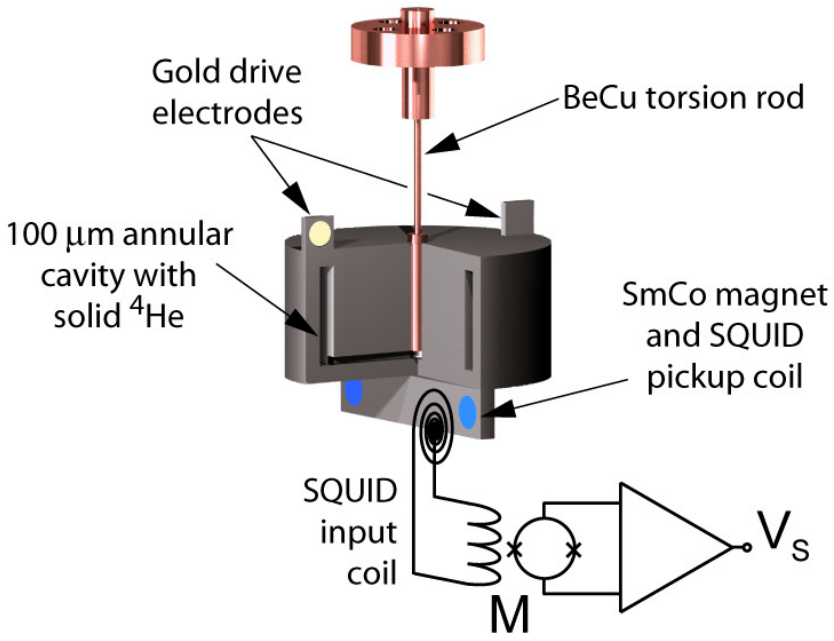

Figure 2.1: Cross-sectional schematic view of the SQUID-based torsion oscillator (TO).
Applying an AC voltage to the drive electrodes rotates the Stycast chassis (containing the solid ^{4}He in a 100-μm-wide annular cavity) about the axis of the BeCu torsion rod. The angular displacement of a SmCo magnet mounted on the TO generates a change in the magnetic flux through the stationary pickup and input coils of a DC-SQUID circuit and thereby a voltage proportional to displacement.

the same class of inertial phenomena as other experiments and are representative of the amorphous material which is in need of a microscopic model for its low-temperature properties.

2.1.2 Refrigeration below 20 mK

The BeCu torsion rod serves as the pressurized fill capillary for the helium, and is sealed by indium o-ring to a large copper vibration isolator which is in turn mounted to the mixing chamber of a dilution refrigerator. Thermometers are mounted to the copper vibration isolator (which also houses the capacitive pres-

sure gauge) and to the mixing chamber plate, and are verified to agree with each other. The refrigerator and experimental components are shown in Fig. 2.2. The components between the still and mixing chamber were purchased commercially from Janis [51]; all other parts of the probe and cryostat were built at Cornell. The refrigerator routinely operates at a base temperature below 10 mK, and as for long-term stability, we were able to study samples for months at a time at temperatures which were always kept below 0.5 K.

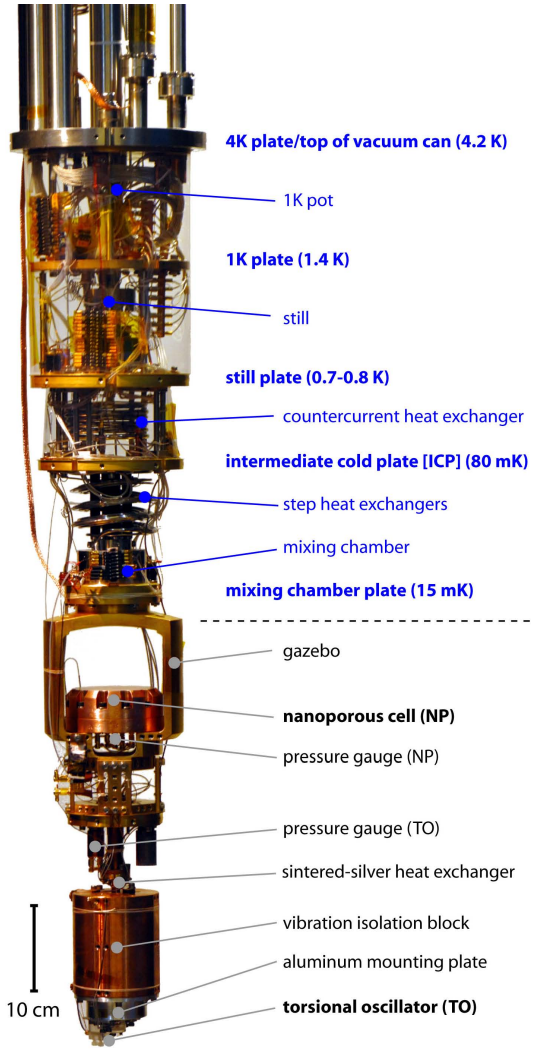

Figure 2.2: Photograph of the dilution refrigerator (blue labels) and mounted experiments (black labels). The torsion oscillator experiment is visible at the bottom. For visibility, the radiation shields, niobium SQUID-shielding can surrounding the TO, and vacuum can are all removed.

2.1.3 Vibration isolation

Careful consideration was given to vibration isolation, since the highly sensitive SQUID detector is easily capable of resolving spurious motion caused by environmental vibrations below those levels typically of interest for standard capacitor-detected oscillators. The dilution refrigerator probe is mounted by three air springs to a vibration-damped lead-filled triangular table, which sits in an acoustically-isolated room (dubbed the "internal acoustic chamber" or IAC) that is itself mounted to a massive 30-ton concrete block which rests on 6 large air springs within an outer acoustically-shielded room in the A-wing of the basement of Clark Hall at Cornell. The cryostat and vibration isolation schematic from construction documents are shown in Fig 2.3.

2.1.4 Blocked-capillary sample preparation

The helium sample is prepared by the blocked capillary method, in which the stycast body is filled with helium in the liquid state at high pressure (typically >70 bars at >3K). The 1K pot is then turned on, which freezes a plug of solid helium in the fill capillary near the 1K plate that serves to generally fix the number of helium atoms in the sample space below the plug (which includes the Stycast body, the pressure gauge, and the extent of the fill capillary below the 1K plate). The dilution refrigerator is then turned on, which cools the fixed helium sample in the stycast TO to base temperature (with a temperature gradient up the remainder of the fill line as it is thermally anchored to the various refrigeration stages). The pressure-temperature profile for a typical solid sample preparation in our cell using this method is shown in Fig 2.4.

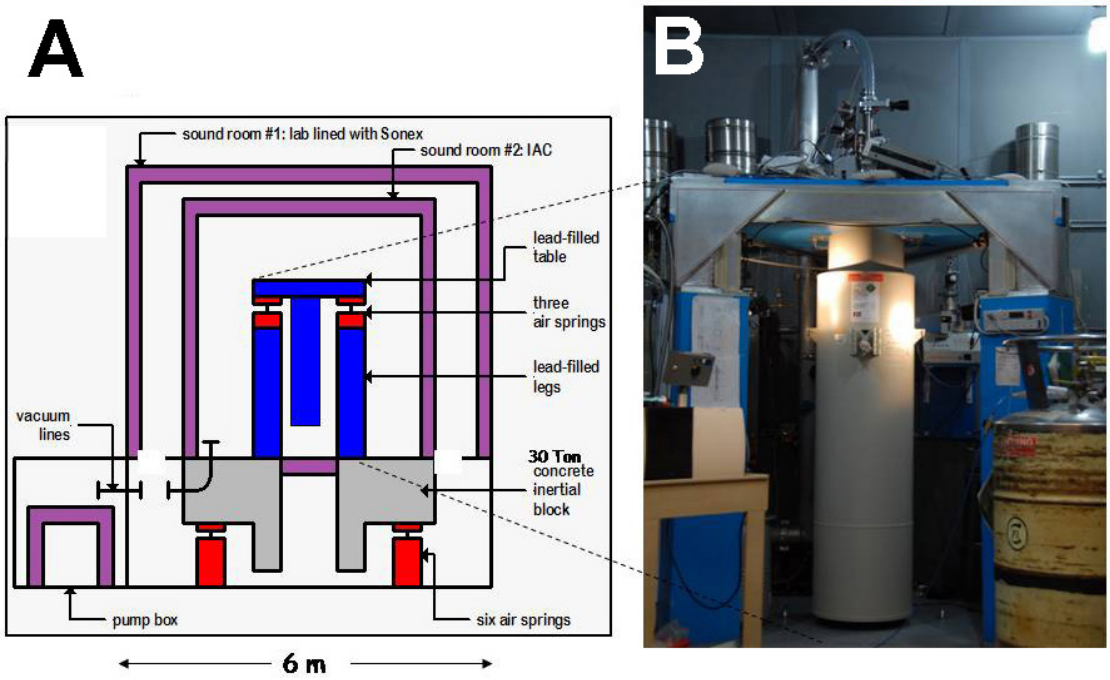

Figure 2.3: **A**: Schematic of "floating" lab space and details of vibration isolation components. **B**: A photograph of the cryostat probe and dewar (which are shown in blue schematically on the left). The plastic still-pumping line can be seen at top center. The two kegs seen on the left-hand side of the back wall contain the ^{3}He/^{4}He mash mixture that operates the dilution refrigerator. The single keg on the right-hand side of the back wall stores clean ^{4}He that is used to form the high-pressure solid sample.

As the dilution refrigerator cools the sample, the pressure follows the melting curve (indicated partially by red circles in Fig. 2.4) and finally reaches a low-temperature equilibrium pressure (in this case ~40 bar) in the solid phase above the melting curve, indicating the low-temperature solid density that corresponds to the value expected for the fixed number of atoms inserted into the sample space before plugging. At that point, the solid pressure departs from the melting curve and remains relatively constant down to the lowest temperatures.

By varying the pressure in the cell before plugging, the final pressure can be adjusted between different sample preparations, although it is typically difficult to predict the final pressure of a given cell before calibrating it. For our

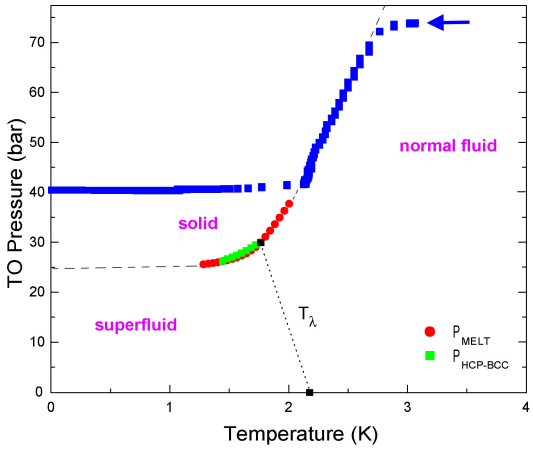

Figure 2.4: Typical solidification of a helium sample in our apparatus, overlaid on the schematic phase diagram. As the helium sample cools towards the solidification boundary of the phase diagram, its pressure (blue squares) runs down the melting curve until the equilibrium pressure is reached at low temperature. Most of the solid phase diagram shown here corresponds to hcp phase, but for reference, the small sliver of bcc is indicated by the green squares.

oscillator and capillary, a starting pressure of ~75 bar at 3K results in a final low temperature sample pressure of ~40 bar, which is well into the solid phase (i.e. well above the ~24 bar melting curve).

2.2 SQUID-based displacement detection

The DC SQUID is used at low velocities (below $\sim$ 30 $^{\mathrm{um}}/_{\mathrm{s}}$) to detect the the oscillatory motion of the torsion oscillator by transducing the displacement of a small SmCo magnet embedded in the Stycast body. At higher velocities, a standard set of capacitive electrodes can be switched on for displacement detection in the regime where signal to noise is not otherwise a problem. A general schematic of the detection elements, and a photograph showing installation, are displayed in Fig. 2.5.

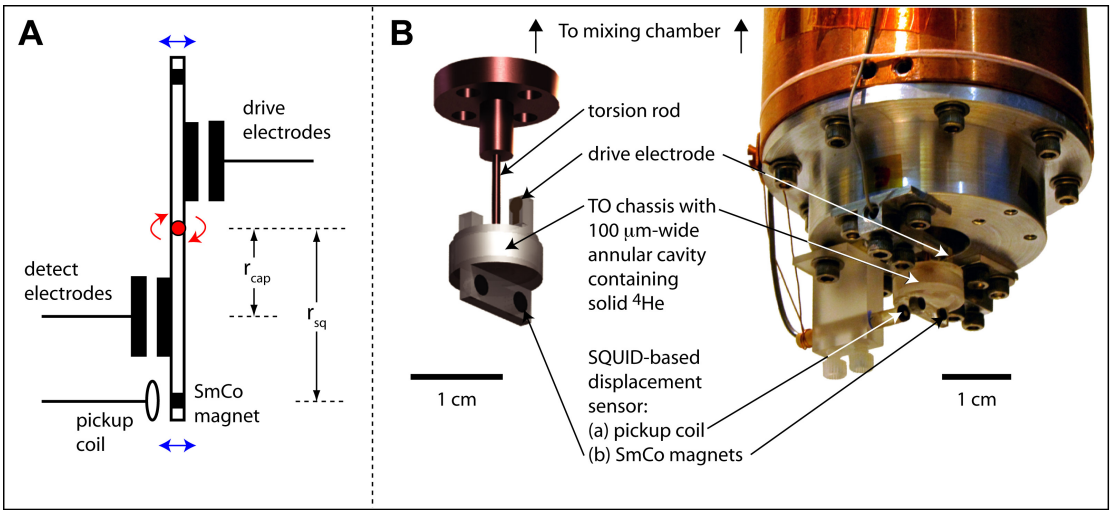

Figure 2.5: **A:** Axial-view schematic of drive and detection by means of both parallel plate capacitor electrodes and a DC SQUID pickup coil which transduces the displacement of a SmCo magnet embedded in the stycast TO body with sensitivity on the order of $10\frac{\text{fm}}{\sqrt{Hz}}$. The capacitor plates are at a radius $r_{\text{cap}} = 3.5\,\text{mm}$; the SmCo magnets and SQUID pickup coil are embedded at a radius $r_{\text{sq}} = 4.5$ mm**. B:** 3D scale schematic of the TO, and a photograph showing installation on the cryostat.

The SQUID operates in a flux-locked-loop mode which linearizes the input flux (generated by the moving magnet on the TO) and thereby provides a voltage proportional to displacement. Typically, such a displacement sensor operates without the aid of a permanent magnet, and requires therefore an injected current in a parallel tank circuit. A diagram showing this typical circuit, and also our setup with the SmCo magnet, is shown in Fig. 2.6.

The sensitivity of the SQUID to position displacement is $\frac{dV}{dx} = 2.4\,\text{V}/\text{nm}$ on the highest sensitivity range; at which the noise floor provides a sensitivity limit of roughly $10\,\text{fm}/\sqrt{\text{Hz}}$. For most of our observations, we actually operated with medium sensitivity (a factor of 10 decrease) to boost the dynamic range.

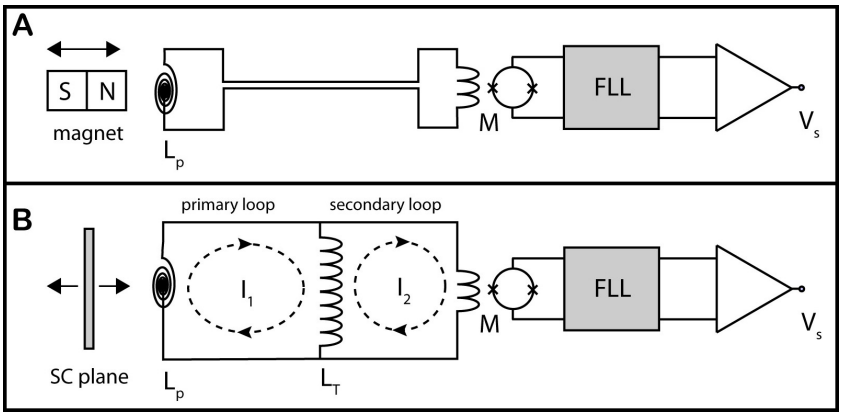

Figure 2.6: **A:** Schematic SQUID transducer as used in our experiments. A moving permanent magnet induces flux in the pickup coil of the SQUID, which is then transduced to a voltage proportional to magnet displacement. **B:** Typical SQUID displacement transducer. The sensitivity to motion of a superconducting film is increased by injecting a large persistent current in the parallel tank circuit (secondary loop). This design requires more superconducting joints, and current-injection terminals, than the version we used.

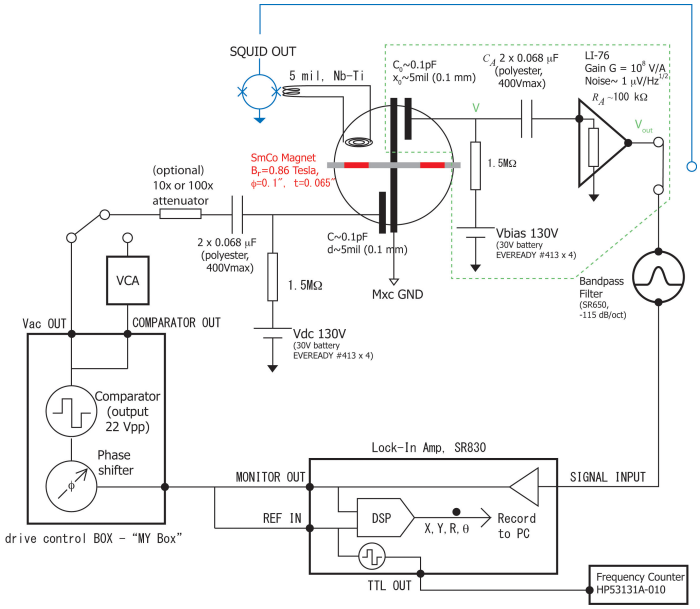

Figure 2.7: Schematic phase-locked-loop as typically used in our on-resonance experiments. The drive torque frequency is locked to the oscillator resonance, which can then be observed as a function of temperature. A switch allows operation using traditional capacitive detection at high velocity (using the LI-76 current preamplifier), or operation using the SQUID at low velocity.

With the SQUID providing a voltage proportional to the displacement of the oscillator, the typical method for acquiring temperature-dependent observations of the solid ^{4}He requires that the oscillator drive torque be locked onto the resonance frequency by means of a phase-locked-loop circuit. The necessary feedback circuit for tracking the drive frequency to the oscillator resonance is shown in Fig. 2.7 (though the rotational susceptibility can also be observed directly at any chosen probe frequency; see Sec. 3.1).

Preamplifiers for both the regular capacitor electrodes and the commercial DC-SQUID are mounted to the room-temperature plate of the cryostat, close to the vacuum feedthroughs to ensure short cable lengths. The SQUID loop is mounted in a shielded can in the liquid helium bath space of the dewar, with sealed feedthroughs for the current leads into the vacuum can and lead tubing to shield the leads down to the experiment space below the mixing chamber.

CHAPTER 3

TORSION OSCILLATOR SUSCEPTIBILITY

The fundamental measurement that a torsion oscillator enables is encoded in the oscillator's complex response to an applied torque - that is, its rotational susceptibility. Therefore, we now derive the connections between physical processes which could occur in the helium (including, but not limited to, supersolidity) and the oscillator's rotational susceptibility, the real and imaginary parts of which are recoverable from the measured resonance frequency and oscillation amplitude.

Some of the following discussion closely follows that first put forth in Ref. [36] and subsequently in Ref. [42]. In the time domain, the angular displacement $\theta(t)$ attained by applying a torque $\Gamma_{\text{ext}}(t) = \Gamma_0 \sin(\omega t)$ to the oscillator is given by

$$\left(I_{\text{TO}} \frac{d^2}{dt^2} + \gamma_{\text{TO}} \frac{d}{dt} + K \right) \theta(t) = \Gamma_{\text{ext}}(t) + \int g(t - t')\theta(t')dt' \tag{3.1}$$

for a linear system invariant under time translation. The second term on the right-hand side of the equation is sometimes called the "back-action" of the helium on the TO chassis: due to its finite shear modulus the helium exerts a moment on the TO. Formulating the dynamical problem in this way allows the entire temperature dependence of the susceptibility to be included in the back-action term $g(t, T)$. Taking the Fourier transform of Eq. 3.1, we find that $\theta(\omega) = \Gamma_{\text{ext}}(\omega)\chi(\omega)$, where

$$\chi^{-1}(\omega, T) = \chi_0^{-1}(\omega) - g(\omega, T), \tag{3.2}$$

and the rotational susceptibility of the empty TO

$$\chi_0^{-1}(\omega) = -I_{\text{TO}}\omega^2 - i\gamma_{\text{TO}}\omega + K \tag{3.3}$$

is assumed to be temperature-independent. In this expression, the term describing the helium $g(\omega, T)$ has a temperature-independent part $I_{\mathrm{He}}\omega^2$ and a temperature-dependent part $\chi_g^{-1}(\omega, T)$, so that

$$g(\omega, T) = I_{\mathrm{He}}\omega^2 + \chi_g^{-1}(\omega, T). \tag{3.4}$$

The definition of χ_g^{-1} is model-dependent and will be made as needed below. The resonant frequency of the system at the lowest temperature is $\omega_0 = \sqrt{\frac{K}{I}}$, which is that of a perfectly rigid rotor with moment of inertia $I = I_{\mathrm{TO}} + I_{\mathrm{He}}$. It is easy to measure the bare oscillator susceptibility as implied by Eq. 3.3 - the modulus of just such a measurement is shown in Fig. 3.1 along with a $Q \sim$ 4x10^6 Lorentzian curve for reference. Note the extremely high dynamic range excursion as one sweeps over the resonance.

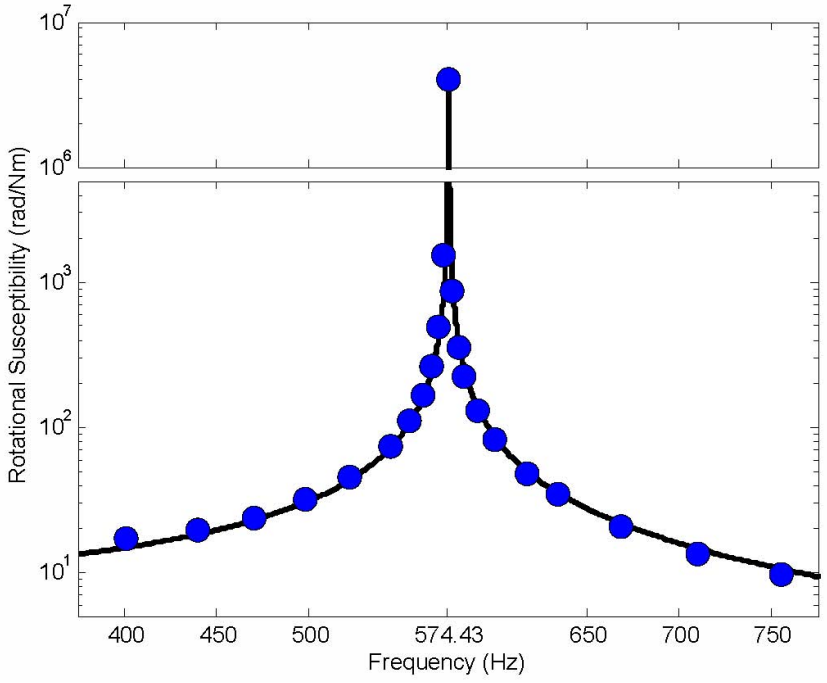

Figure 3.1: Rotational susceptibility $\chi(\omega)$ of the TO-^{4}He oscillator (blue dots). Error bars, as well as interesting temperature-dependent effects due to the helium, are smaller than the symbol size. The solid curve is the theoretical susceptibility of a $Q =$ 4x10^6 damped simple harmonic oscillator. The break in vertical scale accommodates the high dynamic range of the resonance.

We neglect the small dissipation of the TO $\gamma = I\omega_0 Q_\infty^{-1} = I\omega_0 D_\infty$ in the following because it contributes a correction to the resonant frequency proportional to D_∞^2, which is $\mathcal{O}\left(10^{-11}\right)$.

At this point, the model susceptibility should be formally expressed in terms of the measured properties of the oscillator, which are different depending on whether one operates the oscillator on-resonance or not. Both sets of operating conditions will be addressed in the following two sections.

3.1 Frequency-dependent rotational susceptibility

High-Q torsion oscillators are typically operated at their resonance frequency. The inertia of the sample acts as a perturbation to the damping and resonant operating frequency of the oscillator; those perturbations are resolved with extremely high signal-to-noise (S/N) ratios, limited only by the extremely low inherent BeCu background dissipation. Unfortunately, this high S/N comes at the cost of fixing the probe frequency to a somewhat arbitrary value, set not by the interesting physics of the helium sample under study but mainly by the material properties of copper.

This fact, coupled with the difficulty of reproducing samples identically in separate oscillators (see Sec. 2.1 if envisioning a series of TO's, each one at a different frequency) makes traditional on-resonance torsion oscillators a very poor tool for observing frequency-dependent properties of solid helium. Currently, the best one can do is craft a TO with two torsion modes and measure each mode on-resonance [28]. While the dual-frequency results thus obtained at Rutgers were highly valuable in establishing that there *exists* a non-trivial fre-

quency dependence of the inertia, that there were only two probe frequencies prevented them from establishing the nature of that frequency dependence.

Our oscillator has only one torsion mode. Nonetheless, in this section we will develop the frequency-dependent susceptibility $\chi(\omega) \equiv \theta(\omega)/\Gamma_{ext}(\omega)$ of a single-mode torsion oscillator operated many linewidths away from the resonance, and show our measurements of $\chi(\omega, T)$ for the following reasons:

- The algebra is much more transparent (connecting the helium physics directly to the observables) than the perturbation analysis of resonance shifts.
- The detection circuit is simpler, allowing one to verify that the more complicated phase-locked-loop (Fig. 2.7) does not introduce artifacts to the on-resonance measurements.
- This susceptibility will transparently show why frequency-dependent measurements are a high priority for the future determination of the microscopic physics of solid helium, and in what form to analyze such data.

As many authors have pointed out [36, 42, 39], what is measured in the torsional oscillator measurements is not the moment of inertia of the TO-helium system but rather its susceptibility $\chi(t)$ to an external torque. The most direct observation of the susceptibility is attained by applying a torque $\Gamma_{ext}(t) = \Gamma_0 \sin(\omega t)$ and measuring the resulting complex displacement angle of the oscillator $\theta(t)$ (in other words, the amount of oscillator motion in-phase and out-of-phase with the drive torque). A direct measurement of this displacement with a phase-sensitive lock-in amplifier is enabled by the circuit shown schematically in Fig. 3.2 below; bear in mind that it is not the typical resonant detection scheme used

for most torsion oscillators (see also Sec. 3.2) .

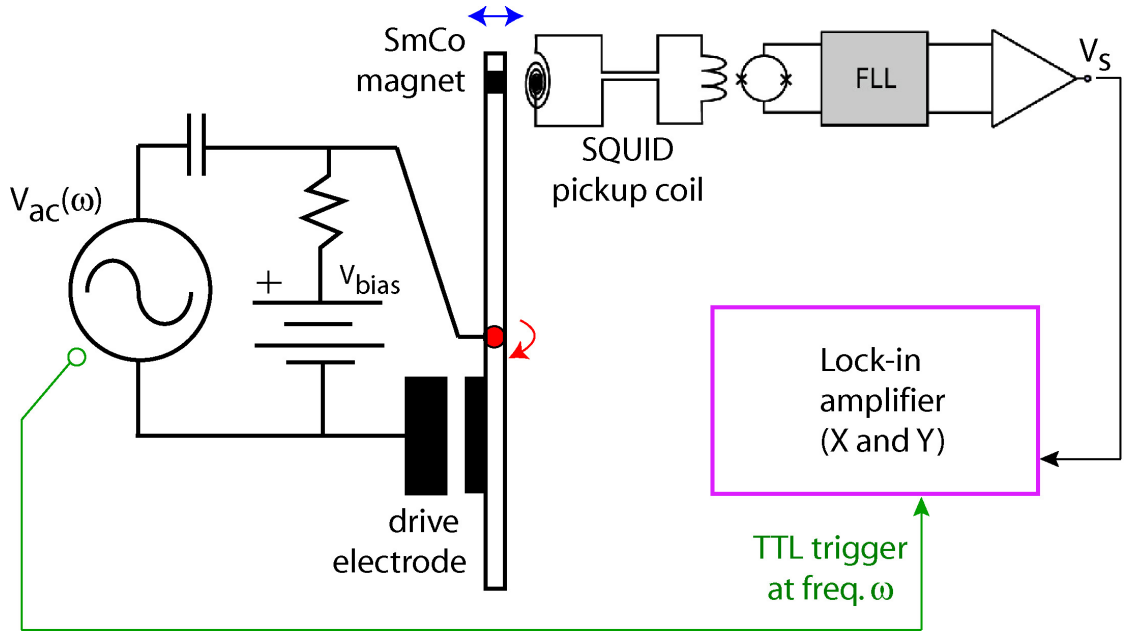

Figure 3.2: Circuit diagram for direct measurement of the torsion oscillator susceptibility. Note the operational simplicity as compared to the on-resonance circuit of Fig. 2.7. A sinusoidal AC voltage is applied - and the in-phase (X) and out-of-phase (Y) components of the displacement measured - at any chosen probe frequency ω. By sweeping ω with enough S/N, one directly acquires the frequency-dependent rotational susceptibility.

3.1.1 Overdamped physical models for an inertial transition

Even assuming an overdamped internal dissipative degree of freedom can be a useful phenomenology controlling the onset of the inertial anomaly, we note that nevertheless there is disagreement as to the frequency dependent coupling of this mode to the oscillator [36, 42], in addition to a lack of understanding of the frequency dependence of the transition itself. Therefore we wish to leave the coupling as a measured parameter, to be determined by observing the frequency-

dependent susceptibility. So, we choose the following form of the back action:

$$\chi_g^{-1}(T) = \frac{C_p \omega^p}{1 - i\omega\tau(T)} \tag{3.5}$$

where the frequency coupling to the oscillator is left as the undetermined parameter p (and the units of the strength C_p thus depend on p). This gives a total susceptibility for the oscillator that can be written in the following form:

$$\frac{\chi^{-1}(T)}{I_{\text{osc}}} = \omega_0^2 - \omega^2 - i\frac{\omega_0 \omega}{Q} - \frac{C_p \omega^p}{1 - i\omega\tau(T)} \tag{3.6}$$

Note that this form is consistent with (and more general than) a freeze-out transition $(p = 2)$ phenomenology [36] and/or the viscoelastic $(p = 4)$ model [42]. In fact for definiteness, we list the specific choice of p from those models (and the back-action term in their own notation) in Table 3.1:

Table 3.1: Frequency - dependent models of helium back-action on a torsion oscillator.

Reference:	Nussinov *et al* [36]	Yoo and Dorsey [42]
Physics:	Debye freeze-out	Viscoelasticity
p	0	4
$C_p \omega^p$	$\frac{g_0}{I_{\text{eff}}}$	$\frac{\rho_n}{\rho} R^2 \left(\frac{I_{\text{He}}}{I_{\text{osc}}}\right) F\left(\frac{h}{R}\right) \omega^4$

A simple superfluid decoupling is worth modeling separately, because it would otherwise be associated with the peculiar term $\tau(T) = 0$ for all temperatures (i.e, one cannot excite damping at finite frequency). A simple superfluid term cannot responsible for the dissipation peak, which is what we hope to describe by an increasing $\tau(T)$ term, so we treat it as a special case. (Inserting a supercurrent into the model does not preclude observing overdamped $p = 2$ physics if it exists.) By convention we choose the superfluid term to be zero at

low temperature, making $T \rightarrow 0$ the reference temperature:

$$\begin{cases} \dfrac{\chi^{-1}(T)}{I_{\text{osc}}\left(1-\delta_{T\rightarrow 0}\right)} = \omega_0^2 - \left[1+\delta(T)\right]\omega^2 - i\dfrac{\omega_0\omega}{Q} - \dfrac{C_p\omega^p}{1-i\omega\tau(T)} \\ \\ \delta(T) = \dfrac{\rho_s(T)}{\rho}\dfrac{I_{\text{He}}}{I_{\text{osc}}} \end{cases} \tag{3.7}$$

The denominator on the left of Eq. 3.7 can now be redefined (to first order in δ) if desired, and the values of ω_0 and C_p may now be redefined slightly – but practically, these slight shifts don't matter. We measure deviations from a fixed value of susceptibility (in other words, small temperature-dependent deviations from the curve in Fig. 3.1) - the deviations are observed with extremely high *precision*, but the fixed value (which we normalize against) is probably not known with extremely high *accuracy*. It is measured only to about 3 or 4 significant figures.

By nulling the baseline susceptibility measurement at low temperature $|\chi_0|$ (zeroing-out the measurement of Fig. 3.1), the lockin thereafter directly records the quadrature susceptibility shift $\triangle\chi(T) \equiv \chi(T) - \chi(0)$: literally the complex change in angular displacement-per-torque as temperature varies from the reference, at fixed frequency. (We prefer normalized units, achieved by dividing out the oscillator's baseline susceptibility $|\chi_0|$, in order to avoid needing to measure the moment of inertia.) Note that $\triangle\chi(T)$ is not a quantity directly entering Eq. 3.7 - the algebra connecting the two follows.

Also note that we neglect Q_{osc}^{-1}, so that $|\chi_0| = \chi(0) = \left[I_{\text{eff}}\left(\omega_0^2 - \omega^2\right)\right]^{-1}$. This corresponds to conditions of the experiment, in which we assume that the entire magnitude of response at the reference temperature belongs to the in-phase channel, and requires again that the operating frequency be far from the resonance. The algebra in Eq. 3.8 makes explicit how to put the model in the same form as our data:

$$\frac{\triangle\chi(T)}{|\chi_0|} = \frac{\chi(T) - \chi(0)}{|\chi_0|} = \frac{\chi(T)}{\chi(0)} - 1$$

$$\Rightarrow \left[1 + \frac{\triangle\chi(T)}{|\chi_0|}\right]^{-1} = \left[\frac{\chi(T)}{\chi(0)}\right]^{-1}$$

$$\Rightarrow \frac{\triangle\chi(T)}{|\chi_0|} \approx 1 - \frac{\chi^{-1}(T)}{\chi^{-1}(0)} = \frac{1}{\omega_0^2 - \omega^2}\left(\delta(T)\,\omega^2 + \frac{C_p\omega^p}{1 - i\omega\tau(T)}\right) \tag{3.8}$$

The left-hand side of Eq. 3.8 is in the form of our frequency-dependent measurements, while the right hand side is in the form of the model (Eq. 3.7). The approximation symbol implies all manner of small neglected terms, including the binomial expansion used to proceed from the second to third line.

Alternatively, if the oscillator is locked on-resonance, one could start with the model in Eq. 3.7 and expand about the pole ω_0 in order to find predictions for the measured $\triangle f$ and $\triangle Q^{-1}$ (which we do in section 3.2).

Our observables are small changes to the overall copper oscillator susceptibility, so in practice it doesn't matter if one normalizes the data by treating$|\chi_0|$ as the susceptibility of the empty or full cell as long as the probe frequency is far from resonance. The difference is merely a small lack of accuracy. It is also useful to use the conjugate form of Eq. 3.8 which allows direct matching of real and imaginary parts of the model to the measured off-resonance data:

$$\frac{\triangle\chi(T)}{|\chi_0|}\left(\omega_0^2 - \omega^2\right) \approx \delta(T)\,\omega^2 + \frac{C_p}{1 + (\tau(T)\,\omega)^2}\left(\omega^p + i\tau(T)\,\omega^{p+1}\right) \tag{3.9}$$

3.1.2 Temperature dependence

Without delving into the open questions over the specific temperature dependence of a putative internal overdamped mode [36, 42], following is simply the minimal physically plausible temperature-dependent limits necessary to begin to pull new results out of the model in Eq. 3.7:

$$\delta(T) = \begin{cases} 0, & T \to 0 \\ \dfrac{\rho_s^0}{\rho}\dfrac{I_{\mathrm{He}}}{I_{\mathrm{osc}}}, & T \to \infty \end{cases} \qquad \omega\tau(T) \begin{cases} \gg 1, & T \to 0 \\ = 1, & T = T_* \\ \ll 1, & T \to \infty \end{cases} \tag{3.10}$$

The physics contained in Eq. 3.10 is straightforward: 1) the superfluid saturates (adding inertia to the oscillator at higher temperatures); 2) the dissipative relaxation speeds up when the sample gets hotter, causing an inertial transition to occur at a temperature T_* which we now define as that which matches the probe frequency to the dissipation rate of the internal overdamped mode.

3.1.3 Frequency-dependent predictions

The most important observation to make off-resonance is the functional dependence $T_*(\omega)$, which is known to be nontrivial [28], but about which little else is known. Also, by inspection of Eqs. 3.9 and 3.10 evaluated at $T = T_*$ we can immediately read off the prediction for the magnitude of the dissipation peak $\triangle\chi''_{\mathrm{peak}}$,

$$\frac{\triangle\chi''_{\mathrm{peak}}}{|\chi_0|}\left(\omega_0^2 - \omega^2\right) = \Im\frac{\triangle\chi(T_*)}{|\chi_0|}\left(\omega_0^2 - \omega^2\right) = \frac{1}{2}C_p\omega^p \tag{3.11}$$

Similarly, we can read off the saturated difference between low-and-high temperature limits of the real part of the susceptibility $\triangle\chi'_{\mathrm{sat}}$ (which corresponds to

the quantity typically interpreted as "NCRIF."):

$$\frac{\triangle\chi'_{\text{sat}}}{|\chi_0|}\left(\omega_0^2-\omega^2\right)=\Re\frac{\triangle\chi\left(T\to\infty\right)}{|\chi_0|}\left(\omega_0^2-\omega^2\right)=\frac{\rho_s^0}{\rho}\frac{I_{\text{He}}}{I_{\text{osc}}}\omega^2+C_p\omega^p \quad (3.12)$$

Because the term $C_p\omega^p$ appears in both Eq. 3.11 and 3.12, one can tell whether the superfluid term is needed to explain the data or not. If the saturated real susceptibility shift is completely predicted by the magnitude of the dissipation peak then one will observe that $\rho_s\left(T\right)=0$ for all temperatures.

By subtracting Eq. 3.11 from 3.12 for a range of probe frequencies ω, we find that the saturated superfluid density appears as the slope of the following line, independent of p:

$$\frac{\triangle\chi'_{\text{sat}}-2\triangle\chi''_{\text{peak}}}{|\chi_0|}=\left(\frac{\rho_s^0}{\rho}\right)\times\left[\frac{\omega^2}{\omega_0^2-\omega^2}\right] \quad (3.13)$$

Eq. 3.13 suggests we plot the subtracted data against the reduced frequency axis as defined in the bracket; they are predicted to fall on a line, the slope of which is the saturated superfluid density. If the Kramers-Kronig relations are satisfied by a simple freeze-out of an overdamped mode, the slope will simply be zero. If, on the other hand, the saturated superfluid term exists but has perhaps a frequency dependence, then the data will not fall on a line at all.

Alternatively, one can acquire a particularly useful prediction if one divides Eq. 3.12 by Eq 3.11:

$$\left(\frac{\triangle\chi'_{\text{sat}}}{2\triangle\chi''_{\text{peak}}}-1\right)^{-1}=\left(\frac{\rho_s^0}{\rho}\frac{I_{\text{He}}}{I_{\text{osc}}}\right)^{-1}C_p\omega^{p-2} \quad (3.14)$$

which predicts a power law as a function of drive frequency ω, where the slope on a log-log plot gives $p-2$ with no free parameters. Note, for example, that the difference between Drude relaxation ($p=0$) and viscoelasticity ($p=4$) is particularly stark (see Table 3.1): the power law has a positive slope for viscoelasticity

and a negative slope for Drude relaxation. Just as important, the two measured quantities $\triangle\chi'_{\text{sat}}$ and $\triangle\chi''_{\text{peak}}$ on the left-hand side are the highest-quality observables in off-resonance frequency sweeps. The strategic value of frequency-dependent observation is easily seen here, since the susceptibility measured at a single (e.g. resonance) frequency provides no way to determine p.

Figure 3.3 shows measured temperature-dependent observations of the complex susceptibility acquired at various frequencies (sweeping the temperature smoothly while holding ω constant). A smooth frequency sweep at fixed temperature is desirable but not possible given the dynamic range of the lockin.

Unfortunately, although the inertial transition is clearly observed to occur at various frequencies away from resonance, even the high S/N of the DC-SQUID was insufficient to acquire quality data which might have been used to observe $T_*(\omega)$ or to fit the predictions of Eqs. 3.13 and 3.14.

A major impediment to quality data acquisition is the onset of temperature-dependent ultra-slow inertial relaxations that were not known to exist when we built the oscillator (see Sec. 4.2). These ultraslow relaxations demand that the experiment sweep be carried out slowly enough to observe the equilibrium inertia. Yet, we need to operate fast enough to avoid the inertial signals being dominated by $1/f$ noise from the DC-SQUID [52]. In practice, there was no overlapping parameter space between these conflicting demands. We estimate that the displacement detection scheme would need a further boost in S/N of roughly a factor of 100 beyond that of the existing DC-SQUID to provide sufficient quality data.

Nonetheless, we hope that the presentation in this section has successfully

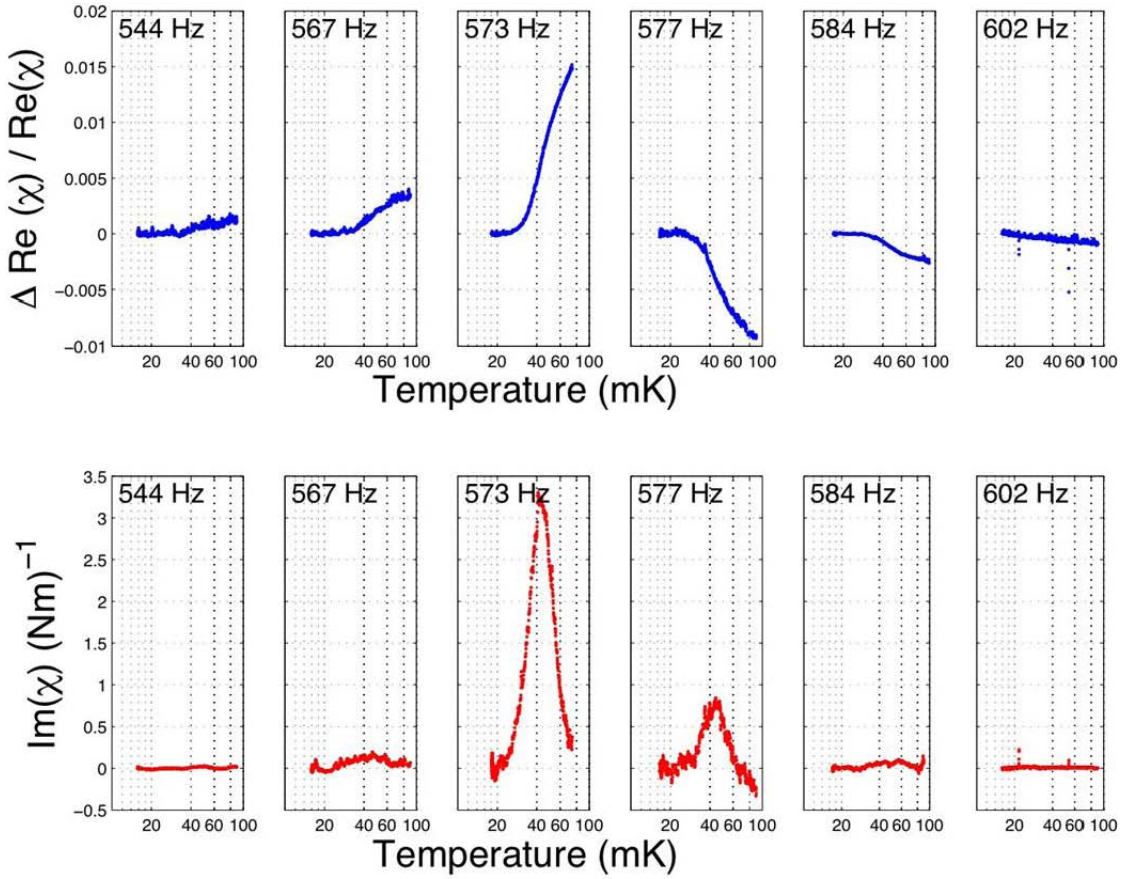

Figure 3.3: Onset of the solid ^{4}He inertial anomaly observed in the rotational susceptibility at various frequencies off-resonance. Top panels indicate the real susceptibility; bottom panels give the dissipation (see Eq. 3.9). By eye, one can see that $\triangle\chi'_{\rm sat}$ and $\triangle\chi''_{\rm peak}$ are the highest-quality measurements in the data; nonetheless, note the difficulty in resolving the details of the transition far away from resonance.

communicated the high strategic value of frequency-dependent measurements for falsifying microscopic models, and presented an analysis which will be useful for future experiments. In addition, the measurements shown in Fig. 3.3 directly verify that the susceptibility measured on-resonance is free from phase-locked-loop artifacts.

3.2 Rotational susceptibility on-resonance

While observations on-resonance obviously cannot probe the frequency dependence of solid ^{4}He inertia, such operation does vastly increase the S/N over direct measurement methods. The helium susceptibility perturbs the resonance condition in a predictable way, which is now derived by two methods: one which matches the compact notation of Sec. 3.1 (including the frequency coupling p) and one which rolls p into the coupling constant as in [36].

3.2.1 On-resonance perturbation, method I.

To solve Eq. 3.7 for the expected frequency shift and added dissipation measured on-resonance, the susceptibility (ignoring Q_{osc}^{-1}) is expanded by a complex perturbation about the resonance, where $\delta(T)$ represents a possible superfluid term as given by Eq. 3.10:

$$\begin{cases} \dfrac{\chi^{-1}(T)\big|_{\omega_R}}{I_{\text{osc}}\left(1-\delta_{T\to 0}\right)} = 0 = \omega_0^2 - \left[1+\delta(T)\right]\omega_R^2 - \dfrac{C_p\omega_R^p}{1-i\omega_R\tau(T)} \\ \\ \omega_R = \omega_0\left[1+\epsilon(T)\right], \qquad \epsilon(T) = \dfrac{\triangle\omega(T)}{\omega_0} - \dfrac{i}{2}\triangle Q^{-1}(T) \end{cases} \tag{3.15}$$

Dropping explicit temperature dependencies where they are obvious, Eq. 3.15 can be rewritten as follows:

$$\left[1-(1+\delta)(1+\epsilon)^2\right]\left[1-i(1+\epsilon)\omega_0\tau\right] = C_p\omega_0^{p-2}(1+\epsilon)^p \tag{3.16}$$

which leads to more transparent algebra than [36]. Discarding terms which are quadratic or smaller in δ or ϵ, one can rearrange Eq. 3.16 to find the complex

frequency shift $\epsilon(T)$:

$$-2\epsilon(T) = \delta(T) + C_p\omega_0^{p-2}\frac{1+i\omega_0\tau(T)}{1+\omega_0^2\tau^2(T)} \tag{3.17}$$

Note that since ω_0 is constant and the observables do not otherwise explicitly depend on p (we do not know C_p independently), it is impossible to use single-frequency observations to determine the type of dissipative physics involved. The complex resonant perturbation can be split into the following useful conjugate parts for comparison to measurements:

$$\begin{aligned} -2\frac{\triangle\omega(T)}{\omega_0} &= \delta(T) + \frac{C_p\omega_0^{p-2}}{1+\omega_0^2\tau^2(T)} \\ \triangle Q^{-1}(T) &= \left(C_p\omega_0^{p-2}\right)\frac{\omega_0\tau(T)}{1+\omega_0^2\tau^2(T)} \end{aligned} \tag{3.18}$$

which reduce to the Debye model (the predictions of [36]) for $\delta = 0$, $p = 0$ and $C_p = \frac{g_0}{I_{\text{osc}}}$ as given in Table 3.1. Figure 3.4 shows an inertial anomaly associated with the Debye susceptibility.

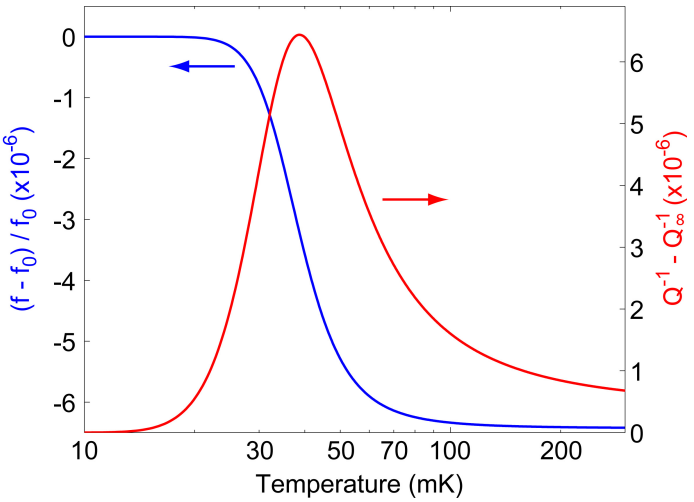

Figure 3.4: An inertial anomaly corresponding to the Debye susceptibility, given a particular $\tau(T)$. It contains several qualitative features in common with the Kim and Chan effect, albeit with some important discrepancies.

Analogously to Eqs. 3.11 and 3.12, one can now read off the saturated values:

$$-\frac{\triangle\omega_{\text{sat}}}{\omega_0} = -\frac{\triangle\omega\left(T\to\infty\right)}{\omega_0} = \frac{1}{2}\left(\frac{\rho_s^0}{\rho}\right)\frac{I_{\text{He}}}{I_{\text{osc}}} + \frac{C_p}{2}\omega_0^{p-2}$$
$$\triangle Q^{-1}_{\text{peak}} = \triangle Q^{-1}\left(T_*\right) = \left(\frac{1}{2\omega_0^2}\right)C_p\omega_0^p \tag{3.19}$$

From Eq. 3.19 and our low-noise resonant measurement of the dissipation peak (see Fig. 4.1) we can measure of the putative value of $C_p\omega_0^p$ (though this does not independently constrain p):

$$C_p\omega_0^p = 2\omega_0^2\left(\triangle Q^{-1}_{\text{peak}}\right) \approx 2\text{x}10^2\, s^{-2} \tag{3.20}$$

which corresponds to a dissipative back-action roughly 0.3% the magnitude of the BeCu/Stycast torsion oscillator strength.

3.2.2 On-resonance perturbation, method II.

Since single-frequency detection cannot distinguish p as discussed above, we can simply choose a p-independent form of the back action $\chi_D^{-1}(\omega, T)$ as follows (see [36] and Eq. 3.4):

$$\chi_D^{-1}\left(\omega, T\right) = \frac{g_0}{1 - i\omega\tau\left(T\right)} \tag{3.21}$$

the subscript "D" in this particular model of the back-action is not an accident; this classic Debye susceptibility describes the freezing out of an ensemble of excitations at a temperature T_* such that $\omega\tau\left(T_*\right) = 1$. In this case, we find that the real and imaginary parts of Eq. 3.21 are (for $\omega = \omega_0$)

$$\Re\left[\chi_D^{-1}\left(T\right)\right] = \frac{g_0}{1 + \omega_0^2\tau^2} \tag{3.22}$$

$$\Im\left[\chi_D^{-1}(T)\right] = \frac{g_0\omega_0\tau}{1+\omega_0^2\tau^2} \tag{3.23}$$

Experimentally, we do not track directly the susceptibility (Eq. 3.2) at the fixed frequency ω_0, but rather we measure the small deviation of the resonant frequency $f(T)$ from its low-temperature rigid-body value $f_0 = \omega_0/2\pi$, as well as the accompanying peak in the dissipation $D(T)$. Unsurprisingly, perhaps, the quantities $f(T)$and $D(T)$ are related in a simple way to the real and imaginary parts of the rotational susceptibility within the Debye model, and indeed within any model that responds at a single mode frequency τ^{-1} (see, e.g., the viscoelastic model of Ref. [42]).

The resonant frequency and dissipation are the real and imaginary parts of the complex frequency $\tilde{\omega}$, which is a pole of the function χ and therefore the solution to the equation $\chi^{-1}(\tilde{\omega}) = 0$. Setting Eq. 3.2 equal to zero at $\omega = \tilde{\omega}$, we see that it becomes a cubic equation for $\tilde{\omega}$. Since the contribution to χ from the solid helium is a small perturbation to the total susceptibility, we consider a form of $\tilde{\omega}$ that is linearized about the low-temperature solution $\omega_0 = \sqrt{\frac{K}{I}}$,

$$\tilde{\omega} = \omega_0 + ix + y, \quad |ix+y| \ll \omega_0 \tag{3.24}$$

and expand to linear order in x and y, giving

$$\tilde{\omega^2} = \omega_0^2 + 2i\omega_0 x + 2\omega_0 y \tag{3.25}$$

$$\tilde{\omega^3} = \omega_0^3 + 3i\omega_0^2 x + 2\omega_0^2 y \tag{3.26}$$

If we substitute these expressions into the cubic equation for$\tilde{\omega}$, we end up with two equations (for $\Re(\tilde{\omega})$and $\Im(\tilde{\omega})$) in two unknowns (x and y). Solving for x and y we find that

$$x = -\frac{g_0}{2I\omega_0}\frac{\omega_0\tau}{\left(1+\omega_0^2\tau^2\right)}, \qquad y = -\frac{g_0}{2I\omega_0}\frac{1}{\left(1+\omega_0^2\tau^2\right)} = \frac{x}{\omega_0\tau} \tag{3.27}$$

Using these expressions we can write our observables, the resonant frequency f and the dissipation D, as

$$f = \frac{\Re\left(\tilde{\omega}\right)}{2\pi} = f_0 + \frac{y}{2\pi} \tag{3.28}$$

$$D = \left|\frac{2\Im\left(\tilde{\omega}\right)}{\Re\left(\tilde{\omega}\right)}\right| \approx D_\infty + 2\frac{|x|}{\omega_0} \tag{3.29}$$

In the last line, we added back the contribution to the dissipation from $\gamma = I\omega_0 D_\infty$. It is these expressions that we fit to our data, in slightly more convenient form as shown in Eqs. 4.4 and 4.5. All that is left unspecified for the Debye susceptibility is the specific temperature dependence which is inserted into the back-action. Generally, an Arrhenius form which slows the dissipative processes at low temperature gives acceptable fits to some parts of the inertial transition.

CHAPTER 4

EVIDENCE FOR A SUPERGLASS

4.1 Equilibrated inertial anomaly

We confirmed the now well-known Kim and Chan effect [8, 26] in our samples, to verify that they exhibit the typical inertial anomaly (frequency shift and dissipation peak) associated with the putative supersolid transition. Fig. 4.1 shows the equilibrated value of *f(T)* (blue circles) and dissipation $D(T) \equiv Q^{-1}$ (red triangles) for our typical sample; the change in *f(T)* between 300 mK and 10 mK would represent a "supersolid fraction" of 4.8% if the frequency shift is entirely ascribable to a superfluid decoupling.

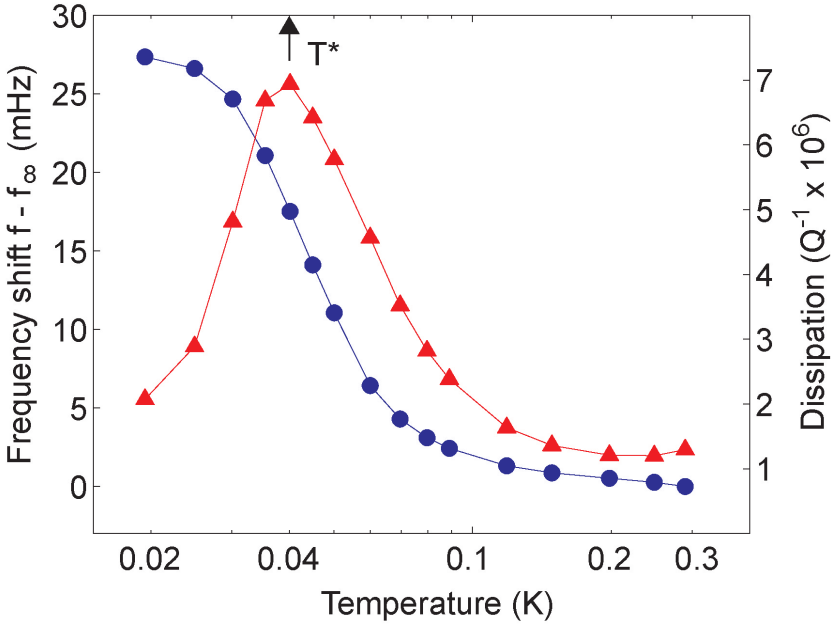

Figure 4.1: The resonant frequency shift $f(T) - f_\infty$ (blue circles) and dissipation $D(T) \equiv Q^{-1}(T)$ (red triangles) for our TO-solid ^{4}He system. Indicated with a black arrow is *T**, the temperature at which *D(T)* peaks and the slope of $f(T) - f_\infty$ is maximal.

Our samples, while formed by the 'blocked capillary' procedure and there-

fore amorphous, are of the type most widely studied in the field, and existence of the well-equilibrated inertial anomaly in Fig. 4.1 has now been verified by several groups around the world [27, 30, 28, 29]. We observed this thermally-equilibrated inertial anomaly at rim velocities slower than 4.5 microns/s, which was chosen to be slower than the onset of any appreciable velocity-dependent effects. The solid samples are grown from a high-pressure liquid (at ~75 bar and 4.2 K) with a nominal ^{3}He concentration of 300 ppb by the blocked capillary method, cooling rapidly along the melting curve (approximately 20 minutes from 4.2 K to < 1 K), and they typically reach a low-temperature pressure of ~36 bar (see sec. 2.1.4). Each measurement was acquired by waiting at the temperature of interest until the asymptotic equilibrated value of *f(T)* and *D(T)* was finally approached, which took several thousand seconds at the lowest temperatures. Equivalent effects were detected in four different samples studied in two different cells of this type.

4.2 Slow onset of the inertial anomaly

To examine the relaxational characteristics of solid ^{4}He, we perform the experiments outlined in Fig. 4.2. First, the temperature is reduced, typically in a 5 mK step, toward a new target temperature T_{eq}. We monitor the frequency and the dissipation during the temperature relaxation for $t < t_{eq}$; during this time the two quantities change at relatively fast rates until the temperature stabilizes at T_{eq}. For $T_{eq} < T_*$ (~60 mK), the frequency and dissipation then continue to relax at much slower rates after the temperature has come into equilibrium at the time t_{eq}; we record this relaxation $f\left(t, T_{eq}\right)$ and $D\left(t, T_{eq}\right)$ for approximately four hours after t_{eq}. More importantly, the subsequent changes after the ther-

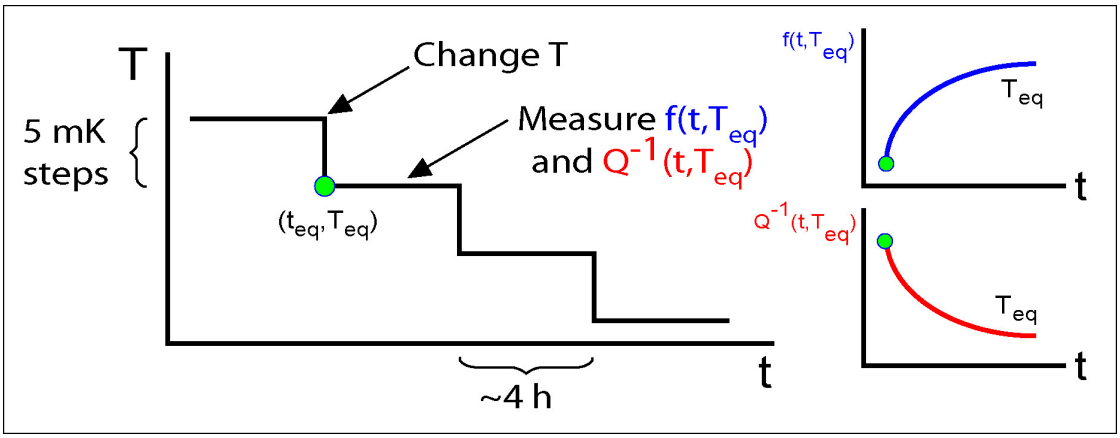

Figure 4.2: The schematic experimental procedure we used to observe the equilibration time of the inertial anomaly. The temperature is decreased stepwise from an initial temperature T_i to a final equilibrium temperature T_{eq} and the rapid co-evolution of f and D are observed as the thermometers approach T_{eq}.

mometers equilibrate: $f\left(t, T_{eq}\right)$ and $D\left(t, T_{eq}\right)$, are measured. We find that these phenomena are well fit by an exponential form for the first portion of the relaxation $(t < 10,000\,\mathrm{s})$and we report the characteristic times $\tau_f\left(T\right)$ and $\tau_D\left(T\right)$ for these relaxations in Fig. 4.5. There are more complex relaxation profiles $f\left(t, T_{eq}\right)$ and $D\left(t, T_{eq}\right)$ for much longer times which are not shown in Fig. 4.4.

Actual experimental traces of the temperature profiles corresponding to those illustrated schematically by Fig. 4.2 are shown in Fig. 4.3. The temperature is automatically controlled at each T_{eq} of interest. For compactness, subsequent experiments are plotted in a cascade, and the coldest experiments (each of which actually run longer than 14 hours) are truncated at 4,000 s. Automated thermal feedback control gives typically better than 0.8 mK RMS fluctuations of the mixing chamber temperature.

Data from five representative experiments are shown in Fig. 4.4 with each trace offset by 5000 seconds for clarity. In Fig. 4.4A the vertical axis represents the percentage of the total frequency change during each experiment. In

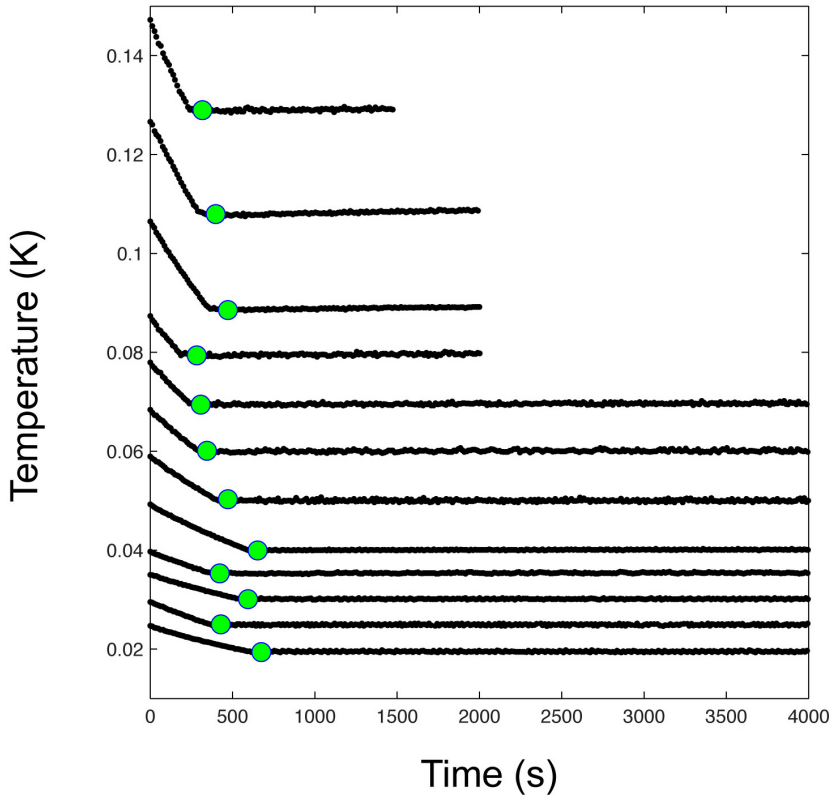

Figure 4.3: Mixing chamber temperature profiles during the experiments used to observe the slow onset times of the inertial anomaly. The green dots denote the time t_{eq} at which the mixing chamber temperature equilibrates.

Fig. 4.4B it represents the percentage of the equivalent total dissipation change. The green circles denote the time t_{eq} at which the mixing chamber temperature equilibrates, as recorded in Fig. 4.3. While for the initial $t < t_{eq}$ part of each trace both $f(t)$ and $D(T)$ change rapidly with temperature, their slopes change sharply at t_{eq} indicating that the solid inside the TO maintains thermal equilibrium with the mixing chamber. The traces are normalized according to

$$\delta f\left(t\right) \equiv \left[f\left(t, T_{eq}\right) - f\left(\infty, T_i\right)\right] / \left[f\left(\infty, T_{eq}\right) - f\left(\infty, T_i\right)\right]$$

$$\delta D\left(t\right) \equiv \left[D\left(t, T_{eq}\right) - D\left(\infty, T_i\right)\right] / \left[D\left(\infty, T_{eq}\right) - D\left(\infty, T_i\right)\right]$$

for comparison at different temperatures T_{eq}. Before the 'supersolid' signature appears, Fig. 4.4 reveals that these relaxation rates are independent of

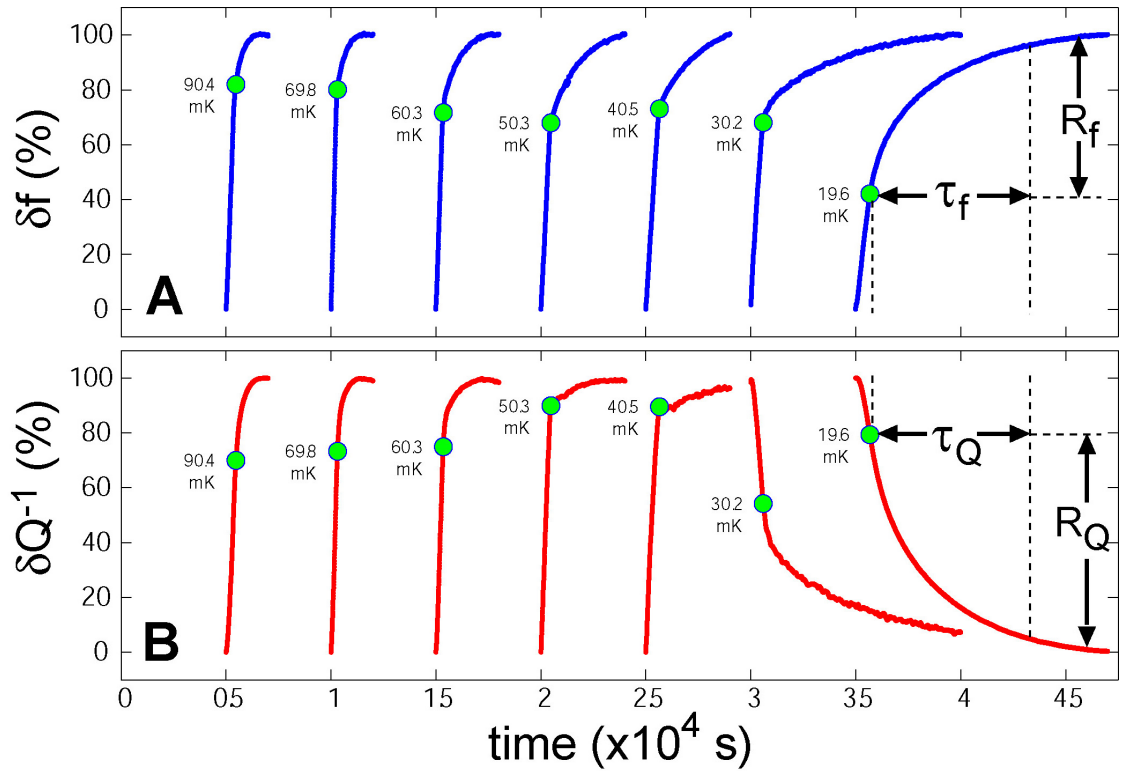

Figure 4.4: Measured traces of **(A)** $f\left(t, T_{eq}\right)$ and of **(B)** $D\left(t, T_{eq}\right)$ for the stepwise-cooling experiment described in the text and Figs. 4.2 and 4.3.

temperature and less than 100 s. But below the onset temperature they begin to increase rapidly. The time constants for relaxation processes in f and D, $\tau_f(T)$ and $\tau_D(T)$, are indicated schematically in Fig. 4.4 A and B. They are measured by fitting the exponential $f(t) = C_1 - C_2 \exp\left(-t/\tau_f(T)\right)$ and $D(t) = C_3 - C_4 \exp\left(-t/\tau_D(T)\right)$ to each trace for times $t > t_{eq}$. Both $\tau_f(T)$ and $\tau_D(T)$ increase rapidly on indistinguishable trajectories (see Fig. 4.5), indicating that the ultra-slow relaxation processes in f and D are intimately linked.

Such ultra-slow dynamics in the 'supersolid' state have also been observed elsewhere [35, 53, 54], and were also observed for acoustic properties by Goodkind's group [55]. It is difficult to reconcile any of these effects with thermal relaxation in a superfluid. Therefore a better understanding of the relaxation dynamics of amorphous solid ^{4}He is required.

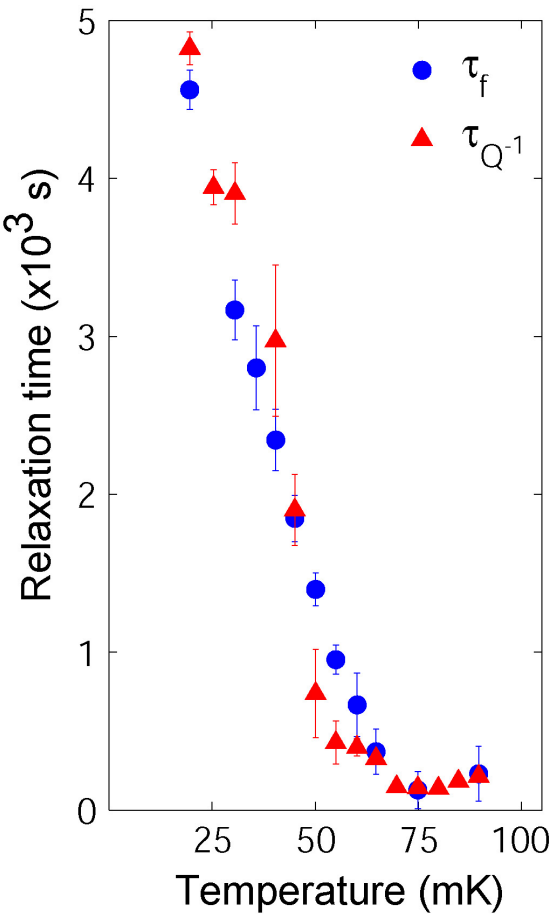

Figure 4.5: Measured temperature dependence of $\tau_f\,(T)$ and $\tau_D\,(T)$, the relaxation time constants for frequency and for dissipation as defined in the text.

4.3 Time-dependent formation of the inertial anomaly

We first examine the relationship between the relaxation dynamics of dissipation and the frequency shift - as both approach their long-time equilibrium states. It is clear from the responses seen in Fig. 4.4 that stepping the temperature directly between adjacent temperatures of interest T_{eq} as in Fig. 4.3 causes the total response to represent the convolutions of time-dependent responses at each previous temperature. Therefore this procedure, while sufficient to extract the magnitude of the time dependence of the inertial anomaly onset (Fig. 4.5), cannot be used to observe the pristine time-dependent evolution of the whole

inertial anomaly in Fig. 4.1.

Instead, the thermal history of each temperature step must be erased (by either annealing away or freezing out) before proceeding to the next temperature. Since our refrigerator cooling power is the limiting factor when trying to quickly change the temperature to lower values, we chose to erase the thermal history by freezing out the thermal history at low temperatures between each temperature step, and then quickly heating from that pristine cold state to each probe temperature T_{eq}.

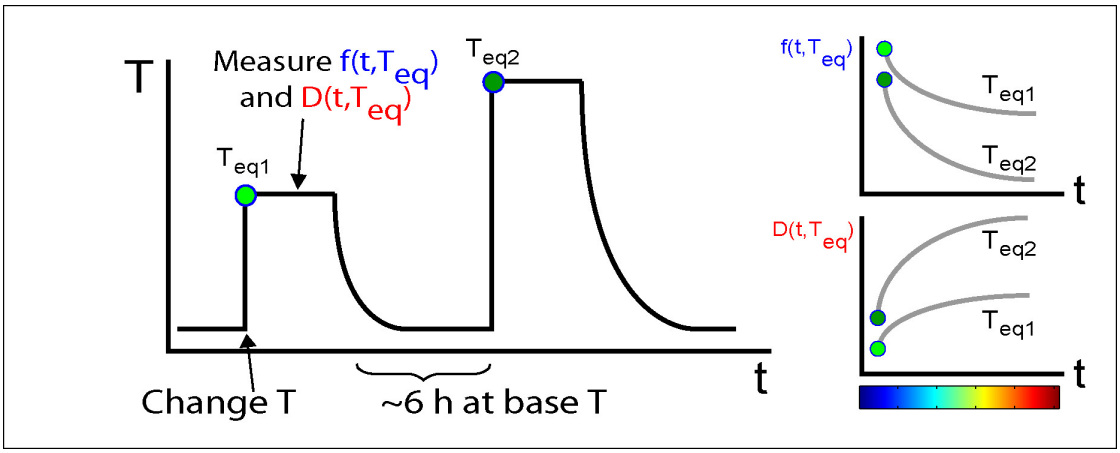

Figure 4.6: The experimental procedure whose results are shown in Fig. 4.7. The ^{4}He sample is cooled to 17 mK and equilibrated for a time $t > 20,000$ s. It is then heated abruptly to a temperature T and the subsequent relaxation dynamics in both $f(t,T)$ and $D(t,T)$ are monitored.

Specifically, (see Fig. 4.6), the system is prepared close to its ground state, equilibrating at low velocity and base temperature (about 17 mK) for more than 6 hours. The temperature is then raised abruptly to T_{eq1} and the frequency and dissipation relaxation $f(t,T_{eq1})$ and $D(t,T_{eq1})$ are recorded for several thousand seconds after the temperature has come into equilibrium. The system is allowed to cool back down to the base temperature and to return to the initial state, erasing the thermal history of the sample associated with inertial relax-

ations at T_{eq1}. The experiment is then repeated for a temperature $T_{eq2} > T_{eq1}$. In this way we are able to create a map of the evolution of the dissipation and the frequency shift due to the solid helium as a function of time after the system is thermally excited from its ground state. The color bar corresponds to the (increasing) times t_i associated with the curves $f\left(t_i, T_{eq1}\right)$ and $D\left(t_i, T_{eq1}\right)$ in Fig. 4.7, as well as with the Davidson-Cole plots at increasing times in Figure 4.11.

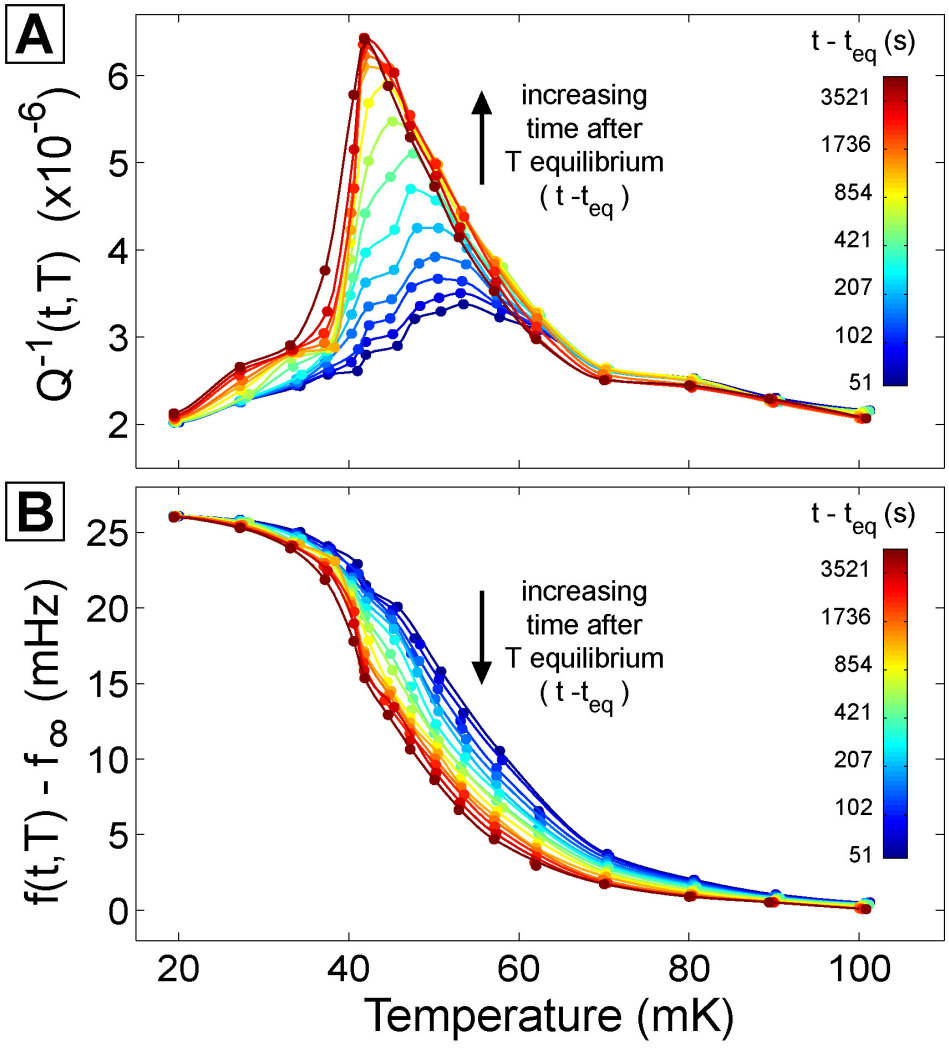

Figure 4.7: Measured time evolution of **(A)** $D\left(t, T\right)$ and **(B)** $f\left(t, T\right)$ for the abrupt warming experiment described in the text and Fig. 4.6. The data are colored circles and the lines are smooth interpolations, intended as a guide to the eye. The dark blue lines represent $D\left(t, T\right)$ and $f\left(t, T\right)$ at $t \sim 50\,\mathrm{s}$ while the dark red lines represent $D\left(t, T\right)$ and $f\left(t, T\right)$at $\sim 5,000\,\mathrm{s}$.

At short times after temperature stabilization, the dissipation increases slightly (dark blue in Fig. 4.7A). But these dissipative processes are actually very far out of equilibrium. As time passes, the dissipation slowly increases on a trajectory indicated by the transition from the blue line representing $D(t,T)$ at $t \sim 50\,\mathrm{s}$ to the dark red line representing $D(t,T)$ at $\sim 5,000\,\mathrm{s}$. In the same experiment, the time dependence of $f(t,T)$ is also measured (Fig. 4.7B). It differs from that of $D(t,T)$; at shortest times after stabilization at T the frequency has already changed greatly from its lowest temperature value (Fig. 4.7B). This means that much of the frequency change responds immediately to the mixing chamber temperature change (and therefore also that rapid thermal equilibrium always exists between the sample the mixing chamber thermometer). The subsequent evolution of the remaining component of the frequency shift exhibits an ultra-slow reduction in f as indicated by the transition from the blue line at$t \sim 50\,\mathrm{s}$ to the dark red line representing $t \sim 5,000\,\mathrm{s}$ in Fig. 4.7B. These data illustrate how the slowing relaxation dynamics within $f(t,T)$ and $D(t,T)$ are synchronized in such samples of solid ^{4}He.

They also imply that thermal hysteresis should occur when temperatures are swept faster than the relevant time constants in Fig. 4.7 A, B. Swept-temperature measurements on the same sample show in Fig. 4.8 that thermal hysteresis occurs in both $f(T)$ and $D(T)$, with their falling within the hysteresis loops as expected. The data indicated by red and blue circles were acquired after waiting $t \gg 5\text{x}10^3$ seconds at each temperature as the dynamical response (Fig. 4.7) asymptotically approached the infinite-time limit.

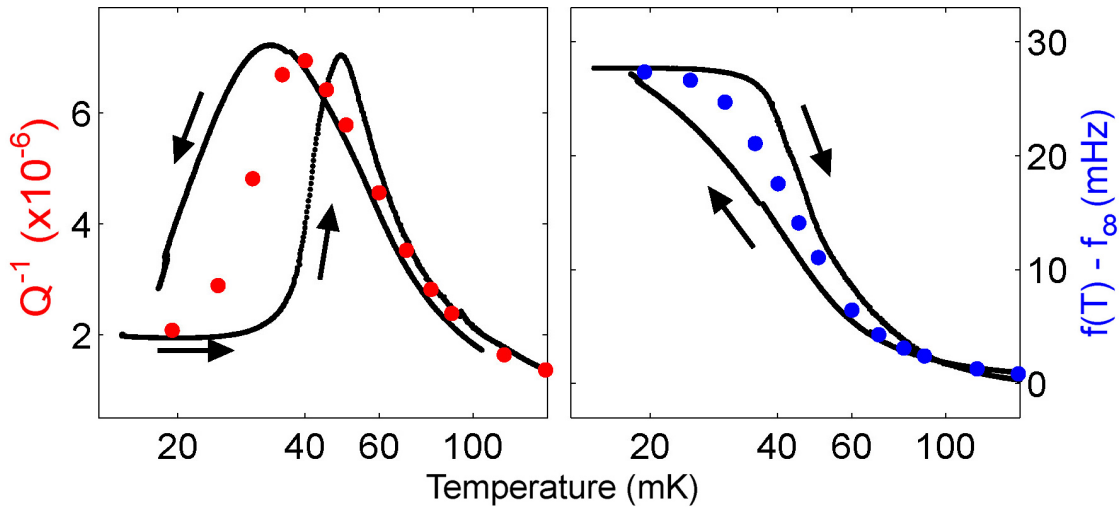

Figure 4.8: Thermal hysteresis in the dynamical response as shown by the black curves in $D(T)$ (left panel) and in $f(T)$ (right panel), with the direction of the temperature change indicated by a black arrow and the long-time equilibrium values (Fig. 4.1) by solid circles.

4.4 Glassy excitations

The extraordinary relaxation dynamics in $f(t,T)$ and $D(t,T)$ are unexpected in the context of a familiar superfluid. But effects analogous to these are seen during the freeze out of excitations at a dielectric glass transition [56, 1]. Thus the phenomenology of solid ^{4}He might also be due to a freeze-out of an ensemble of excitations within the solid [36]. In fact, the characteristic time dependence we observed in Fig. 4.4 is strongly reminiscent of the well-known responses of classical viscous glasses, as (for example) described in this excerpt from Brawer's book on such materials [1]:

Consider a sudden change in a thermodynamic variable, such as temperature, pressure, or strain, and let $p(t)$ be the subsequent variation of a property, such as index of refraction, enthalpy, or stress. The variation of $p(t)$ with time is shown in the inset to [Fig. 4.9]. A nearly instantaneous change occurs, due mainly to change in the lattice vibrations, but also to some very fast relaxations, during which the value of p jumps to p_1. (In fact, all changes which occur on a time scale much faster than the time resolution may be incorporated into this segment of the change.) Following this rapid change is a much slower variation of the property, on a time scale very roughly equal to the shear relaxation time (determined by the shear viscosity).

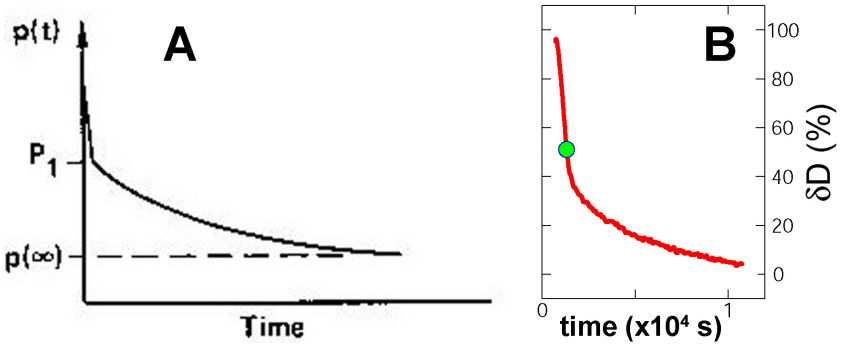

Figure 4.9: **(A)** Typical time-dependent response $p(t)$ of a viscous glass after changing a thermodynamic variable - adapted from Fig. 3-3 in Brawer [1]. **(B)** Typical solid helium dissipation response to a temperature change (see Fig. 4.4).

In addition to the obvious visible similarity between Fig. 4.9A and 4.9B, the fast component of the response of solid helium (which occurs before the green dot) indeed corresponds exactly to the time-dependent portion of its thermal bath temperature (see Fig. 4.3), analogous to the fast response of mainly lattice vibrations (i.e. thermal phonons) in classical glasses [1]. This qualitative match between the response of classical viscous glasses and the response of solid helium begs for a better better understanding of the relaxation dynamics of amorphous solid ^{4}He, especially in light of the dramatic blocked-annulus phenomena observed in helium [8, 49] that are certainly not expected to occur in a classical glass.

4.4.1 Susceptibility of a simple freeze-out transition

Indeed there have been numerous proposals [43, 44, 45, 46] that solid ^{4}He is a 'superglass' – some form of granular superfluid within an amorphous solid.

To examine such hypotheses, we consider the total rotational susceptibility $\chi(\omega, T)$ of the TO plus solid ^{4}He sample [36]. A classic Debye susceptibility describing the freeze-out of an ensemble of identical excitations with decay time $\tau(T)$ is

$$\chi_D^{-1}(\omega, T) = g_0 / (1 - i\omega\tau(T)) \tag{4.1}$$

For solid ^{4}He, g_0/ω_0^2 would represent the rotational inertia associated with the relevant excitations. Their 'back action' on the TO would appear in the total susceptibility as $\chi^{-1}(\omega, T) = K - I\omega^2 - i\gamma\omega - g_0/(1 - i\omega\tau(T))$ where γ is the intrinsic damping constant of the TO. The effect of changing the temperature can be captured entirely by the Debye term χ_D^{-1}, whose real and imaginary parts are

$$\Re\left[\chi_D^{-1}(T)\right] = \frac{g_0}{1 + \omega_0^2\tau^2} \tag{4.2}$$

$$\Im\left[\chi_D^{-1}(T)\right] = \frac{g_0\omega_0\tau}{1 + \omega_0^2\tau^2} \tag{4.3}$$

at $\omega = \omega_0$. Thus, when one susceptibility component changes due to the $\tau(T)$ term, the other must always change in a quantitatively related fashion. Such changes are measurable because

$$\frac{2(f_0 - f(T))}{f_0} = \frac{1}{I\omega_0^2}\Re\left[\chi_D^{-1}(T)\right] \tag{4.4}$$

$$D(T) - D_\infty = \frac{1}{I\omega_0^2}\Im\left[\chi_D^{-1}(T)\right] \tag{4.5}$$

within the Debye model with suitable approximations (see Sec. 3.2). Moreover a well-defined characteristic temperature T_* for such a susceptibility occurs when

the dissipation rate matches the oscillator frequency at $\omega_0 \tau\,(T_*) = 1$; both the $f\,(T)$ slope and the dissipation $D\,(T)$ achieve their maxima at $T = T_*$ (see Fig. 4.1).

In Fig. 4.10 (left) we show a fit of Eq. 4.5 to the measured $D\,(T)$ as a red line while Fig. 4.10 (right) shows the resulting prediction from Eq. 4.4 for $f\,(T)$ as the blue line. For these fits, we assumed an Arrhenius thermal activation form $\tau\,(T) = \tau_0 \exp\,(\Delta/T)$ of the excitations, with parameters as listed. Comparison to the measured $f\,(T)$ (solid blue circles) shows that this Debye susceptibility is inconsistent with the relationship between $D\,(T)$ and $f\,(T)$. While the dissipation can be fit reasonably well by this model [36], the magnitude of the frequency shift which is then predicted is dramatically smaller than observed.

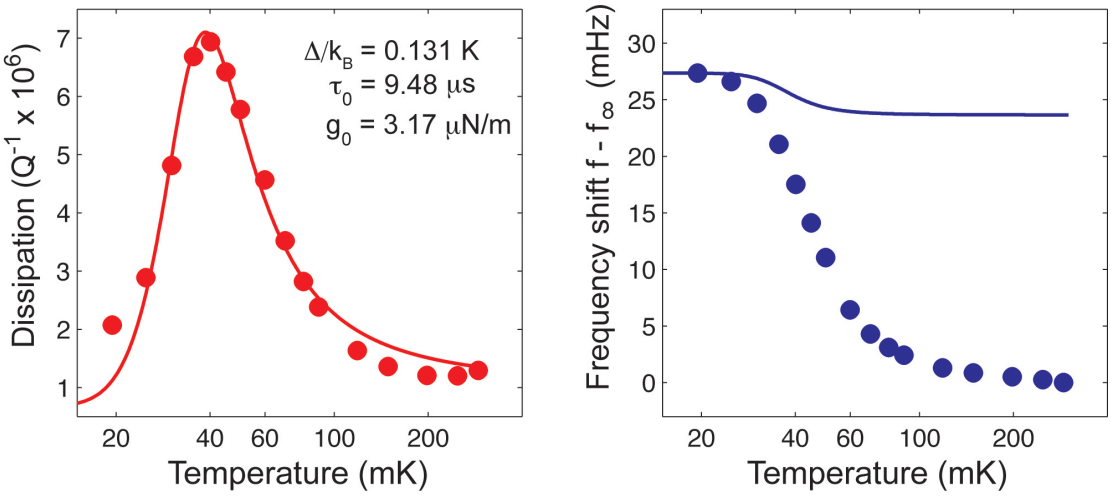

Figure 4.10: Comparison of equilibrated and data with simple Debye model of susceptibility in Eq. 1. The long-time equilibrated data (left) and (right) are plotted as filled circles.

4.4.2 Time-dependent Davidson-Cole analysis

Nevertheless, we have observed that the (low-velocity) frequency shift and dissipation peak are synchronized and share identical relaxational characteristics as a function of temperature. It seems natural, therefore, to consider whether these observables may be simultaneous consequences of an underlying physical mechanism. In such a scenario, we could expect the temperature to appear as a parametrization between the real and imaginary components of the oscillator's rotational susceptibility.

A tool commonly used to illuminate this type of relationship is a direct plot of the imaginary vs. real components of a susceptibility in the complex plane. When used in the context of the dielectric susceptibility of classical glasses or polarized liquids, this is called a Cole-Cole or Davidson-Cole (D-C) plot [57, 58]: the plot is the locus of points $(\Re[\varepsilon], \Im[\varepsilon])$ and the implicit parameter is typically the measurement frequency ω. In our experiment, by contrast, we fix the measurement frequency at the resonant frequency of the system $\omega = \Re(\tilde{\omega})$ and we vary the resonant response of the system at τ^{-1} by varying the temperature. The analogous plot to $(\Re[\varepsilon], \Im[\varepsilon])$ would be the locus of points $\left(\Re\left[\chi^{-1}\right], \Im\left[\chi^{-1}\right]\right)$. In the context of quantum fluids experiments, Bowley, Saunders, and collaborators used this method of analysis in comparing superfluid thin-film vortex unbinding observations with detailed theories of the Kosterlitz-Thouless transition, obviating the need for free parameters to fit any temperature-dependent terms. [4, 59]. The D-C plot is important conceptually because it displays information about the linear response of the system without favoring one implicit variable over another.

As a practical tool, it is also essential. First, in the case of the rotational sus-

ceptibility of the TO-helium system, it eliminates the need for specific models of the relaxation time $\tau(T)$. Second, deviations from the Debye susceptibility appear as prominent geometric features in the D-C plot. The Debye susceptibility (Eq. 3.21) becomes a semicircle centered on $X \equiv \Re\left[\chi^{-1}\right] = g_0/2$ and with radius $g_0/2$, as can be seen from taking the real and imaginary parts of Eq. 3.21 and eliminating $\omega_0\tau$ from the resulting equations. One finds (with $Y \equiv \Im\left[\chi^{-1}\right]$):

$$\left(X - \frac{g_0}{2}\right)^2 + Y^2 = \left(\frac{g_0}{2}\right)^2 \tag{4.6}$$

We know from the separate temperature-dependent fits to Eqs. 4.4 and 4.5 (Fig. 4.10) that the Debye susceptibility is a poor model for our data, but why exactly? To answer this question, we would like to compare our data to the semicircular D-C plot (Eq. 4.6) of the Debye susceptibility. Equations 3.22 and 3.23 suggest the natural abscissa and ordinate for a Davidson-Cole plot: Eqs. 4.4 and 4.5. This is clear because if our data were correctly described by the Debye susceptibility, then a plot of $2\frac{\Delta f}{f_0}$ vs. ΔD vs. would appear as a semicircle. In fact, as already anticipated from the failure of Eqs. 4.4 and 4.5 simultaneously to fit our data, the situation is quite different.

We therefore plot $D(T) - D_\infty$ versus $\dfrac{2\left(f_0 - f(T)\right)}{f_0}$ in Fig. 4.11. It reveals that, instantaneously upon warming, the D-C plot is a symmetric elliptical curve, whereas after several thousand seconds the response has evolved into the skewed D-C curve more familiar from studies of the dielectric glass transition [56]. But the maximum frequency shift expected from the maximum observed dissipation within the Debye susceptibility (vertical dashed lines) is again far too small. Moreover, no temperature equilibration lag between the solid ^{4}He sample and the mixing chamber could generate the complex dynamics reported in Fig. 4.11 because, for any given frequency shift f, a wide variety of different (and non-

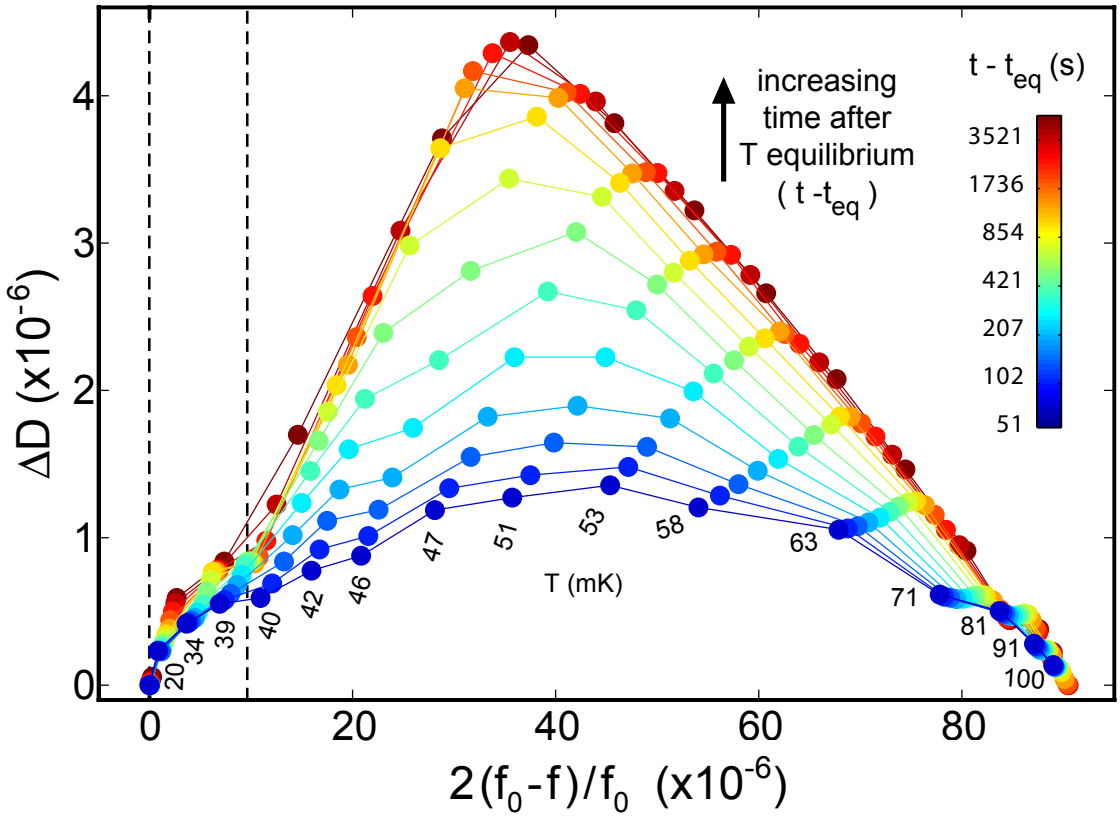

Figure 4.11: The time-dependent Davidson-Cole plot of the solid helium inertial anomaly. Mixing chamber temperature (in mK) is indicated by a text label below the starting (blue) point of each time-dependent acquisition. Time after equilibration is indicated by the color bar. The dashed lines indicate the maximum real susceptibility shift expected for a simple non-superfluid Debye freeze-out transition that matches the observed peak dissipative strength; the real susceptibility anomaly of solid helium clearly exceeds this bound.

monotonic) dissipation magnitudes D are observed.

As mentioned above, departures from the simple Debye susceptibility appear as prominent geometric features in the D-C plot. As one important example, consider a glassy susceptibility in place of the Debye susceptibility, which represents the linear response over a distribution of relaxation times (instead of a single relaxation time τ). Formally, this is obtained by the substitution

$$\frac{1}{1-i\omega_0\tau} \rightarrow \frac{1}{(1-i\omega_0\tau)^{\beta}} \tag{4.7}$$

with $0 < \beta < 1$. It is straightforward to show (using the notation of Sec. 3.2.1) that this back-action leads to the following predicted susceptibilities:

$$X(T) = -2\frac{\triangle f}{f_0} = C_p \omega_0^{p-2} \left(1 + \omega_0^2 \tau^2(T)\right)^{-\frac{\beta}{2}} \times \cos\left(\beta \tan^{-1}\left[\omega_0 \tau(T)\right]\right) \quad (4.8)$$

$$Y(T) = \triangle Q^{-1} = C_p \omega_0^{p-2} \left(1 + \omega_0^2 \tau^2(T)\right)^{-\frac{\beta}{2}} \times \sin\left(\beta \tan^{-1}\left[\omega_0 \tau(T)\right]\right) \quad (4.9)$$

If $\beta \neq 1$, parametric plots of Y vs. X are manifest as *skewed* (i.e. non-elliptical) curves in the D-C plot (see Fig. 4.12B below). $C_p \omega_0^p$ may be replaced by g_0 / I_{osc} for single-frequency measurements, which is the slightly more compact notation as used from now on.

We have shown in Fig. 4.7 that the susceptibility of the TO-solid helium system is time-dependent on extremely long (glassy) time scales. We therefore expect the susceptibility to be representable in a time-dependent D-C plot. Fig. 4.12A shows the time-independent version of the D-C plot of the glassy susceptibility (Eq. 4.7) and Fig. 4.12 B and C illustrate two different possibilities for the ways in which the glassy susceptibility (Eq. 4.7) might give a time-dependent D-C plot. A model in which both g_0 and β change as a function of time (see Fig. 4.12C) allows the height of the t-d D-C plot to increase as well as for skew to develop as a function of time, which captures some of the features of Fig. 4.11, but not all.

Quite simply, there are two parameters, g_0 and β that can affect the total magnitudes of the real and imaginary parts of the susceptibility and therefore the range, domain and shape of the D-C plot. In Fig.4.12B we allow only β to vary with time, keeping g_0 constant. It is clear that such a model cannot describe our Fig. 4.11 data accurately; in this model, the height of the D-C plot decreases with time, whereas in Fig. 4.11 the height clearly increases with time.

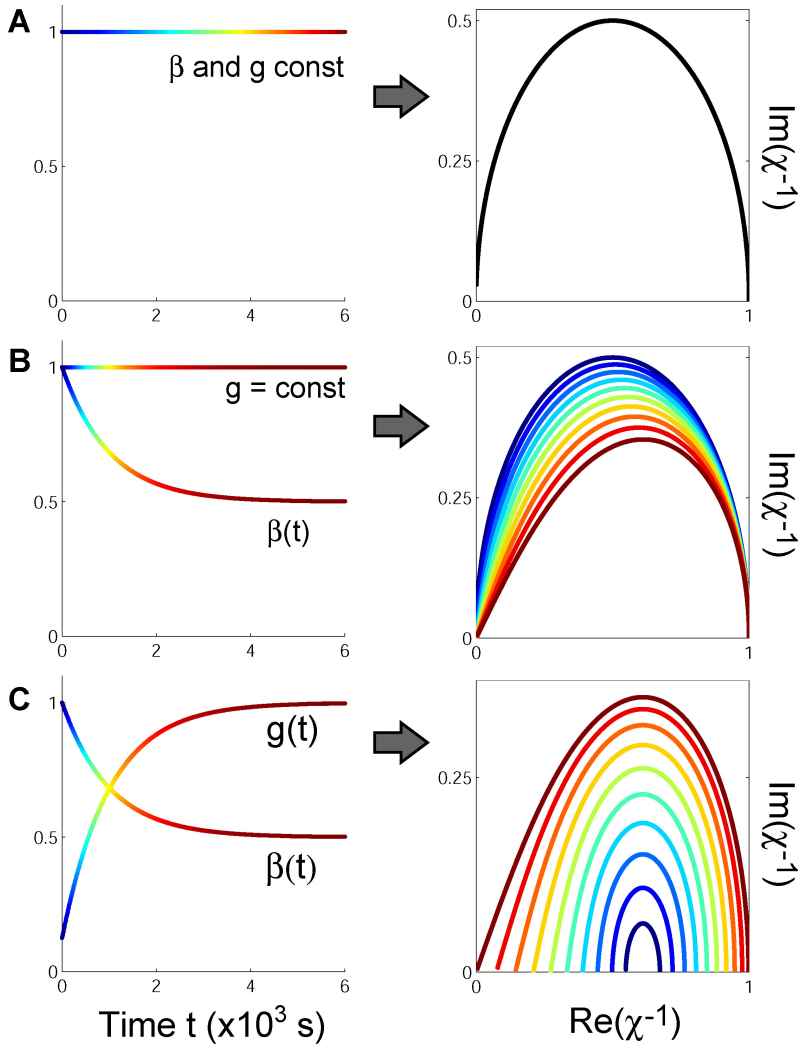

Figure 4.12: Three models of the time dependence of the two parameters, g_0 and β, of a glassy susceptibility (left figures) and their corresponding time-dependent Davidson-Cole (t-d D-C) plots (right figures). The color scale corresponds to the same one as Fig. 4.7; blue to red is increasing time.

The model in Fig. 4.12C allows g_0 to increase and β to decrease with time and captures some of the essential features of the time-dependent susceptibility that we measure: the height of the D-C plot increases with time and the skew increases as well. (For clarity, the curves in Fig. 4.12C are offset so that they are centered at the same point on the x-axis). However, the central question to this section remains: what can account for the disproportionately large extent

of the D-C plot along the real axis and why does it not appear to change with time? A naive argument is that most of the frequency shift is due to a superfluid component of the solid helium coexisting with (and whose phase stiffness is apparently controlled by) the glassy component - see Sec. 4.7.1.

A simple superfluid transition is inconsistent with all these observations because there should be no synchronized dissipation peak associated with $f(T)$ (Fig.'s 4.1, 4.11) and no ultraslow dynamics in $D(T)$ and $f(T)$ (Fig.'s 4.4, 4.7).

4.5 Other non-supersolid interpretations

Other microscopic models have been suggested, most of which focus on predicting the low-velocity real susceptibility anomaly in solid helium. The functional form of several of these will be presented in this section, with a comparison to both the Debye susceptibility predictions for the inertial transition and to data we acquired (using a similarly prepared sample as in Fig. 4.11).

4.5.1 Vortex fluid

Based on Anderson's suggestion [39] that the solid helium inertial anomaly is generated by the physics of a vortex fluid interpenetrating the lattice, it was extrapolated that some features of the well-known vortex liquid phases in superconductors and turbulent superfluids may be observed analogously in the dynamics of solid helium [29, 60]. In particular, a turbulent vortex fluid was suggested [60] to give rise to a low-velocity frequency shift f given by a Langevin

equation as a function of $x = \frac{1}{T^2}$ as follows:

$$f(x) = a\left[\frac{\exp(bx) + \exp(-bx)}{\exp(bx) - \exp(-bx)} - \frac{1}{bx}\right] \tag{4.10}$$

where a is a fitting parameter that controls the magnitude of the saturated low-temperature frequency shift, and b is a fitting parameter that controls the transition temperature. A plot of solid helium frequency shift vs. $x = \frac{1}{T^2}$ was provided by the Kubota group in the paper in which they suggested this correspondence, for high-temperature data which extended to $x \lesssim 450\,\mathrm{K}^{-2}$, with a good fit to the curve given by Eq. 4.10 in that temperature range. We too find that Eq. 4.10 gives good agreement to our data over the same temperature range, as illustrated in Fig. 4.13, but it fails to fit the data at lower temperatures.

4.5.2 Two-level systems

Andreev proposed [37] that the inertial anomaly in solid helium is generated by a population of tunneling two-level systems (TLS) that collectively give rise to a momentum deficit that appears as a decrease in rotational inertia at low temperature. The susceptibility for such a model was subsequently worked out explicitly by Korshunov [38] and Andreev [61], and for free TLS at low velocity, is of the following functional form:

$$f(T) = A\tanh\left(\frac{B}{T}\right) \tag{4.11}$$

where A and B are suitable fitting parameters. This prediction is plotted against our data in Fig. 4.13 and does not give particularly good agreement. However, the TLS model does have the advantage of an explicit prediction for the susceptibility dependence on velocity, which will be revisited later in this dissertation.

4.5.3 Comparison with observations of solid helium

The models given by equation 4.10 (in two versions with different fitting constraints), equation 4.11, and equation 4.2 on page 46 (the Debye susceptibility for the low-velocity frequency shift, assuming $\tau(T)$ is Arrhenius activated) are plotted in Fig. 4.13, along with well-equilibrated low-velocity solid helium frequency shift observations. Of these models, only the Debye susceptibility also gives an explicit prediction for the dissipation, which agrees with the qualitative shape of the dissipation peak but not with its magnitude, as indicated by Fig. 4.10 on page 47 and Table 4.1 on page 60.

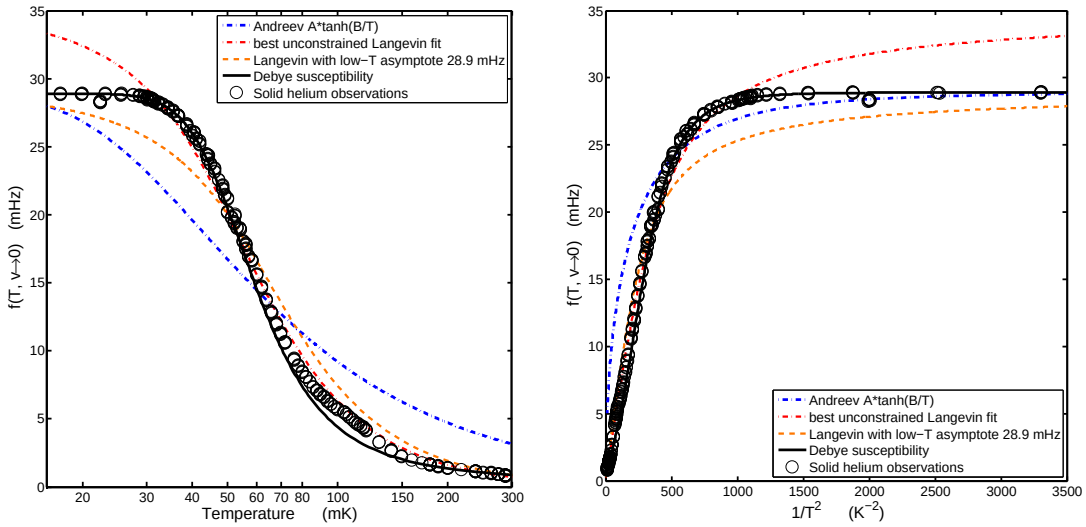

(a) Logarithmic temperature axis.

(b) Temperature axis shown as $\frac{1}{T^2}$.

Figure 4.13: Several models of a low-velocity inertial anomaly compared to the observed solid helium TO frequency shift.

4.6 Vortex unbinding (thin superfluid film) interpretation

Of course, it is possible for a more complicated superfluid transition to display a synchronized dissipation peak, as is well known in the 2D liquid thin film Berezenski-Kosterlitz-Thouless (BKT) transition [62, 63, 3, 64, 2]. The well-known inertial signature of such a transition, from the famous paper by Bishop and Reppy [2] is replotted for reference here in Fig. 4.14.

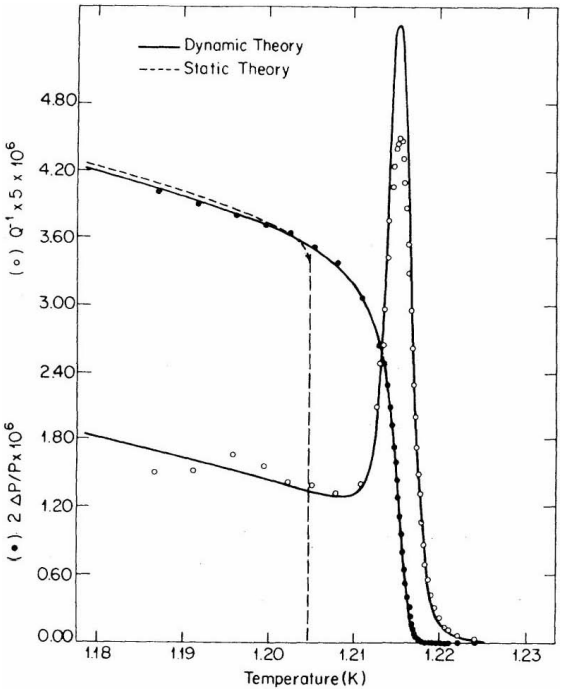

Figure 4.14: The well-known dissipation and frequency shift signatures of the thin-film BKT transition, from [2].

Though there are some qualitative similarities between thin liquid films (Fig. 4.14) and the solid helium inertial signature (Fig. 4.1), the shape of the curves are obviously different. To make a more detailed comparison between the two physical phenomena, we apply the same Davidson-Cole analysis to the BKT transition in Fig. 4.15, which shows thin-film data from [3] and [2] as solid black symbols, scaled in magnitude to overlay the solid helium data from Fig. 4.11.

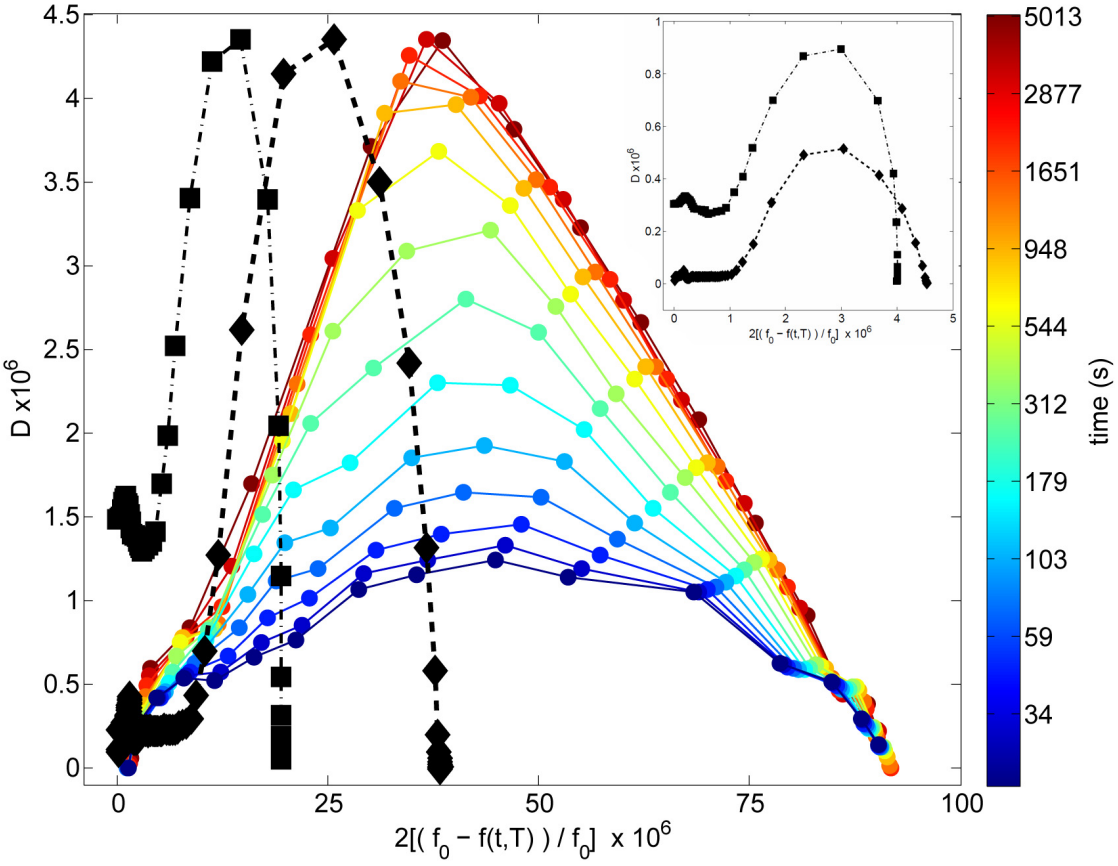

Figure 4.15: The well-known dissipation and frequency shift signatures of the thin-film BKT transition (black symbols); scaled to overlay the solid helium dynamics. Color scale for solid helium data as in Fig. 4.11. Black diamonds are data from Agnolet [3] (acquired at constant drive); black squares are data from Bishop and Reppy [2] (acquired at constant amplitude). The inset shows both sets of raw (unscaled) thin-film BKT data.

One particularly interesting characteristic to notice in Fig. 4.15 is that the transition region of the thin liquid film inertia is described quite well by a mostly symmetric elliptical arc. (There is also a small flat tail in the low-temperature region, where the real inertia starts to increase without accompanying change in the dissipation. The tail is attributable to the temperature dependence of the background superfluid density.) This is in contrast to the long-time behavior (red data) of solid helium, which is highly skewed away from a symmetric elliptical arc. In addition, there is an obvious discrepancy in magnitudes between

the dissipation peak and the frequency shift of liquid films, if one attempted to model the quasi-elliptical arc of the BKT transition as caused by a single Debye mode. This is similar to (although less pronounced than) the magnitude discrepancy we observed in solid helium, and which we interpret as being consistent in both cases with the existence of a superfluid component that dominates the magnitude of the real response. Indeed, there is even a magnitude discrepancy in the classic thin film observations [4], compared to the full dynamic AHNS theory, although it is less pronounced than either the discrepancy in solid helium or the discrepancy generated by a Debye model.

The inclusion of a probability distribution function for each vortex pair-separation distance in a thin superfluid film inertial transition [59] is analogous to the inclusion of a probability distribution of relaxation times in a glassy susceptibility (as in Fig. 4.12). Both types of non-single-mode theories generate characteristic skew in the D-C plot of the susceptibility. Skew can also be generated by inclusion of finite-size effects, as is shown in Fig. 4.16 adapted from the Saunders paper [4]. Based on the qualitative appearance of skew due to the inclusion of a distribution of vortex pairs and/or finite-size effects, it is therefore natural to ask whether such a distribution might be able to describe the inertial anomaly in solid helium.

Indeed, it has been proposed that the supersolid anomaly could in fact be a finite-size BKT transition of thin liquid films presumably confined to grain boundaries within the solid [65]. And, although such a picture can begin to reconcile some of the stark discrepancy between the shapes of the transitions in Fig. 4.14 and Fig. 4.1, it cannot begin to address the ultraslow relaxation dynamics of the inertia that we observed in solid helium (Fig. 4.7). While some

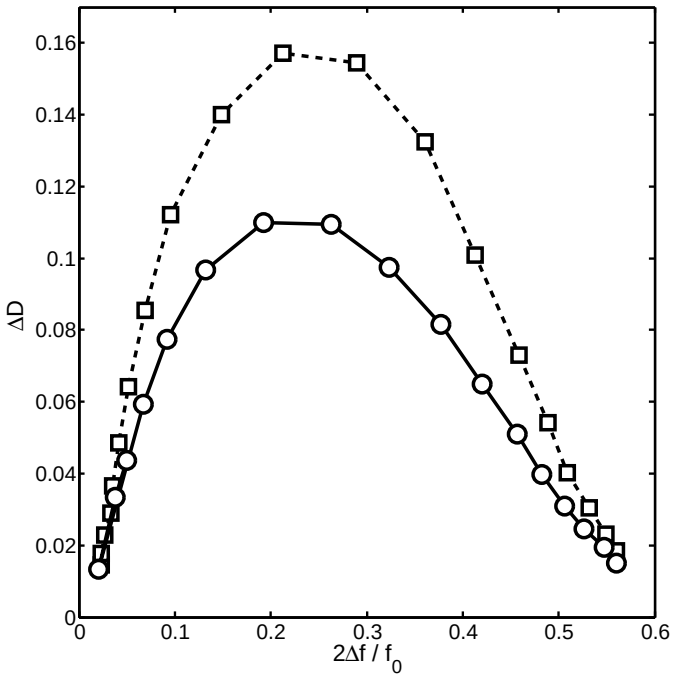

Figure 4.16: Skewed susceptibility predicted by a higher-order theory of the thin-film vortex inertial transition (circles) that includes finite-size effects. Unskewed AHNS theory is illustrated by the squares. Adapted from [4].

ultraslow (~week-long time constant) relaxations were observed in the overall background dissipation levels of the BKT transition [3], they were not observed to control the onset of the characteristic inertial curves themselves, and glass-like relaxations are not expected in the context of the BKT theory [62].

Furthermore, the extremely high value of the magnitude discrepancy between the saturated dissipation peak and inertial strength in the case of solid helium - along with the complete lack of skew in the D-C plot at short times after heating the sample - are inconsistent with even finite-size corrected theories of the BKT transition, as well as single-mode Debye freeze-out models. The magnitude discrepancies observed and predicted for various cases are summarized in table 4.1, where the skew is listed as "0" when it is not readily apparent.

In addition, the quality of the curve fits in [65] do not show unambiguous

Table 4.1: Discrepancies in the magnitude of the saturated inertial shift versus dissipation peak for various models and experiments.

Ref.	Source	Physical model	Skew	$\frac{\max(2\Delta f/f_0)}{\max(\Delta D)}$
[36]	theory	Single-mode Debye freeze-out	0	2 : 1
[58]	theory	Davidson-Cole glass, $\beta = \frac{1}{2}$	yes	3 : 1
[62, 4]	theory	2D vortex unbinding (AHNS)	0	4 : 1
[2]	expt.	Thin-superfluid-film at constant amplitude	small	5 : 1
[4, 59]	theory	2D vortex unbinding with finite-size effects	yes	5 : 1
[3]	expt.	Thin-superfluid-film at constant drive	0	9 : 1
Fig. 4.11	expt.	Solid helium, $t \to \infty$ after heating	yes	21 : 1
Fig. 4.11	expt.	Solid helium, shortly after heating	0	73 : 1
[58]	theory	Davidson-Cole glass, $\beta = 0.01$	extreme	73 : 1

agreement between finite-size BKT physics and the inertia of solid helium, and the thin films do not exhibit an ultraslow time-dependent onset of the inertial transition as solid helium does (Fig. 4.15) From these observations we conclude that the BKT physics of a thin liquid film superfluid transition is insufficient to explain the inertia of solid helium, although qualitative aspects of the model could plausibly agree better with solid helium data by combining vortex pairing physics with the ultra-slow dynamics of a conformational glass. The rotational susceptibility of such a mechanism within a solid helium lattice has not been theoretically established.

4.7 Superglass interpretation

In fact, these phenomena are reminiscent of the characteristics of a glass transition [56]. Nevertheless, a simple freeze-out of excitations described by a Debye susceptibility is also quantitatively inconsistent because the dissipation peak is far too small to explain the observed frequency shift (Fig. 4.10). Thus, when considered in combination with implications of the blocked annulus experiments [8, 49], our observations motivate a new hypothesis in which amorphous solid ^{4}He is a supersolid, but one whose superfluid phase-stiffness can be controlled by the freeze-out of an ensemble of excitations within the solid.

Within such a model, generation of excitations at higher temperatures would suppress superfluid phase stiffness. The complex relaxation dynamics (Fig. 4.7, 4.11) would reveal the excitation freeze-out processes. And the anomalously large frequency shifts (Fig. 4.11) would occur predominantly because of superfluid phase stiffness appearing subsequent to excitation freezing.

4.7.1 A model superglass

From the apparent onset of skew in Fig. 4.11, the picture which emerges from this interpretation is that the low-temperature ground state of solid helium is well described by a single overdamped dissipative mode (as reflected by the ellipticity of the $t \sim 50\,\mathrm{s}$ curve), whereas higher temperatures spread out the dissipative relaxation into many modes.

The internal relaxation *rate* of the dissipative modes in this interpretation appears to respond very rapidly to temperature, as the synchronized inertial

changes between f and D already trace out the characteristic shape of the Davidson - Cole form for a single mode (aside from the scale of f) even at the shortest times after raising the temperature. By increasing the temperature in this kind of model, τ (presumably related to the strain autocorrelation time) is rapidly swept down across the probe frequency ω of the oscillator so that at the higher temperatures, the inertial "supersolid" back-action is already decorrelated on the time scale of the measurement, i.e. $\omega\tau \to 0$. This picture also indicates the mechanism by which the inertia gains a frequency dependence (see [46]).

After the temperature has been raised, the dissipative motion which had been confined to the ground-state single mode, in this model slowly spreads out into a glassy distribution of modes (as reflected by the time-dependent increase in *skew* in Fig. 4.11), and the internal relaxation *amplitude* gradually increases as thermal energy is pumped into the spreading glassy modes. Because we observe that the total magnitude of the frequency shift is constant in time, it appears that if the large real part of the inertia is indeed dominated by a superfluid, its transport is directly extinguished by the the internal dissipative mode that couples to it. For illustration, we present one very simple encapsulation of this picture in Fig. 4.17, which includes the following features:

1. Time-dependent spreading of glassy modes as the temperature is raised (captured by a glassy exponent $\beta(t)$ that decreases from 1 (single mode) at low temperature and saturates at $\beta \to 1/2$ for long times (see Fig. 4.18)
2. Time-dependent dissipative back-action $g_0(t)$ that increases in magnitude as the glassy modes are populated and exponentially saturates at long times
3. A superfluid whose saturated inertia $\delta_0 I_{\mathrm{osc}}$ is entrained to the oscillator by

excitation of the dissipative modes (i.e. the total mass decoupling occurs only when the system is probed in the quasistatic limit - the oscillator frequency being much higher than the dissipative relaxation rate). We model this by modifying the term $X(T) \rightarrow X(T) + \delta_0 \left(1 + \omega_0^2 \tau^2(T)\right)^{-\beta}$ in the real susceptibility of Eq. 4.8 on page 51.

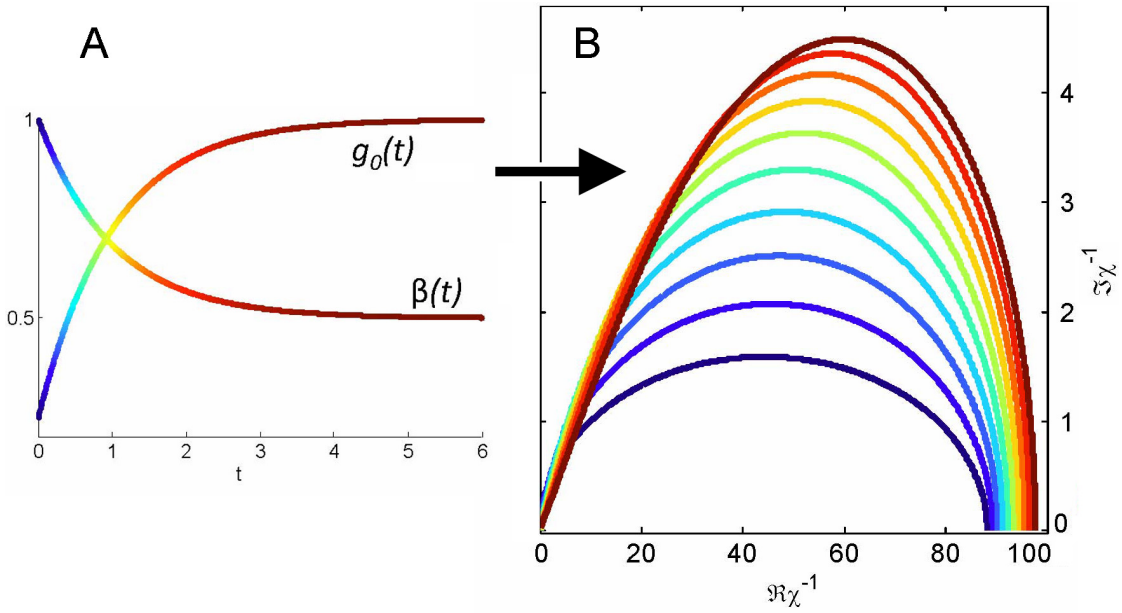

Figure 4.17: A phenomenological superglass model that produces qualitative agreement with observations of solid helium. **(A)** Time-dependence of the dissipative mode strength $g_0(t)$ and glassy distribution exponent $\beta(t)$, which extinguish a background superfluid stiffness to generate **(B)** a time-dependent Davidson-Cole susceptibility plot for a superglass. The color scale is the same for both **(A)** and **(B)** and is logarithmic in time (as in Fig. 4.11).

The model presented in Fig. 4.17 is merely meant to be illustrative; the difference between it and the model depicted in Fig. 4.12C is the presence of a superfluid component that dominates the real axis and whose phase stiffness is controlled by the glassy component. Nonetheless, this phenomenological model represents by far the most successful (in fact, to our knowledge so far the only) fit to the ultraslow relaxation dynamics (Fig. 4.11) that we reported in [66]. Of particular importance is that the fits are temperature-independent (because the

Davidson-Cole plot parametrizes out the temperature), thus constraining the physics maximally with the fewest free parameters possible. Though the fit is not perfect, it attains the following robust features:

- The large magnitude discrepancy (from a simple glass interpretation) is now resolved by a superfluid component that dominates the span of the real axis without accompanying dissipation.
- The mode distribution width increases in time, as reflected by the increasing skew (qualitatively similar to Fig. 4.11 although with the peak position shifting to higher temperatures, instead of lower, for unknown reasons.)
- The glassy mode exponent remains physical (i.e. it infers a physically plausible distribution of relaxation times.) In fact many classical glasses are described by a stretching exponent approaching $1/2$ [56, 1].
- The dissipation magnitude slowly increases as the specific energy capacity of the modes (described by g_0 saturates at long times.

Indeed, fitting a stretched-exponential to the time dependence of *skew* of the Davidson-Cole curves in Fig. 4.11 gives additional quantitative justification to this mode-spreading idea, although it requires a rescaling of the magnitude of f before fitting since the scale discrepancy otherwise disrupts the fits which follow. Furthermore, the fits are most easily accomplished with the data in polar form (Y is not an explicit function of X with a fit parameter). In a classical glassy susceptibility, the polar angle given by $\tan\phi = \frac{\Im\chi^{-1}}{\Re\chi^{-1}}$ for a given point on the Davidson-Cole plot is related to the magnitude r of that point - where $\left(\Im\chi^{-1}\right)^2 + \left(\Re\chi^{-1}\right)^2 = r^2$ by:

$$r = \Re\cos^{\beta}\left(\frac{\phi}{\beta}\right) \tag{4.12}$$

which gives characteristically skewed curves when $\beta < 1$. The fit parameter $\beta(t)$ is shown in Fig. 4.18, along with an inset showing the data from 4.11 in polar form and fit to Eq. 4.12 (after rescaling $\Im\chi^{-1}$ by δ_0 self-consistently within the superglass interpretation). Assuming such a rescaling is justified, the resulting $\beta(t)$ confirms the phenomenology of a single mode spreading out into many modes with increasing time.

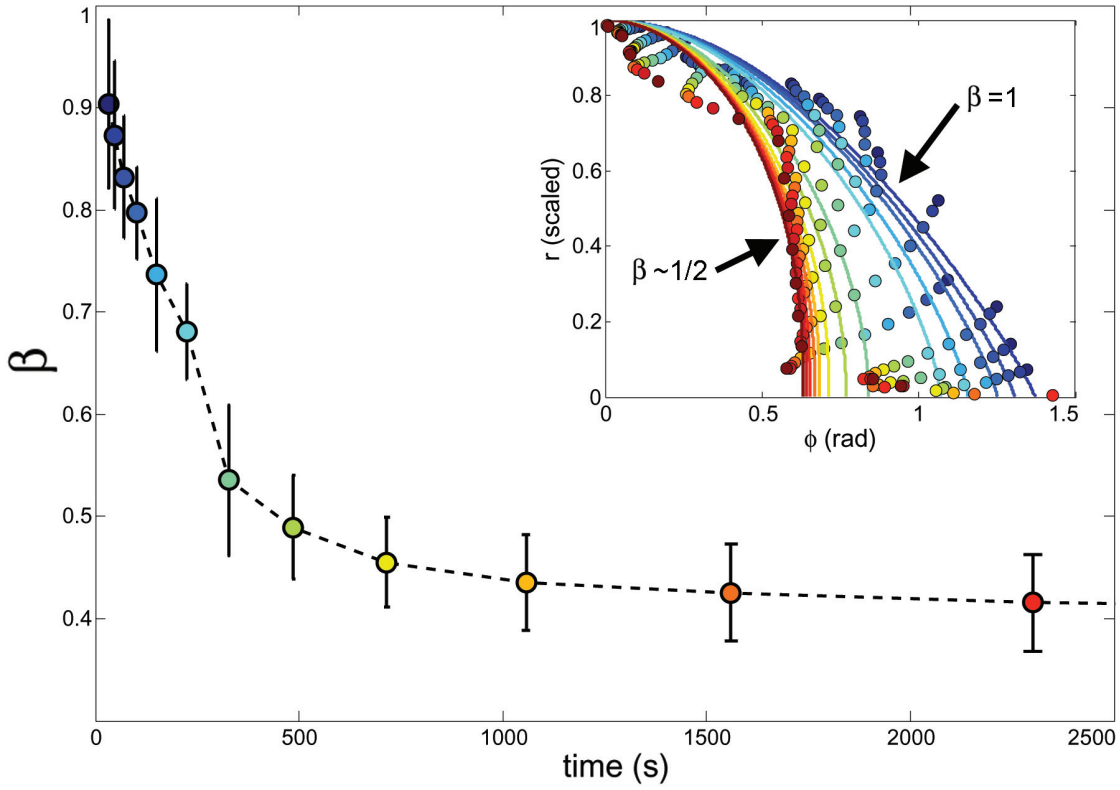

Figure 4.18: Time-dependent fitted stretching exponent $\beta(t)$ acquired from fitting the time-dependent DC plots in Fig. 4.11. Inset: Fitting curves and data shown in polar $r(\phi, t)$ form (after rescaling the magnitude discrepancy of f to allow a fit just to the skew). Within the superglass interpretation, the saturation of $\beta \rightarrow\sim 0.4$ at long times reflects the slowly widening distribution of glassy relaxation rates.

Finally, the superglass model avoids two pitfalls of exotic non-superfluid glass interpretations [36, 67], which attempt to completely resolve the magnitude discrepancy by employing broad distributions of relaxation times (i.e. ex-

tremely stretched exponential decays). The first is that a stretched exponential generates skew in a D-C plot because the dissipation peak occurs at a different temperature (or frequency) than the maximum slope of f - in other words, there is not just one T_* for the system. Yet in our data, the coincidence between these observations is extremely robust. Though there is room for fitting a slightly different T_*based on whether one looks at f or D, the discrepancy is not nearly as large as is required for stretched exponentials which deviate enough from unity to explain the magnitude discrepancy.

To see this more explicitly, Fig. 4.19 below shows several classical glass susceptibility curves with various stretching exponents, overlaid on the well-equilibrated data from Fig. 4.1. Note that as β departs more and more from 1, the dissipation peak occurs farther and farther from the maximum slope of f, whereas our data exhibits a quite close coincidence between the two (but a striking discrepancy in magnitude). This plot includes our best fit for a simple glass model to our well-equilibrated data, which seriously departs from fitting the transition shape in order to achieve agreement with the total magnitudes.

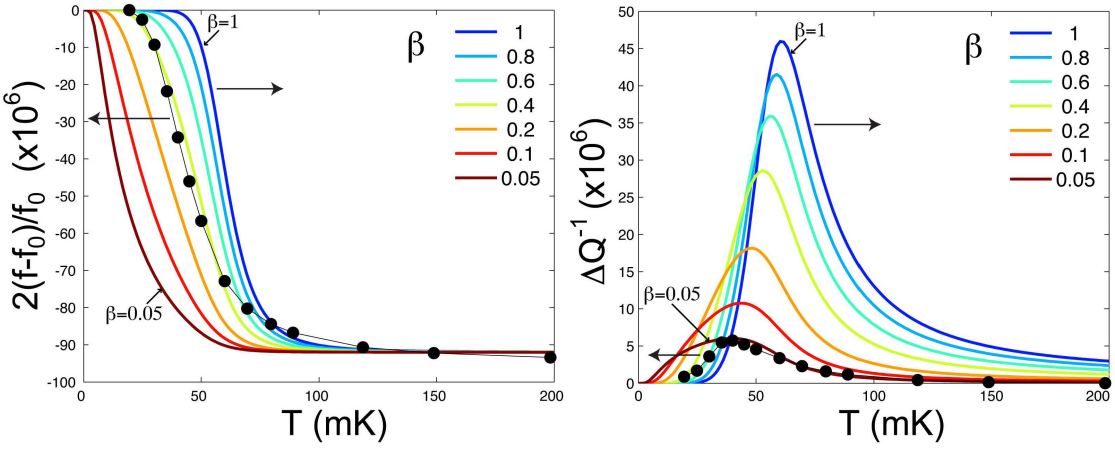

Figure 4.19: Fits to stretched-exponential glass susceptibilities (Eq. 4.7)

The second and much more serious pitfall avoided by the superglass model,

is that it is obvious from the time-dependent Davidson-Cole plot in Fig. 4.11 on page 50 that the skew is observed to increase in time. This fact - on its own - should require a stretching exponent to slowly *depart from* unity (as is certainly the case in this superglass model, see Figures 4.17 and 4.18). Simultaneously however, the magnitude discrepancy is observed to slowly decrease (it is most extreme at short times, when the D-C plot is most symmetric). This fact - on its own - should require a stretching exponent which slowly *approaches* unity. Clearly, a single exponent cannot simultaneously depart from - and also approach - unity. This stark conflict makes futile any attempt to fit the whole phenomenology of solid helium into a simple stretched-exponential glass interpretation.

4.7.2 Implications of a superglass

The principal open question motivated by these glassy observations is: what is the microscopic model that couples the dissipative and superfluid components? (Or, does a model exist which simultaneously fits these data - and the blocked annulus experiments - without invoking a superfluid?)

A superglass model could also generally explain the remaining diverse phenomenology of solid ^{4}He. As discussed above, the ω dependence of T_* [28] would occur because T_* is the temperature for which $\tau(T_*)\,\omega_0 = 1$. The shear modulus stiffening [10] would occur because of the freeze-out of liquid-like motion of these excitations, and T_* would increase with ^{3}He concentration [26, 31] because, with pinning, higher temperatures would be required to achieve the excitation rate $\tau(T_*)\,\omega_0 = 1$. Finally, sample preparation effects [27, 35] and dif-

ferent responses from different TO types would occur because the amorphousness allowing these excitations would depend on annealing and TO design.

Independent of these hypotheses, significant new elements of solid ^{4}He are revealed here. We find synchronized ultra-slow relaxation dynamics of dissipation $D(T)$ and a component of frequency shift of $f(T)$ in TO's containing amorphous solid ^{4}He (Fig. 4.7). Such phenomena are reminiscent of the glassy freeze-out of an ensemble of excitations and inconsistent with a simple superfluid transition. Nevertheless, while the evolutions of $f(T)$ and $D(T)$ are linked dynamically, the situation is also inconsistent with the simple excitation freezing transition because there is an anomalously large frequency shift (Fig. 4.11). One possible explanation is that solid ^{4}He is not a supersolid and that the appropriate rotational susceptibility model for its transition will be identified eventually. But if superfluidity is the correct interpretation of blocked annulus experiments [8, 49], then our results indicate that solid ^{4}He supports an exotic supersolid in which the glassy freeze-out at T_* of an unknown excitation within the amorphous solid controls the superfluid phase stiffness. Such a state could be designated a 'superglass'.

CHAPTER 5

UNIFIED SHEAR AGITATION DYNAMICS

The microscopic mechanism allowing shear agitation to inject energy into the dissipative dynamics of a driven material (such as a glass) leaves telltale signatures in its bulk material properties [1, 68]. Similarly, the microscopic connections between agitation (in the form of boundary velocity) and bulk transport are well known in superfluids, typically giving rise to characteristic bulk critical velocity effects that depend sensitively on the physics of the underlying excitation (e.g. vortex nucleation, phase slips, etc [69]). Which of these (if any) are the underlying microscopic mechanisms of low temperature solid ^{4}He remain unknown. However - when driven below both a characteristic velocity v_* and a characteristic temperature T_* - this exotic material does exhibit a well-known ultraslow inertial transition simultaneously consistent with both an agitated glass *and* a superfluid [66, 8, 27].

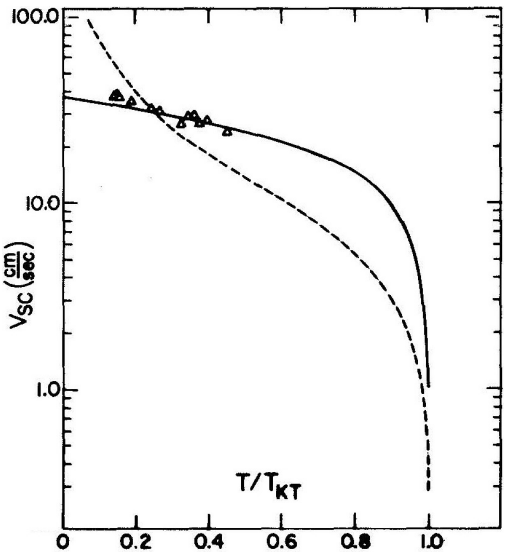

Figure 5.1: Critical velocity as a function of temperature (triangles) for a thin-film BKT transition, from [5]. The solid curve shows a theoretical fit to the KT recursion relations, including a velocity-dependent term.

Energy injected by increased mechanical agitation (parameterized in torsion oscillators by the rim velocity v) tends to reduce the characteristic temperature of as a function of this agitation, until at sufficiently high v the finite temperature inertial anomaly is completely extinguished. A measurable consequence of the glassy or superfluid nature of the excitations can therefore be revealed by observing the precise functional relationship between v_* and T_*. This relationship - essentially, the function $v_*(T)$ - should be exquisitely sensitive to underlying dissipative physics. For illustration of this type of observation, Fig. 5.1 shows the situation in a well-known dissipative superfluid system: the thin-film BKT vortex-unbinding transition, with two model curves capturing $v_*(T)_{KT}$ and observations overlaid, from [5]. The corresponding relationship between v_* and T_* in solid ^{4}He has not yet been observed .

5.1 Susceptibility as a function of velocity and temperature

Therefore we developed a new free-inertial-decay (FID) technique to map out the entire velocity-temperature "phase diagram" of solid ^{4}He in a torsion oscillator, and observed the effect of increased shear agitation and its consequential decrease in the thermal activation necessary to disrupt the supersolid inertial transition. These effects are interrelated and captured by the characteristic ("critical") contours that extinguish the inertial transition, and are only visible with the whole $v - T$ susceptibility revealed.

Acquiring the complete susceptibility map is a formidable experimental challenge, because the fragile nature of the solid helium dynamics requires a high duty cycle to collect sufficient data without disruptive helium transfers inter-

vening. We used the extremely high dynamic range and S/N ratio of a DC-SQUID displacement sensor on the same annular torsion oscillator as previously discussed (see Fig. 2.1) to efficiently capture the necessary data as quickly as possible.

A drive torque is applied on resonance near 575 Hz via a capacitor electrode in a standard phase-locked-loop circuit (Fig. 2.7), while the resulting oscillations can be detected either by a second capacitor electrode (which is used at high velocities) or via the high-sensitivity DC-SQUID detector (used at low velocities). The dual detectors allow us to measure the torsion response over a dynamic range spanning more than six orders of magnitude. A typical FID - taken at 47 mK - is illustrated in Fig. 5.2.

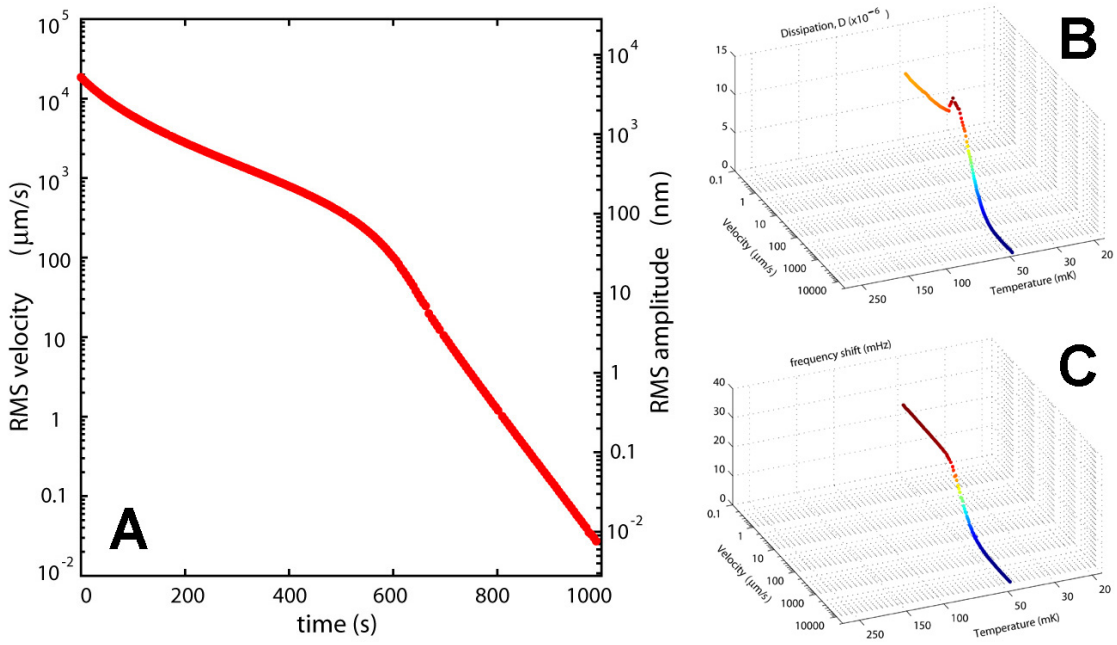

Figure 5.2: **(A)** Oscillator amplitude during a typical free-inertial-decay ringdown on resonance at 47 mK. The velocity-dependent dissipation $Q^{-1}\,(\mathrm{v},\,47\,\mathrm{mK})$ is acquired in software by fitting this decay envelope to an exponential within a sliding window of 28 seconds duration. The background is then subtracted to reveal the velocity-dependent helium dissipation for this temperature, shown in **(B)**. The resonant frequency $f\,(\mathrm{v},\,47\,\mathrm{mK})$ is measured simultaneously (see Fig. 2.7) and shown in **(C)**.

Ringdowns such as this are acquired by stabilizing the temperature, driving the oscillator to high amplitude, and then suddenly turning off the drive torque. The amplitude and frequency are recorded during the subsequent free decay. At fixed temperature, the recorded oscillator frequency contains the real part of the ^{4}He dynamical susceptibility (as a function of velocity), while the slope of the ringdown envelope (as shown in 5.2A) contains the dissipative part. By judicious choice of temperatures, we have mapped the complex susceptibility over the complete range of temperatures and velocities of interest, and display this complete set of FID's in Fig. 5.3.

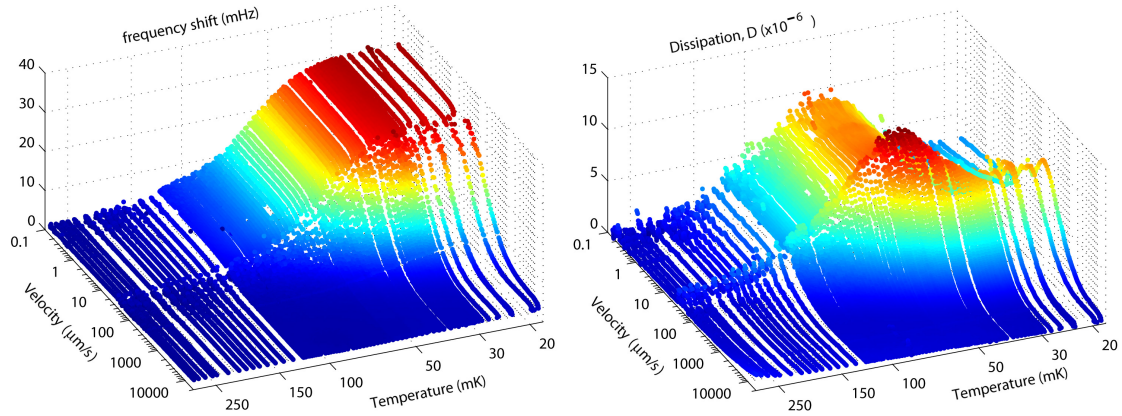

Figure 5.3: Complete set of frequency shift (left) and dissipation (right) observations from free-inertial-decay experiments on low-temperature solid ^{4}He. Color scale indicates magnitude for each respective plot.

The low-velocity maximum frequency shift (~30 mHz) in our sample would correspond to a superfluid fraction of roughly 5% if it was entirely ascribable to a simple supersolid phase transition. Within Fig. 5.3 we discovered a previously unknown "superpeak" region of enhanced dissipation centered at roughly (50 mK, 30 microns/s). In fact, a velocity-dependent signature similar to this was observed in the thin-film BKT transition [3], although it was not discussed therein and the complete $v - T$ surface was not acquired, so further comparison is difficult. Nonetheless, several line-cuts across the the dissipation surface for that

transition were observed and are shown in Fig. 5.4 for qualitative comparison to solid helium.

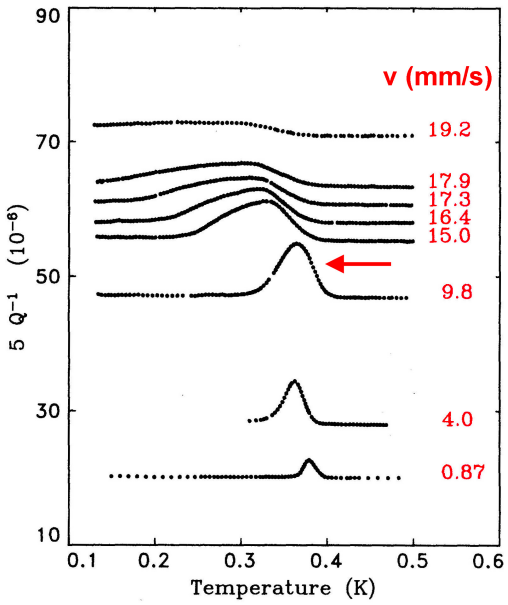

Figure 5.4: Some line-cuts across the $D(v,T)$ dissipative susceptibility surface of a thin-film BKT vortex-unbinding transition (adapted from [3]) for comparison to Fig. 5.5B. We have noted the appearance of a superpeak by adding an arrow.

To extract a quantitative signature of the dissipative physics generating the susceptibilities in Fig. 5.3, it is useful to interpolate the discrete data and reveal the underlying smoothly contoured surfaces. These are then displayed as the two color-coded contour plots on log-log axes spanning several decades of temperature and velocity in Fig. 5.5.

5.2 Observation of velocity imitating temperature

We can now revisit the Kim and Chan effect using this measurement: it is acquired by a temperature-dependent line-cut across the $f(v,T)$ and $D(v,T)$ surfaces at low velocity, as shown in Fig. 5.6 (a) and (c).

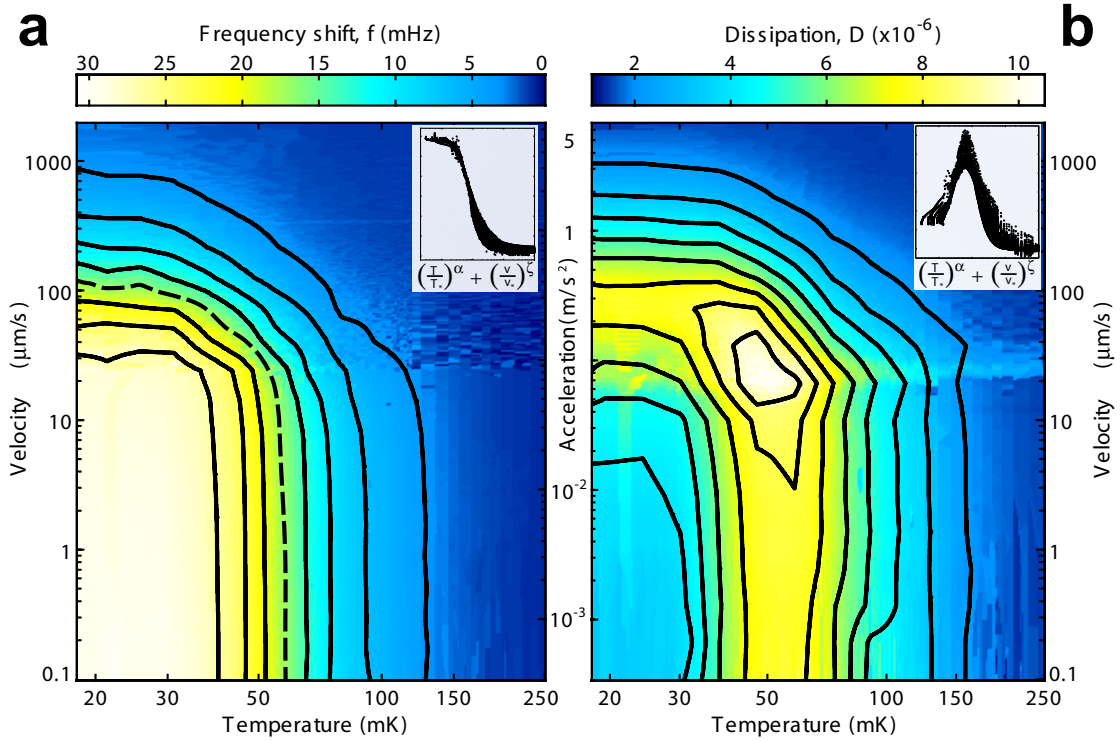

Figure 5.5: Interpolating the f and D surfaces in Fig. 5.3 gives the complete map of complex susceptibility as a function of velocity and temperature - a type of "phase diagram" for solid ^{4}He. The frequency shift is shown in **(a)** and the dissipation in **(b)**. Note the observation of a "superpeak" - a previously unknown region of enhanced dissipation encircled by close contours. The characteristic contour of the real susceptibility is dashed, and insets show collapse of the data onto a unified axis as discussed in the text.

Remarkably, however, we observe that it is alternatively possible to observe an essentially indistinguishable inertial anomaly if we take a velocity-dependent line-cut across the f and D susceptibility surfaces at low temperature - shown in Fig. 5.6 (b) and (d) - but only with the special modification that the velocity axis be redefined by $v \rightarrow \sqrt{v}$.

Therefore we observe that velocity scaled in this way - at least on the extreme linecuts of the susceptibility surfaces of Fig. 5.5 - effectively imitates a temperature. Furthermore, note that the internal relaxation time associated with a rather simple overdamped dissipative transition (see Sec. 3.2) can be directly acquired

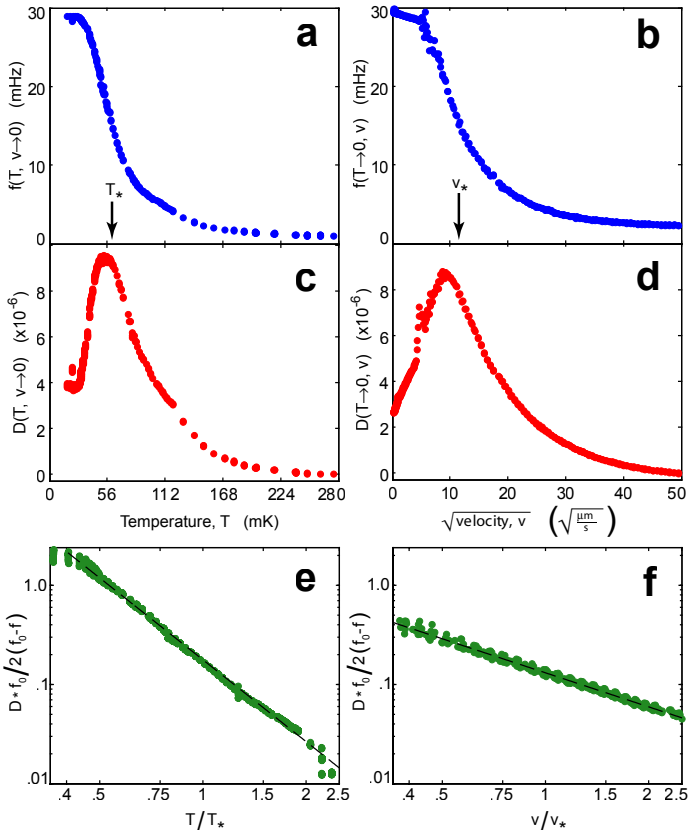

Figure 5.6: Line-cuts across the susceptibility phase diagram in Fig. 5.5 at low *velocity* (below 5 microns/s) reveal the usual Kim/Chan inertial anomaly as a frequency shift **(a)** and dissipation peak **(b)** - see also Fig. 4.1. On the other hand, we discovered that a line-cut across the same surface at low *temperature* **(c)** and **(d)** reveals essentially identical behavior if the susceptibility is plotted on a $\sqrt{v}$ axis. The putative relaxation time of an overdamped mode controlling such an inertial anomaly can be observed directly by a plot of $\frac{D}{2(f_0-f)}$ using data from **(a)-(d)**. We find that this relaxation time is given by power laws alternatively at low velocity **(e)** or low temperature **(f)**. The solid curves are power laws with exponents of 2.74 and 1.13, the ratio of which is slightly higher (by about 20%) than that used in the plots of T^1 vs. $v^{1/2}$.

by the observation of $\frac{D}{2(f_0-f)}$. This quantity, generated at low velocity (by the data in Figs. 5.6 a and c) is displayed as Fig. 5.6e, while the analogous quantity is generated at low temperature (by the data in Figs. 5.6 b and d) and displayed as Fig. 5.6f. Log-log axes are chosen to illustrate that the internal dissipative rate indeed obeys power law speedup with increasing agitation, as opposed to sim-

ple Arrhenius activation. This comparison is shown more explicitly in Fig. B.2. The observed quantity $\frac{Df_0}{2(f_0-f)}$ is shown on log-log-log axes in Fig. 5.7, where the power laws can be seen directly as regions of equally-spaced contour lines.

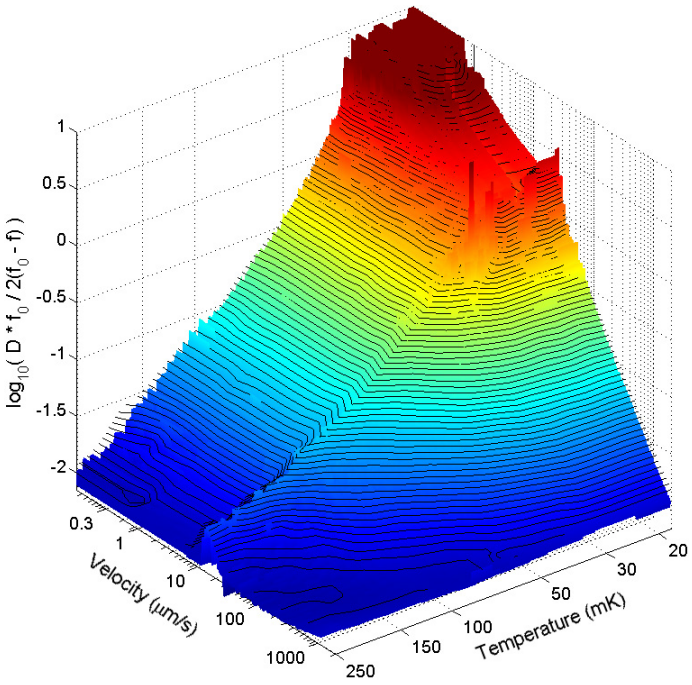

Figure 5.7: Log-log-log plot of the observed quantity $\frac{Df_0}{2(f_0-f)}$ which is proportional to the internal dissipative relaxation time of the material. Power law behavior generates regions of equally-spaced contour lines on this surface, which are easy to see by eye (also, the extrema power laws of T at low-v, and v at low-T are obvious). The superpeak region is visible, but is not as prominent as on the linear-scale surface plot of D in Fig. 5.5.

In fact, as can be seen by the fit quality of Fig. 5.6 (e) and (f), the integer powers which we selected for simplicity (namely, T^1 vs. $v^{1/2}$) are not quite the best fits. Instead, the best fits are given by $T^{2.7\pm0.1}$ vs. $v^{1.1\pm0.1}$ and therefore we see that the ratio of the fitted powers (which controls the apparent fit quality of the plots in Fig. 5.6) is ~2.4, or 20% higher than the integers. Nonetheless, for pedagogical simplicity we will use the integer powers where useful.

The observation of a power-law function of velocity acting indistinguish-

ably from a power-law function of temperature is completely unexpected in the context of either classic superfluid systems, or simple Arrhenius-activated freeze-out materials. Nonetheless, the observation of this behavior in solid ^{4}He provides a robust signature of the internal dynamics, against which to compare various theoretical predictions of the dashed connecting contour between v_* and T_* in Figure 5.5, since the functional form of that curve will depend sensitively on the mechanism by which temperature-dependent and velocity-dependent excitations combine when both are independently excited.

5.3 Effective temperatures

The identification of shear agitation as a parameter that mimics temperature is a concept much more familiar from the observations and modeling of jammed disordered nonlinear systems [6, 70]. In such materials, it is now well-known that drive parameters such as shear stress can often be expressed as effective temperatures, even in the absence of actual thermodynamic agitation. For this equivalence to hold, it appears to be critical that the dissipative excitations undergo a jamming transition - that is, enter a disordered state with a yield stress. The physical mechanism of agitation as an effective temperature is then:

1. shear agitation decorrelates the strain fields within the sample in a statistically indistinguishable way from a thermal bath
2. the time-dependent configuration of the excitations explores the available parameter space in an approach to ergodicity

An unjammed or ordered system will not sustain one or both of these conditions. An illustrative observation of shear rate as an effective temperature for a driven disordered foam, from [6], is shown in Fig. 5.8.

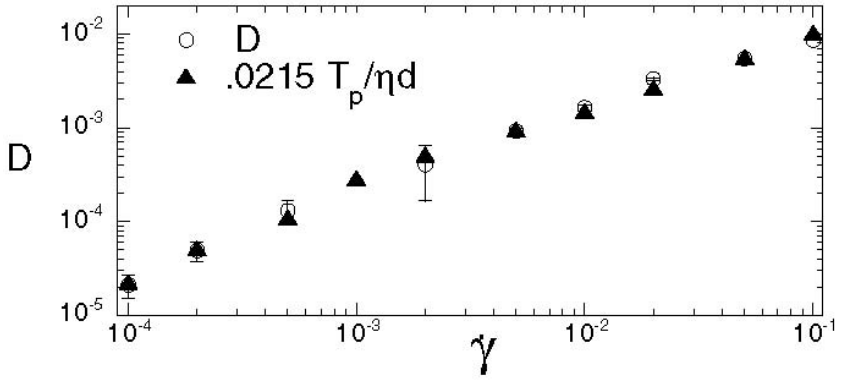

Figure 5.8: Effective temperature for a driven system near jamming, from [6]. The diffusion constant D - which is given by temperature (via the fluctuation-dissipation theorem) for a typical thermodynamic system - is found here to be a power law of shear rate $\dot{\gamma}$ for a jammed athermal system. The jammed system enters an "effective temperature" state because shear agitation decreases the strain autocorrelation time and forces the athermal system to explore configuration space approaching ergodicity: effects of agitation that are statistically indistinguishable from a thermodynamic temperature.

To generate a phenomenological model wherein such coupling is given by a fitted observation to the data, we note that an overdamped Debye susceptibility is a quite useful phenomenological description of the shape of the inertial transition, apart from an overall magnitude discrepancy (see Sec. 4.7.1). Thus we are motivated to look for a type of sum of agitations which can enter the Debye susceptibility to allow curve-fitting. (Also, see Sec. B.2 for a discussion of high-velocity susceptibility in light of linear response.)

Specifically, the simple ansatz we use is based on an assumption that temperature and velocity each generate excitations which combine in some way to give a total relaxation time τ as follows, where n is a yet- undetermined fit parameter

governing the phenomenology of how the excitations combine:

$$\omega\tau = \omega_0 \left[\left(\frac{T}{T_*} \right)^{\alpha} + \left(\frac{v}{v_*} \right)^{\lambda} \right]^{-n} \tag{5.1}$$

where v_* and T_*can be measured as illustrated in Fig. 5.6 and $\omega\tau$ is assumed to enter the velocity-dependent version of the susceptibility of Eq. 3.18. Obviously, we switched to the notation which allows the exponents to float from the pedagogical integer values. In fact, to remain consistent with the power laws on the extrema linecuts as fitted in Fig. 5.6, we know the following conditions must be satisfied:

$$\alpha n = -2.7, \quad \lambda n = -1.1 \tag{5.2}$$

though n remains undetermined. Several intuitive choices for n are possible: a quadrature sum of fluctuation times is recovered by the choice $n = 1/2$, while the physics of an incoherent simple sum of excitation rates is recovered by the choice $n = 1$.

5.4 Other models for the critical contour

A network of dislocation lines with superfluid cores was originally proposed several decades ago as a possible microscopic structure for a solid exhibiting an inertial anomaly [71, 72], and is known as the Shevchenko state; this model was recently updated by Shevchenko and a collaborator [73] to include a useful relationship between an internal hopping amplitude t and the transition temperature T_{BEC}, as will be discussed.

5.4.1 The Shevchenko state

The Shevchenko model treats vacancies on an interlaced cubic lattice of dislocation lines, as shown in Fig. 5.9 (adapted from [73]); each line contains several sites for vacancies in-between adjacent network crossing nodes; these adjacent sites are separated by the small distance a. The network nodes (i.e., junctions between lines) occur with a period of length l. The key control parameter is the hopping amplitude t which gives the probability for a vacancy to tunnel from one site to the next along the line (hopping a distance a in the process). There is also a parameter t_1 which governs hopping onto a network crossing node site, which is treated in [73] but ignored here because it doesn't enter T_{BEC} in the most applicable case. The 1-dimensional vacancy density n_1 is proportional to the filling factor (i.e., vacancies per site), and is notable because n_1 enters T_{BEC}.

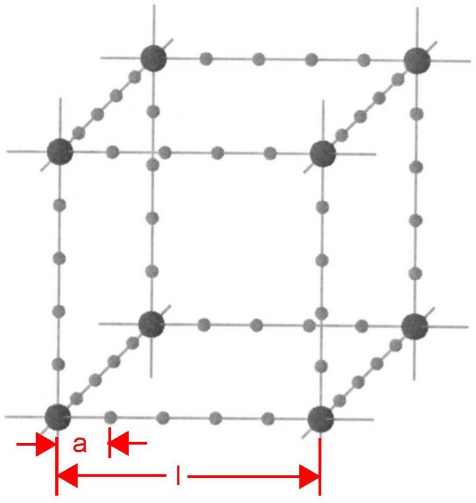

Figure 5.9: Elementary cell of a lattice model of dislocation lines with node crossing period l and vacancy hopping site period a. Vacancies tunnel between adjacent sites with amplitude t.

Essentially, the rest of the recent Fil and Shevchenko paper is devoted to calculating band structure and T_{BEC} for several cases of the filling factor and ratio of t to t_1. More importantly for the present analysis, their results for all

the considered cases give a linear dependence $T_{BEC} \propto t$, while the other parameters only affect the coefficients. Furthermore, this model has a degeneracy temperature T_D that is higher than T_{BEC}, and below which one should observe superfluid-like hydrodynamics with ultra-slow relaxations as the degeneracy lifts, but which does not give a true condensate. The main prediction of [73] is now reprinted as Eq. 5.3 for reference,

$$T_{BEC} \approx 3ta^2 \frac{n_1}{l} = \frac{3}{2} \frac{\hbar}{M^*} \frac{n_1}{l} \tag{5.3}$$

where the alternate form on the right treats t as an inverse effective mass M^*. Also, their specific prediction for the degeneracy temperature is $T_D = t\,(n_1 a)^2 \gg T_{BEC}$. Nonetheless, note that both T_{BEC} and T_D are linear in t, so the rest of this treatment remains relevant (with respect to scaling) regardless of which temperature is presumed to control the inertia.

Given the functional form of Eq. 5.3, we need a functional form of t dependence on v to extract the interplay between temperature and velocity for this dislocation lattice model; that is, how does the external shear velocity inhibit the tunneling amplitude? One such dependence is used in Andreev's TLS paper [37], specifically in giving the effective tunneling barrier $\triangle = t\sqrt{1+u^2}$ (where u is a dimensionless version of v, $u \equiv \dfrac{v}{v_\star(0)}$ and we are otherwise using Shevchenko's notation). Assuming this is sensible, the dependence assumed for the rest of this section is simply given by a dimensionally consistent inversion of the form used by Andreev:

$$t \propto \left(1+u^2\right)^{-1/2} \tag{5.4}$$

which can be inserted into Eq. 5.3 and inverted to find the scaling dependence between $u_\star$ and T below $T_\star$, where $T_\star$ could be either T_{BEC} or T_D, and the re-

duced characteristic velocity $u_\star(T) = \dfrac{v_\star(T)}{v_\star(0)}$ is the interesting scaling quantity:

$$u_\star \propto \sqrt{\left(\frac{T_\star}{T}\right)^2 - 1} \tag{5.5}$$

This result will be compared directly to the functional form of our measured contour $v_\star(T)$ on the real susceptibility surface. Also note that this functional form is quite different than that due to an incoherent sum of relaxation rates, which is given by:

$$u_\star = \frac{v_\star}{146\,\mathrm{um/s}} = \left[1 - \left(\frac{T}{63\,\mathrm{mK}}\right)^\alpha\right]^{-1} \tag{5.6}$$

where α is a positive fitting parameter.

5.4.2 Two-level systems

In addition, the agitation physics of a single TLS mass deficit [61] can be put into the following form:

$$u_\star = \sqrt{\tanh^2\left(\frac{T_\star}{T}\right) - B} \tag{5.7}$$

where B is a fitting parameter, and both $u_\star$ and $T_\star$ are different fitting parameters for this model than simply the low-v and low-T values.

Also, it seems worthwhile to point out that these models do not necessarily predict or agree particularly well with the temperature-dependent inertial anomaly observed in solid helium, as seen in Fig. 4.13 on page 55. However, we will examine here only their predictions of the functional form of the critical interplay between velocity and temperature, which we presume may point towards some independent physical insights that might be included in a more complete model.

5.5 Nearly complete data collapse

We are now prepared to analyze the observed critical contour $v_*(T)$ - which we take to be that contour which extinguishes 50% of the frequency shift, along with the theoretical functional forms. This data is shown in Fig. 5.10, along with the BKT curve from [5] (Fig. 5.1) for illustration, and curves generated by equations 5.5, 5.6, and 5.7. Note that the corresponding putative contour on the dissipation axis is more difficult to extract because of the unexplained superpeak.

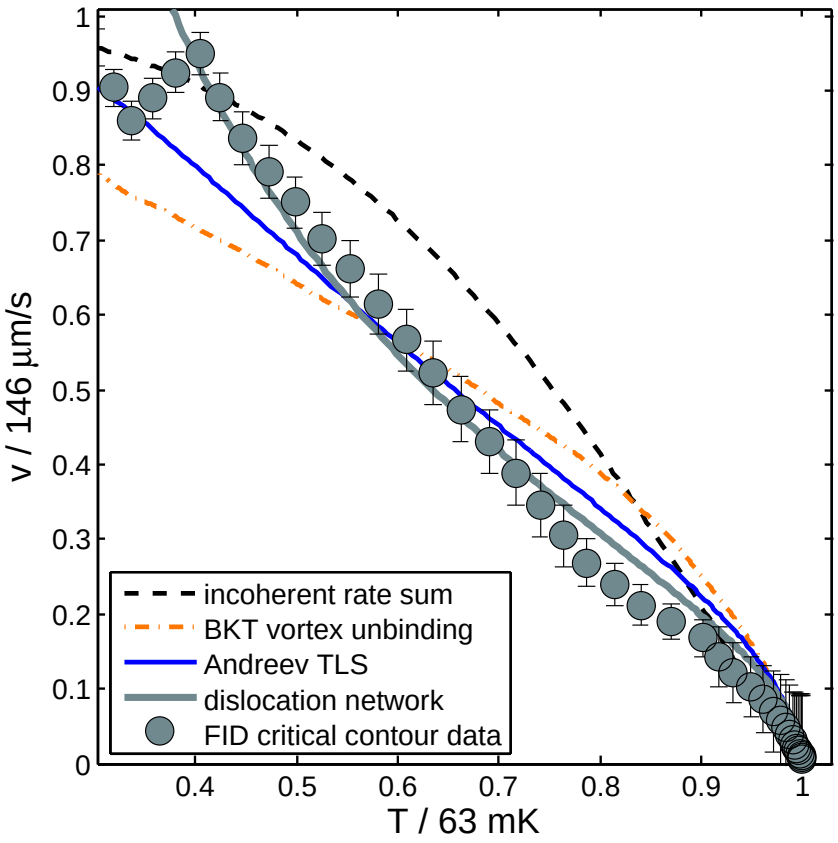

Figure 5.10: Critical contour $v_*(T)$ for the real susceptibility of solid ^{4}He (gray dots), extracted from Fig. 5.5 as the contour that extinguishes 50% of the frequency shift. At low velocity, this contour gives $T_* = 63.2 \pm 0.8$ mK and at low temperature, it gives $v_* = 146 \pm 3$ um/s. This curve is expected to be strongly influenced by the microscopic mechanism allowing velocity or shear agitation to influence the inertia. The curves correspond to functions in the text.

Several features of these models can be plausibly fit to the observed data, with the dislocation network giving the best agreement over the largest range, but failing under our assumed $t\,(v)$ dependence failing to give the proper low-temperature asymptote. Also, note that the Andreev model, which gives a rather decent fit to this contour, fails to fit the low-velocity inertial transition very well at all (as in Fig. 4.13 on page 55).

However, at least approximately, it appears that a great deal of the physics underlying the dissipative inertial transition in solid ^{4}He is similar to that of an incoherent sum of relaxation rates due independently to shear agitation (i.e. velocity) or temperature, and that these rates increase as power laws of their respective arguments. A natural consequence of identifying the critical contour in Fig. 5.10 with a suitable analytical form for $\omega\tau$, is that the data should *collapse* onto the unified agitation rate axis as given by 5.1 (or its approximate equivalent expressed with integer powers, $\omega_0^2\left(\Phi^{-1}T^2+\xi^{-1}\mathrm{v}\right)^{-2}$ where the coefficients Φ and ξ are trivially related to the measured v_* and T_*). An attempt at this collapse (excluding the superpeak) is shown in Fig. 5.11, along with some susceptibility curves as discussed. Theories corresponding to the other theoretical contours shown in Fig. 5.10 would presumably give equally good collapse, but only the Debye susceptibility gives a full prediction for the entire surface, as opposed to just the critical contour. Therefore it will be used to illustrate the collapse.

The solid curve in **5.11(B)** is a fit to a Debye model (see Eqs. 4.4, 4.5 and Ref. [36]) of such a relaxation time $\omega\tau$ where the relaxation rate is a power law of excitation; it correspondingly gives the dashed curve prediction for $f\,(v,T)$ shown in **5.11(A)**. The discrepancy in magnitude that was observed for the superglass sample is similarly observed here, and identical when viewed as a function of

velocity or temperature. The discrepancy can be overcome by several modifications, including an overall boost to the real susceptibility, which corresponds to a simple model of a superglass and is shown as the solid curve in **5.11(A)**. A distribution of relaxation times can also somewhat reduce the discrepancy, but typically, we find that distributions broad enough to eliminate the magnitude discrepancy necessarily skew the dissipation peak far away from the inflection point of the frequency shift. The fit quality to these or any model curves is an issue concerning the specific *shape* of the data, and is an open issue.

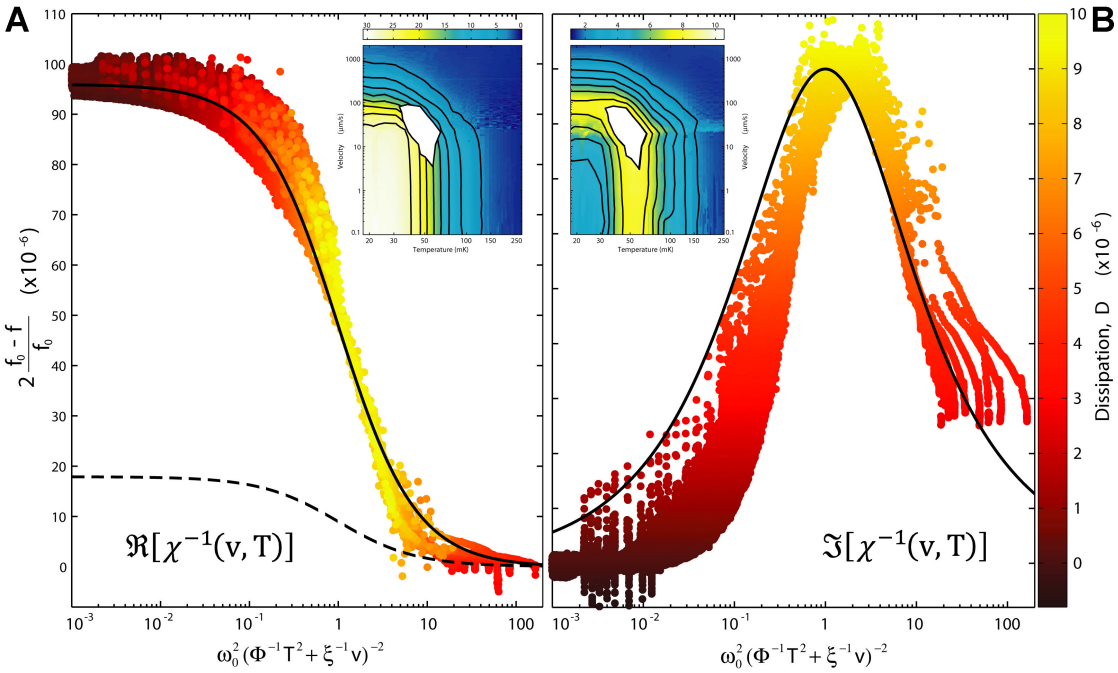

Figure 5.11: The complete collapse (excluding the superpeak) of the real **(A)** and dissipative **(B)** susceptibility surfaces of Fig. 5.5 (shown as insets) onto a unified agitation axis $(\omega\tau)^2$ given by an incoherent sum of power-law relaxation rates due to temperature or velocity, $\omega_0^2\left(\Phi^{-1}T^2+\xi^{-1}v\right)^{-2}$.

Nonetheless it remains an observed fact - even in the absence of any model curves - that the data do *collapse* onto the unified agitation axis. These observations are most consistent with a picture of jammed, disordered excitations that are already known to display glassy behavior [66], and which dynamically

control the onset of the supersolid inertial anomaly.

5.6 Power law behavior from glassy distributions

Given the superior fit quality of the Debye susceptibility (Fig. 4.13 on page 55), observation of ultra-slow relaxations with increasing skew (Fig. 4.11 on page 50) indistinguishability of velocity from temperature (Fig. 5.6), and the persistent extreme magnitude ratio between the saturated dissipation peak and real frequency shift (Table 4.1 on page 60), the emerging physical picture is that of a driven superglass, where ultra-slow evolution of a mechanical ensemble controls a superfluid that is principally responsible for the large inertial transition.

However, the power law phenomenology discussed in section 5.2 reveals a glaringly unexplained component of this physical picture. It is of course possible to hypothesize - as we have done in Eq. 5.1 - that the internal relaxation rate is simply a direct power law of temperature (or velocity). But this relation does not have a strong physical motivation. Instead, what we would now like to examine, is whether one consequence of the glassy hypothesis - namely that there exists a probability distribution function describing the *spread* of internally relaxing mechanical modes - can also explain the unexpected emergence of power law relaxation behavior.

Specifically, we would like to establish in principle whether the cumulative effects of a distribution of Arrhenius-activated microscopic processes (which has a robust physical motivation, unlike the phenomenology of Eq. 5.1) might generate an apparent power law susceptibility. Consider the well-known formulation of a susceptibility made up of the cumulative effect of such a distribu-

tion of microscopic Debye relaxations [74]:

$$\chi^{-1}(\omega, T) = \int_{-\infty}^{\infty} \frac{1}{1 - i\omega\tau} \widetilde{G}(\tau) d \ln \tau \tag{5.8}$$

where the temperature dependence comes from $\tau = \tau(T)$. Typically, distributions are defined on a log basis for compactness, but we would like to define the distribution on a linear basis for clarity [75]. Since $d \ln \tau = d\tau/\tau$, we redefine $G(\tau) \equiv \widetilde{G}(\tau)/\tau$, so that

$$\chi^{-1}(\omega, T) = \int_{0}^{\infty} \frac{1}{1 - i\omega\tau} G(\tau) d\tau \tag{5.9}$$

Eq. 5.9 can reproduce some commonly used susceptibilities by judicious choice of $G(\tau)$. Motivated by the suitable time-dependent behavior of the Davidson-Cole distribution (allowing for an overall magnitude discrepancy) in Fig. 4.18 on page 65, we choose to proceed with this model for specificity. Other distribution functions could probably also be chosen, however, the goal is to find the *existence* of any function that provides a more convincing explanation of the power law relaxation than an Arrhenius-activated Debye susceptibility, not necessarily to prove its uniqueness or maximal effectiveness. The Davidson-Cole glass will be seen to satisfy at least this modest goal. These two distributions are now listed in Table 5.1.

Table 5.1: Some distribution functions for conformational ensembles and their corresponding susceptibilities at low velocity.

Model →	Single mode	Davidson-Cole glass
Insusceptibility $\frac{1}{g_0}\chi^{-1}(\omega, T)$	$\frac{1}{1-i\omega\tau(T)}$	$\left(\frac{1}{1-i\omega\tau(T)}\right)^{\beta}$
Distribution function $G(\tau)$	$\delta(\tau' - \tau)$	$\begin{cases} \frac{\sin \pi\beta}{\beta} \left(\frac{\tau}{\tau_c - \tau}\right)^{\beta}, & \tau < \tau_c \\ 0, & \tau > \tau_c \end{cases}$

Now, we would like to recast the distribution of τ (i.e. $G(\tau)$) as a distribution $P(\Delta)$ over energy barriers Δ within an Arrhenius model for the relaxation time. This can be accomplished with a simple change of variables in Eq. 5.9. Let $\tau = \tau_0 \exp(\Delta/T)$. The inverse is $\Delta = T \ln(\tau/\tau_0)$, so to change the limits of integration, $d\tau = (\tau_0/T)\exp(\Delta/T)d\Delta$.

Thus we rewrite Eq. 5.9 as

$$\chi(\omega, T) = \int_{-\infty}^{\infty} \frac{1}{1 - i\omega\tau_0 \exp(\Delta/T)} P(\Delta, T) d\Delta \tag{5.10}$$

where the two distributions are related by

$$\begin{gathered} P(\Delta, T) = (\tau_0/T) G(\tau) \\ \tau = \tau(T) = \tau_0 \exp(\Delta/T) \end{gathered} \tag{5.11}$$

which retains the physically motivated microscopic Arrhenius-activated physics.

5.6.1 An excitation-dependent distribution function

The preceding section leads us to use the following adapted Davidson-Cole probability distribution function, where $A(T)$ is a normalization coefficient such that the total probability at each temperature is unity:

$$P(\Delta, T) = A(T) \frac{\sin(\pi\beta)}{\beta} \left(\frac{\tau}{\tau_c - \tau} \right)^{\beta} \tag{5.12}$$

This is easily derived from the Davidson-Cole distribution $G(\tau)$ in Table 5.1 and Eq. 5.11 [74]. Often, in classical glasses the D-C distribution is considered *temperature-independent* and the susceptibility is probed by varying the frequency; here we investigate the temperature dependence of the distribution

itself, as well as the temperature-dependent rate of activation over the amorphous ensemble of conformational defects comprising it.

Given a particular β and a temperature, one can calculate the probability distribution over the possible energy barriers Δ. Since the FID data is acquired after suitable mechanical equilibration of the ultra-slow dynamics, we choose a stretching exponent $\beta = \frac{1}{2}$ to roughly correspond to the $t \to \infty$ limit and thus reduce the scope of distribution functions we will consider (see Fig. 4.18 on page 65). A series of such distributions for various T is shown in Fig. 5.12.

Already, we observe that this type of distribution should generate some of the qualitative features we observed in solid helium:

- As temperature increases from $T \to 0$, glassy equilibration of the conformational barriers governed by this probability distribution would generate ultra-slow relaxation dynamics (as in Fig. 4.4 on page 39) while the distribution relaxes.
- The susceptibility immediately after heating would be dominated by the simple back-action of a superheated single mode and would generate an elliptical Davidson-Cole plot. This is consistent with the blue, $t \to 0$ curve in Fig. 4.11 on page 50 apart from the real magnitude.
- Later, the distribution function would slowly approach the equilibrium multi-mode distribution given by T, which corresponds in solid helium to the skewed, glassy behavior (red $t \to \infty$) Davidson-Cole response in Fig. 4.11 on page 50.

Using equations 5.10, 5.11, and 5.12 as illustrated by Fig. 5.12, we are now prepared to evaluate the susceptibility and relaxation rate of the Davidson-Cole

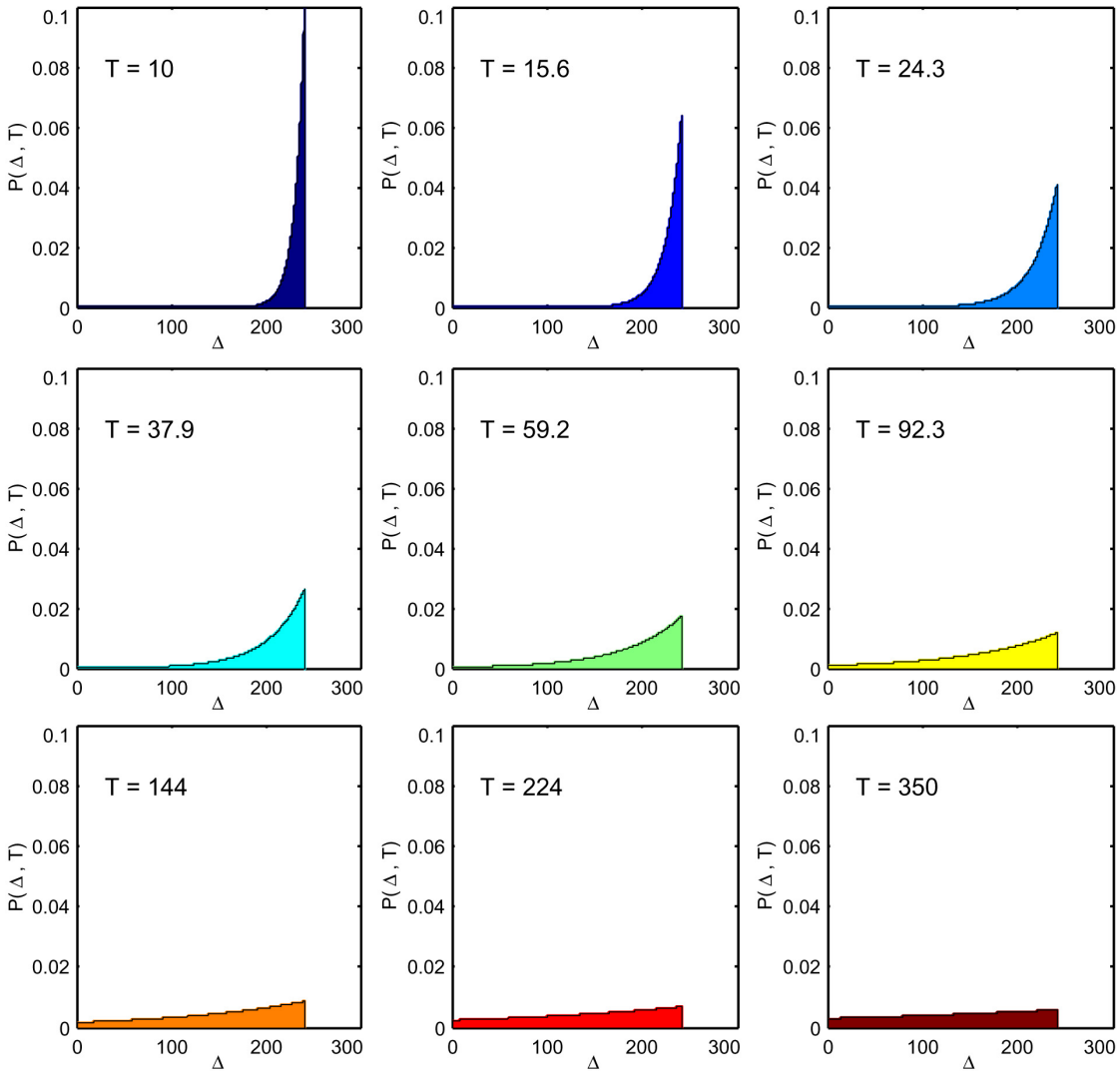

Figure 5.12: Adapted D-C normalized probability distribution function $P(\Delta, T)$ of Arrhenius-activated energy barriers Δ at various temperatures T (with $\beta = \frac{1}{2}$ for illustration). The cutoff relaxation time τ_c in Eq. 5.12 corresponds in this formulation to a cutoff Δ_C, above which there are no barriers. The low-temperature distribution function approaches the delta-function Debye susceptibility.

glass, and compare it to the Debye single-mode material and for illustration, our solid helium data. Such a comparison is presented in Fig. 5.13.

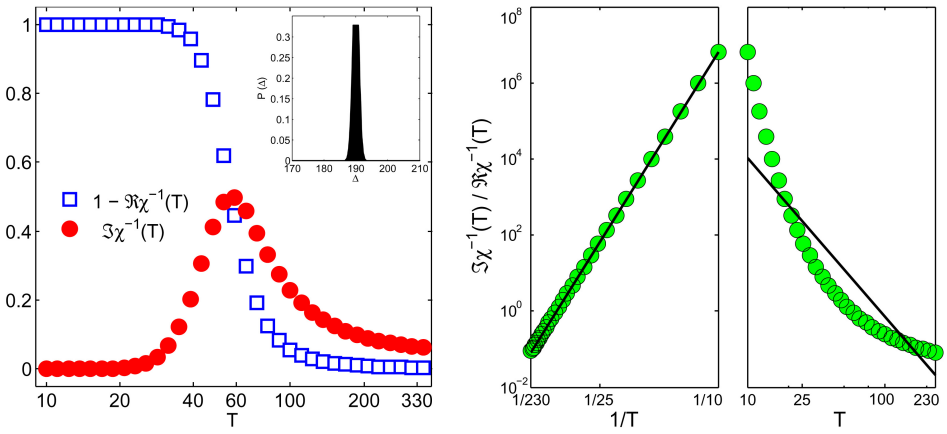

(a) Left: theoretical susceptibility of a T-independent single overdamped mode (approximated delta-function $P(\Delta)$ inset) and corresponding relaxation time τ (right). Simple Arrhenius activation generates a straight line on log τ *vs* $\frac{1}{T}$ axes.

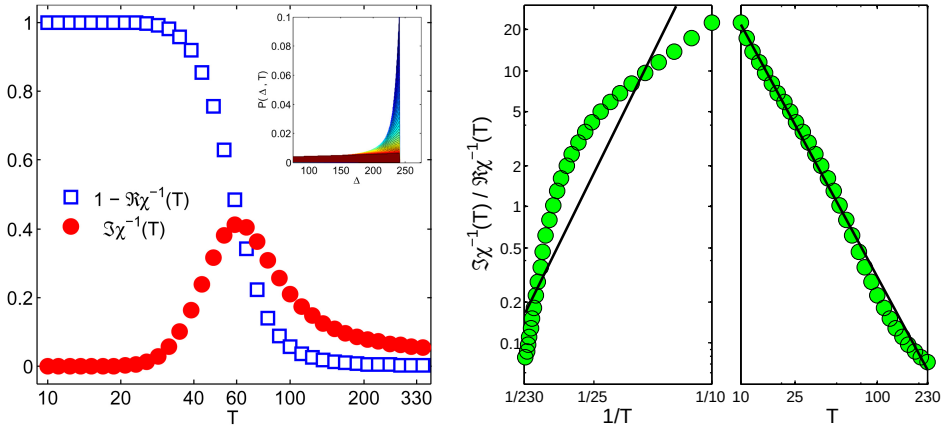

(b) Left: theoretical susceptibility of a T-dependent glassy mode distribution and τ (right). Power law relaxation gives a straight line on log τ *vs* log$T$ axes.

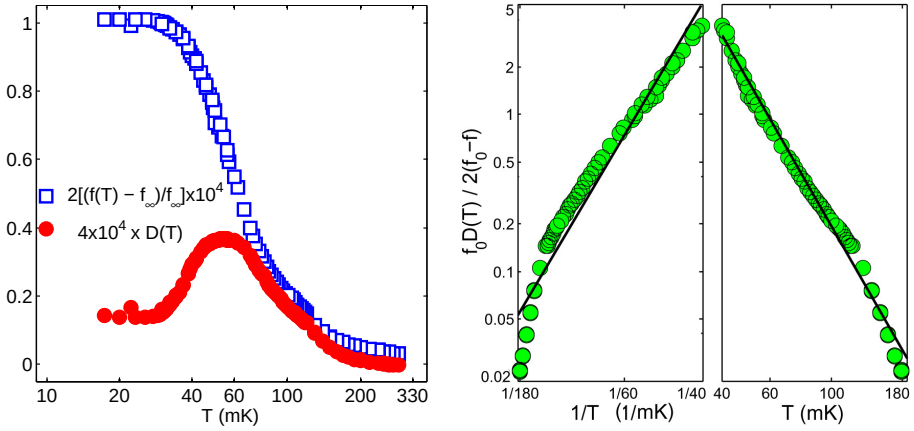

(c) Left: experimentally observed temperature-dependent susceptibility of solid helium at low-velocity, and corresponding relaxation time (right).

Figure 5.13: Susceptibilities and relaxation times for a Debye material, a glass, and solid helium observations. Black lines are guides to the eye.

Each theoretical T-dependent susceptibility is shown with its generating probability distribution inset, with color scale proportional to T as in Fig. 5.12. For illustration, $\omega\tau_0$ is fixed at 0.04 (comparable to $\tau_0 \sim 10$ μs if $f_0 \sim 575$ Hz), and the energy barrier cutoff $\triangle_0 = 240$ for the D-C distribution.

In Fig. 5.13b, it is apparent that the glassy distribution of energy barriers indeed generates a relaxation power law, which appears as a straight line on log τ *vs* log T axes. The emergence of this power law is a striking signature of glassy physics which is robust compared to conclusions based only on the fit quality of the individual susceptibility shape parameters. Figure 5.13 demonstrates that a theoretical glassy distribution function of Arrhenius processes that cumulatively generates the appearance of a power law relaxation qualitatively agrees with the dynamic signatures of solid helium, yet with a remnant overall magnitude discrepancy that is also consistent with a superfluid inertial fraction.

The data exhibit power law relaxation, which is much more similar to glassy behavior than single-mode Debye response. The dissipation in Fig. 5.13c has been scaled up for clarity, by a factor that corresponds to the persistent magnitude discrepancy as summarized in Table 4.1 on page 60 (although this is a different sample). In particular, note that Fig. 5.13c is similar to Fig. 5.6a, c, and e, with the addition of a test for Arrhenius behavior.

The most natural way to generate a temperature-dependent probability distribution is to start with a distribution of relaxation times $G(\tau)$, and then - as we have done in this section - convert to a distribution of energy barriers $P(\triangle)$ by the transformation outlined in Eq. 5.11, and by assuming a microscopic Arrhenius activation $\tau(\Delta, T)$ (as, for instance, proposed by Nussinov *et al* [36]). Other glassy functions have been proposed for modeling solid helium [76, 77],

but they typically begin by directly specifying a temperature-independent distribution $P(\triangle)$, thus precluding the ability to best fit the time-and-temperature-dependent thermal response we observed.

Finally, it is critical to note that the theoretical treatment of the barrier probability distribution in this section is predicated on an excitation parameter that we have labeled T and which typically corresponds to genuine temperature in the classical literature. Yet, there is nothing physical about the notational choice, and it is trivial to develop the identical treatment as in Fig. 5.13 based on velocity as the microscopic generator of Arrhenius activation. In fact we already know this will work, based on the successful velocity-dependent analysis of 5.6b, d, and f on on page 75.

Although the notational substitution $T \rightarrow v^{0.4}$ in the preceding treatment is - as mentioned - trivial, the physical implications of associating the velocity with an effectively thermodynamic bath that activates conformational defect motion in exactly the same way as a temperature was not expected to occur in supersolid helium (although velocity-dependent relaxations were eventually observed [53]). It suggests that the probability distribution of glassy barriers is effectively melted by velocity, even at low temperature. Furthermore, the velocity activates the microscopic motion over this ensemble of barriers. It should be mentioned that this mechanism is, at the very least, a strikingly different physical picture than a traditional superfluid critical velocity.

5.7 Implications of a temperature-dependent ensemble

At low temperature, the distribution in Fig. 5.6b is peaked at a particular energy gap, much like a single-mode Debye material. Temperature then has two effects on such a material: first it spreads out the distribution (physically generating more small-$\triangle$ barriers), and second, it increases the rate of tunneling over the particular barrier distribution at that temperature. Mechanical agitation could generate identical effects.

A temperature-dependent distribution function has not been discussed in the context of solid helium. But for classical glasses, it is actually fairly typical, and models material responses that are "thermorheologically complex" [78]. In other words, the temperature-dependent susceptibility of such a material cannot be separated from its time-dependent history. We have already discovered thermorheologically complex behavior in solid helium (see Fig. 4.11 on page 50), so it is not surprising to find that the relaxation time can also be best described by a thermorheologically complex glassy distribution function.

Whatever the dissipative microscopic mechanism - TLS [37, 38], dislocation network [10, 48, 79, 80], grain boundaries [32, 65, 41], superfluid dislocation cores [81], vortex fluid [39], etc. - the ensemble of such excitations appears to enter a jammed effective temperature state as it controls the onset of the inertial transition, and models should incorporate temperature-dependent glassy distributions of their respective microscopic excitations to better compare with solid helium observations.

The most important implication of the underlying distribution function is that it points the way towards a proper description of solid helium as given

by an agitation-dependent distribution of glassy energy barriers. Furthermore, it clarifies the physical origin of the ultra-slow temperature-dependent relaxations we discovered in Fig. 4.4 on page 39 and reported in Science [66]: the time constants we measured would correspond to the glassy response time of the equilibrium probability distribution function as temperature changes.

To move beyond the rough agreement found in Fig. 5.13, curve-fitting the susceptibilities will certainly be a necessary component of the analysis. However, given the obvious subtlety of the differences in susceptibility generated by completely different microscopic pictures, efforts to resolve the microscopic physics based only on fitting parameters of the real vs. imaginary anomaly will not be convincing. This situation is made even more dire by the very large discrepancy between dissipation strength and real inertia shift, which is consistent with (but certainly not proven to be) a superfluid inertia controlled by the glass, and which disrupts most attempts to fit a fully classical model to the whole data set with high fidelity. At the moment, the strongest evidence in support of the presence of a genuine superfluid term remains the blocked annulus experiments, and not this magnitude discrepancy.

In addition, the specific heat dependence of such a glassy distribution is a necessary prediction to compare with measurements by Moses Chan's group [82, 83, 84], as the Los Alamos theory group has done [77] for the following static (temperature-independent) glassy distribution function:

$$P(\triangle) = A\left[1 - \tanh\left(\frac{\triangle - \triangle_c}{W}\right)\right] \tag{5.13}$$

where A is a normalization constant, and W controls the rolloff width above the high-energy cutoff Δ_c. This static distribution is qualitatively very similar to the high-temperature limit of the distribution function we used in Fig. 5.13b, and it

agrees with the measured specific heat of solid helium [77]. We therefore expect that Eq. 5.12 (or perhaps a temperature-dependent extension of Eq. 5.13) would be able to generate reasonable fidelity with respect to both the specific heat observations *and* the ultra-slow dynamical equilibration (Fig. 4.11 on page 50) of solid helium.

If the still-unexplained magnitude discrepancy - along with the blocked-annulus experiments - reveals the presence of a genuine superfluid fraction in solid helium, its discovery would be most convincingly confirmed by directly observing flowing supercurrents through the solid.

CHAPTER 6

TOWARDS DIRECT SUPERFLUID FLOW THROUGH SOLID ^{4}HE

6.1 Direct flow measurements

Though the blocked annulus experiments [8, 27] are strongly suggestive of macroscopic phase coherence, direct hydrodynamic flow associated with the Kim and Chan effect has not been observed. Resonant torsion oscillators are of course unable to measure DC superflow in principle, and gyroscopes [85, 86] of sufficient sensitivity to observe persistent currents down to μm/s velocities have not yet been developed.

Direct strain-driven flow has been attempted with null results [33, 7]. Because of the solid bulk modulus, however, it is not clear how much flow within the sample should be expected (if any) due merely to compressive strain applied at the solid helium lattice boundary. The low-frequency Reppy group device from Ref. [7] is shown in Fig. 6.1, to illustrate this class of boundary-strain induced flow experiments.

To date, the only DC flow experiment that has demonstrated measurable mass transport off the melting curve is the "UMass Sandwich" experiment of Ray and Hallock [34]. The apparatus consists of two porous Vycor straws that connect (in parallel) a warm superfluid bath to a low temperature solid ^{4}He sample (the helium remains superfluid even at the low-temperature end of the straws because solidification is suppressed by the Vycor pores). Thus, liquid flow through the solid - generated by pressurizing the top of one straw - may be detected as a pressure change at the top of the other.

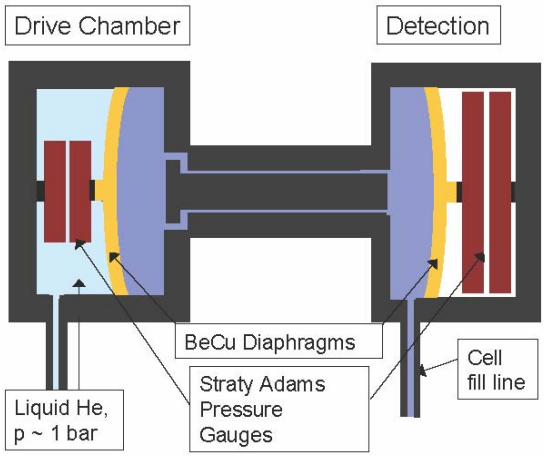

Figure 6.1: The low-frequency compressive-strain flow test device used by the Reppy group. No flow was observed through the solid. From [7].

With this apparatus, pressure changes were indeed observed above a few bars above the melting curve and at temperatures above 400 mK. However, a major drawback of this design is the large thermal heat leak to the solid sample, created by maintaining the top of the porous helium straws at warm enough temperatures to be in the liquid phase. Because of this, the experiment cannot practically cool below T_* as measured by the torsion oscillators, and therefore cannot determine whether the Kim and Chan effect is associated with DC superflow or not. The observations of flow that were made at high temperature are themselves not associated with any inertial anomalies measured by torsion oscillators, and so their origins remain a mystery. Furthermore, it has been argued that the results could possibly be explained by the "frost heave" effect of elastic intrusion by newly crystallizing solid under pressure, and not necessarily by mass transport *through* the solid [7].

6.1.1 Prospects for porous flow

We have developed a nanoporous supercurrent device designed to overcome these drawbacks and detect DC flow at low temperatures if it is associated with the Kim and Chan effect. The device is somewhat related to the UMass Sandwich in schematic form, in that it is designed to generate flow from one porous superfluid bath and detect it on the other side of a solid sample as a density change in another. However, the flow is generated in our device not by hydrostatic force on the liquid (which requires a thermal gradient and associated heat leak) but by electrostatic force from capacitive electrodes encasing the porous superfluid reservoirs. Therefore, the whole experiment can be cooled to the base temperature of the refrigerator, below T_*.

Of course, it is not usually possible to have a solid in thermodynamic equilibrium with its liquid far above the melting curve. This situation is, however, allowed in the special case of confinement within nanoscale pores, which prevents nucleation of solid seed crystals of sufficient size to propagate and thereby suppresses the porous melting curve to far above the bulk (up to $\sim 10^1$ bars over, see Fig. 6.2). Therefore, a suitable flow can be arranged between patterned porous glass regions (that will remain superfluid) and etched bulk microcavities that will contain solid crystals when pressurized.

Since the whole cell will be cold, the bulk solid in the fill line prevents one from applying hydrostatic pressure to the superfluid reservoirs. And, applying hydrostatic strain directly to the cold solid lattice as in Fig. 6.1 has been demonstrated to give no corresponding flow [33, 7]. For these reasons, we designed our device to generate flow by application of an electrostatic potential to capacitor plates sputtered on either side of the patterned porous superfluid reservoirs.

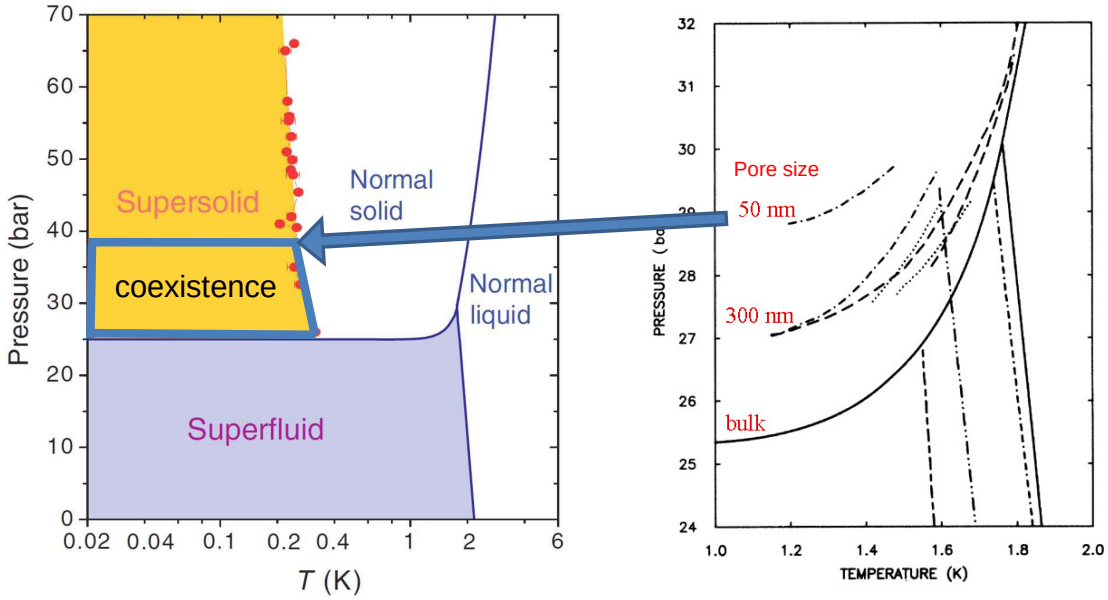

Figure 6.2: Phase diagram showing suppressed porous melting curve and coexistence region in which a new class of hydrodynamic devices can probe superfluid currents through "supersolid" helium samples. Schematic diagram on the left adapted from the original supersolid observation [8]; that on the right adapted from observations of the porous suppression of the melting curve [9].

The critical difference between this class of experiment and the compressive boundary strain experiments such as depicted in Fig. 6.1 is that the electric field is expected to penetrate the superfluid reservoir volume and change the chemical potential for the whole dielectric superfluid mass. If there exists any hydrodynamic coupling between a superfluid reservoir and a solid ^{4}He sample, this induced chemical potential change should be rapidly equilibrated by superflow through the solid.

By a straightforward equating of the free energy density of polarization with the free energy per volume of compression $\kappa_b^{-1} \approx 10^{-7}\,\mathrm{Pa}^{-1}$ [87] of low-temperature superfluid helium in a parallel-plate capacitor, we expect the application of a DC voltage V_{bias} to increase the equilibrium density ρ within a porous dielectric

superfluid by roughly the following order of magnitude:

$$\frac{\triangle\rho}{\rho} \approx \epsilon_0 \left(\epsilon_4 - 1\right) \left(\frac{V_{\text{bias}}}{d}\right)^2 \kappa_b^{-1} \tag{6.1}$$

where ϵ_0 is the vacuum permittivity, $\epsilon_4 \approx 1.04$ is the relative dielectric permittivity of helium, and d is the thickness of the porous dielectric layer. A schematic of the capacitor plate arrangement in relation to the two porous superfluid reservoirs and bulk microcavities is shown in Fig. 6.3.

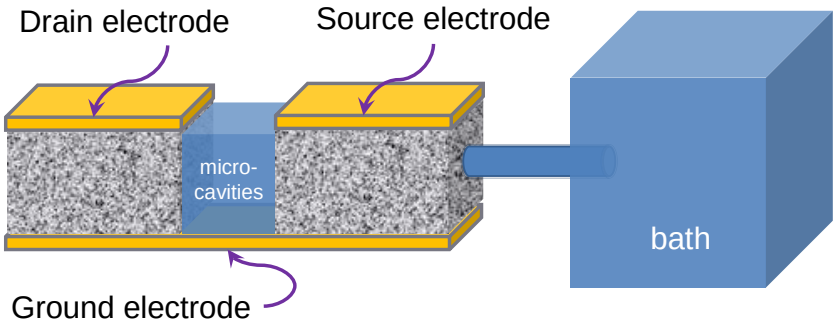

Figure 6.3: Schematic cross-section of a nanoporous supercurrent flow device. Porous glass reservoirs contain superfluid in hydrodynamic contact with solid ^{4}He microcrystals. The drain reservoir is completely isolated from the solid bath, except for flow which may pass through the patterned microcavities.

Effects due to porosity and glass dielectric screening are not included; Eq. 6.1 is presented not for precise predictive power but in order to convince the reader that microfabricated (as opposed to machined bulk Vycor, for instance) porous capacitors are required for this device geometry, since 5 volts across even a 1-micron capacitor is expected to give only a change in capacitance $\frac{\triangle C}{C_0} \sim \frac{\triangle\rho}{\rho} \sim$ 1 ppm, which is near our sensitivity limit.

6.1.2 Fabrication of porous capacitors and microcavities

We would like rather large volume porous superfluid reservoirs, so that C_0 is large compared to stray capacitances, and so that the mass depletion due to

exiting superflow from one reservoir remains a small change. These constraints demand large-aspect ratio (i.e. thin, large-area) microfabricated capacitors. Our largest chip design therefore uses two semidodecagonal electrodes each taking roughly half the area of a ~2-inch diameter wafer die, with facing edges abutting the microcrystals, and a porous layer thickness of ~0.5 micron. The resulting capacitance of each single electrode is ~31 nF, which is a relatively large value compared to those in typical helium devices.

The facing edges enclose a linear array of 432 microcrystals, each of which is ~20x4x3 microns^3, with flow directed in parallel across the 3-micron width separating the two porous reservoirs (see Fig. 6.3). The porous glass dielectric material is formulated by spin-on techniques, based on a recipe originally developed by Shu Yang *et al* for reducing *RC* delays in semiconductor interconnects [12]. Microfabrication was conducted at the Cornell Nanoscale Facility on 4″ Si wafers. Following is the list of processing steps and measured film thicknesses for a successful device:

1. Deposit 270-nm thick SiO_2layer (PECVD at 400°C) as insulating barrier on Si wafer.
2. Blanket sputter 83-nm thick chrome electrode layer to serve as ground electrode.
3. Pattern die outlines and saw streets using standard photolithography and chrome wet-etch.
4. Spin-on liquid glass solution containing polymer porogen (see recipe in Appendix C.1).
5. Burn-out porogen in anneal furnace (see temperature profile in Appendix C.1). Final porous film thickness of 450 nm. See Fig. 6.4 for reference.

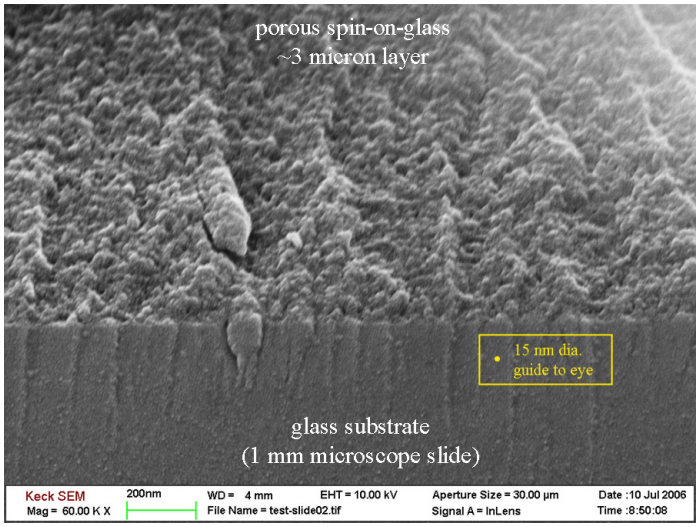

Figure 6.4: Typical cross section view of a porous spin-on-glass layer. From a test device (no electrodes). 15 nm circular guide to eye shown. (Final films on real devices had finer pore diameters, typically smaller than 5 nm.)

6. Deposit 159-nm thick SiO_2 layer (PECVD at 320°C) as pore-sealing barrier.

7. Sputter ~100-nm thick blanket aluminum film as top electrodes.

8. Pattern 3-micron wide trench across electrodes to split them, using standard photolithography and plasma Al etchback on PT740. Also etch ground electrode pad pattern, and clear circumferential edges.

9. DRIE etch (CF_4) trench down through oxide barriers and porous glass layer, preventing any porous paths directly between the two superfluid reservoirs.

10. Deposit 3.7 micron a-Si layer (PECVD at 320°C) as sacrificial cavity template layer.

11. Clear a-Si from everywhere except trench-fill (see Fig. 6.5 far left) using optical lithography and SF_6/O_2 plasma etchback.

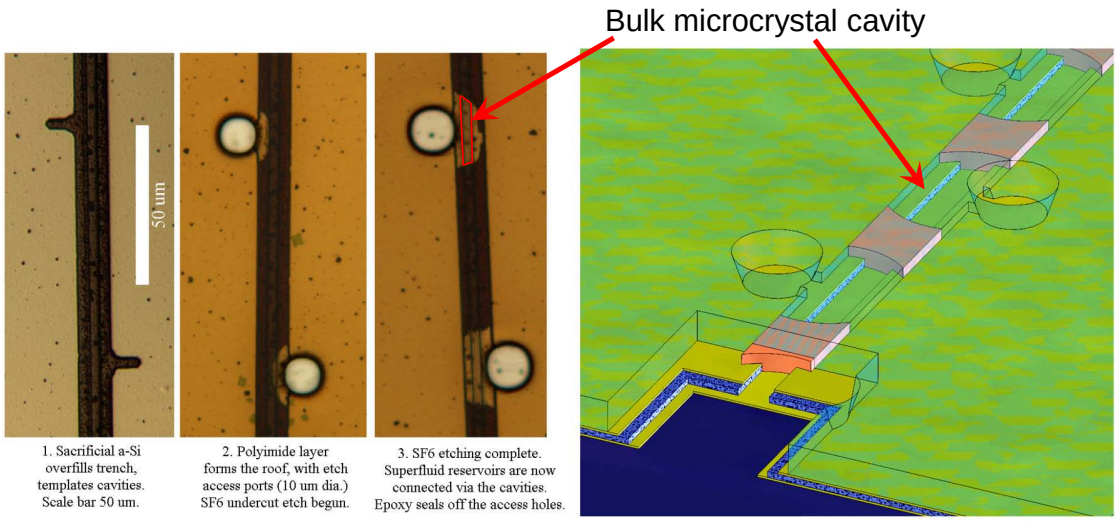

Figure 6.5: Left: Sequence of three optical micrographs showing microcavity formation by SF_6 plasma etchback of sacrificial silicon trench-fill (via etch-access holes in the polyimide roof layer). Right: Corresponding 3D device schematic to scale.

12. Deposit 5.8 micron PWDC-1000 photosensitive polyimide layer by spin-coating. Expose pattern for etch access holes, develop and cure bake at 300°C.

13. Dice chips using wafer saw.

14. Etch microcavities by SF_6/O_2 plasma under-etch, removing sacrificial a-Si from beneath polyimide roof layer. See Fig. 6.5 for photographs of typical cavity formation sequence (only two of 432 cavities are visible at this magnification).

15. Mount chip to socket with small dab of Apiezon-N grease on back of wafer.

16. Wire-bond electrodes to coax-pin feedthroughs on chip socket using fine gold wires and silver epoxy (Epo-Tek EE129-4).

17. Mask-off a small section of one electrode area using Kapton tape, for future access to bath.

18. Swirl-coat 5 drops of solution made up of 38%$_{wt}$ Apiezon-N grease in mineral spirits over wafer to seal etch access holes (don't use epoxy). Pump out excess solvent in a bell jar.

19. Lift Kapton tape mask and scratch away top electrode layer using a sharp blade, to expose pores to air.

20. Burn out short-circuits by applying constant current with 18V-max supply. Check capacitances and install chip in high-pressure cell on the mixing chamber (see Fig. 6.6).

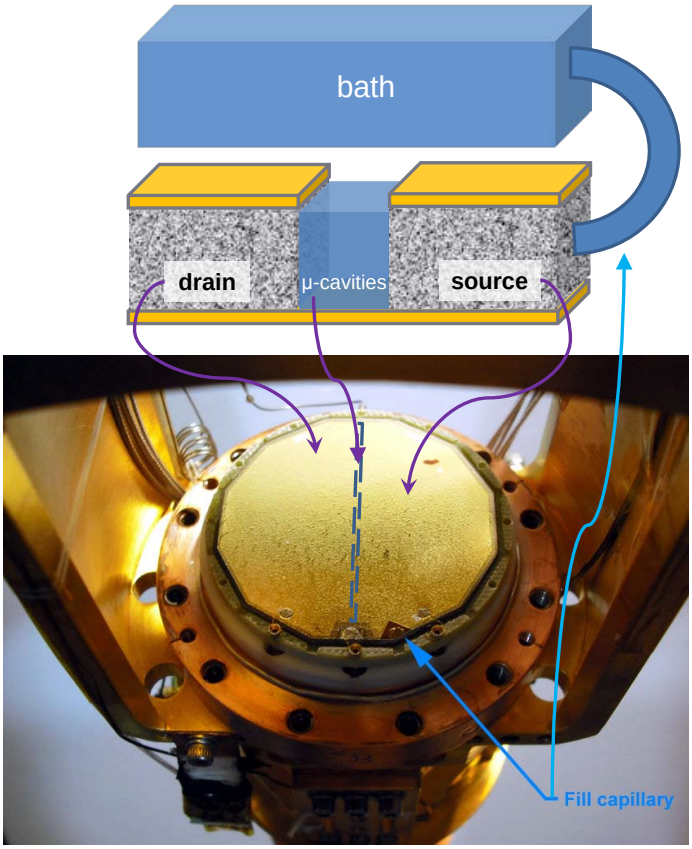

Figure 6.6: Photograph and schematic of a nanoporous supercurrent device mounted on the cryostat, with high-pressure copper cell unsealed for visibility. Three electrode wires are visible near the bottom of the chip, connecting via sealed feedthroughs to coax.

There are three fatal defects to be avoided: the first is the possibility of rem-

nant porous hydrodynamic paths that short out the microcavities, the second is a top-sealing layer that is too thick (and shatters upon cooling), and the third is a bad porous dielectric layer: either by being non-porous (i.e. fully dense and unpercolated), or by having bad film quality. The first problem is easily avoided by careful etching in step 9, with verification that the etch proceeds all the way into the barrier oxide layer (so that the trench is cleared). The top-coat of grease can be skillfully applied (i.e. thin enough) after some swirl practice (don't bother trying epoxy: it is too thick and shatters upon cooling). The porous spin-on chemistry, on the other hand, is the most painstaking part of the process with the least process latitude. See Appendix C.1 for the recipe, including steps to reduce particulate contamination. Films should be optically clear before placing in the anneal furnace.

Also, note that there is (as of the time of this writing) a remaining set of unfinished wafers with porous glass layers (from the same batch as the successful device discussed below) in storage. The wafers are complete through step 7. They were purposefully left in this state to allow arbitrary new cavity designs to be quickly implemented in future devices (since the difficult porous spin-on chemistry steps are already complete).

6.2 Nanoporous supercurrents through microcavities

One wafer - marked "Q" - containing two dies - was processed successfully according to the steps in Sec. 6.1.2. The larger die of these two - "Q1" - is shown in the photograph in Fig. 6.6. Background DC flow tests were undertaken to characterize the mechanical cross-talk between electrodes, and to verify that

the pores are open and percolated, and that the microcavities are connected to each superfluid reservoir. The simplest test, primarily concerning the pore structure, is shown in Fig. 6.7 with results for capacitance measurements in the empty, normal fluid (~3K, ~1 bar) and superfluid (~19 mK, ~1 bar) states. The capacitance is measured by a standard balanced-bridge technique as illustrated.

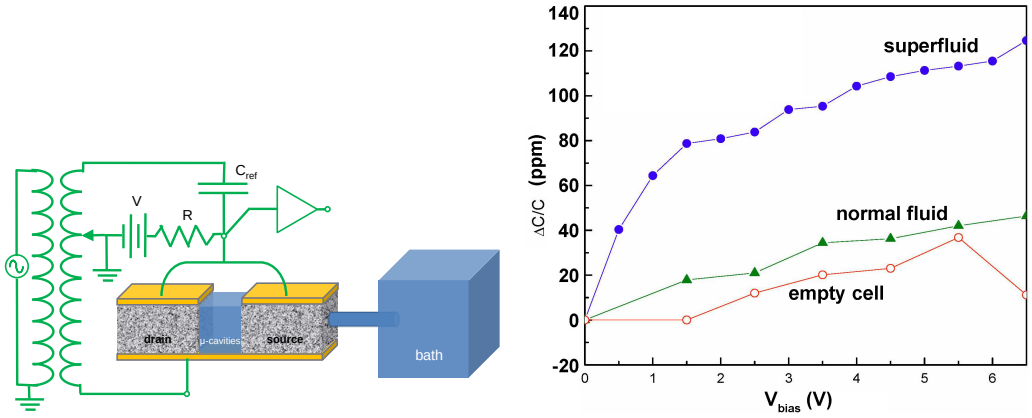

(a) Circuit (b) Observed capacitance changes

Figure 6.7: Verification that superfluid can be forced to flow into the pores. Capacitance of source+drain reservoirs - shown in (b) for various operating conditions - was observed using the circuit in (a). Normal fluid $(T > T_\lambda)$ is almost completely locked by viscosity, giving similar response as the empty cell. Supercurrents (at 19 mK) from the bath into the porous reservoirs $(T \ll T_\lambda)$ increase the capacitance measurably above the mechanical background response. Error bars not yet available.

The marked increase in capacitance change as a function of voltage - in the superfluid case versus the normal - indicates the ability to drive supercurrents from the bulk bath into one or both reservoirs, via the open pore region created in processing step 19. In fact, this experimental configuration may be used above the melting curve as a real test of supersolid flow, to test whether supercurrents can be driven from a bulk solid helium bath to a bulk porous superfluid reservoir by application of a chemical potential to the superfluid.

A different configuration, designed to test flow specifically through the mi-

crocavities, was tested under superfluid conditions, to provide a baseline measurement. This experiment - repeated above the melting curve - would constitute the first test of flow through micron-scale solid samples, and is illustrated in Fig. 6.8.

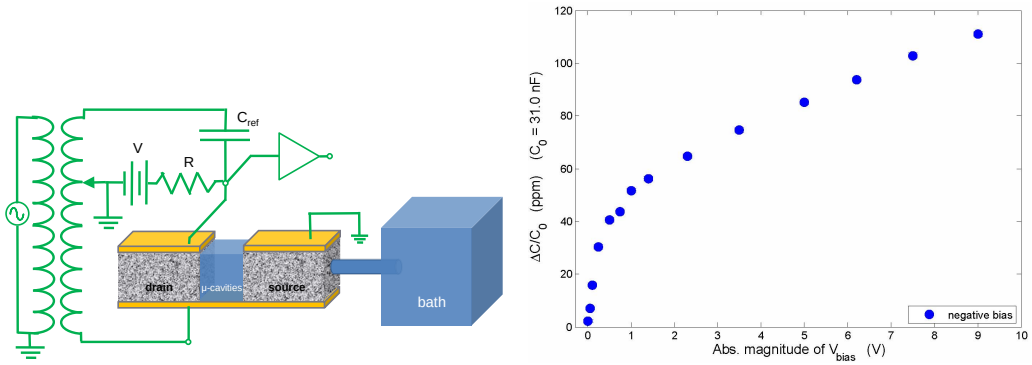

(a) Circuit (b) Observed capacitance changes

Figure 6.8: Large increase in capacitance indicates probable observation of superflow through the microcavities into the drain reservoir (b), using the circuit in (a) at 19 mK, with 1.1 bar ^{4}He vapor pressure. Baseline with normal fluid has not yet been measured. Error bars are shown, and typically smaller than the symbol size.

Though the corresponding baseline measurements with normal fluid in the pores are not yet available, it seems likely (due simply to the signal magnitudes compared to normal flow in Fig. 6.7) that the normal fluid case will be distinguishable against the data in Fig. 6.8, and therefore that this will serve as the observation of superfluid flow through the microcavities. Although the data do not fit the V^2 form expected by Eq. 6.1, the empty cell exhibits unanticipated mechanical crosstalk of unknown origin, which in fact dominates the observations at higher voltage (where it actually *decreases* the capacitance with increasing voltage). We attribute this behavior to unknown mechanical degrees of freedom associated with the porous spin-on-glass dielectric material, and believe that the non-V^2 dependence of the fluid signals is also plausibly due to this crosstalk.

Regardless of the crosstalk, the large observed *difference* between behavior with normal fluid versus superfluid in the pores constitutes the observation of superflow, and sets the scale by which flow through low-temperature solid ^{4}He microcrystals will be compared - assuming successful pressurization above the melting curve - in the near future.

APPENDIX A

TORSION OSCILLATOR THERMALIZATION

We studied the thermal time constants of the empty torsional oscillator (TO) by gluing a 100Ω Matsushita carbon resistance thermometer onto a test cell with the identical geometry and materials used in the actual TO. A test cell was used in an effort not to perturb the sensitive parameters of the actual torsional oscillator assembly. A repeat of the cooling protocol for the experiment outlined in Fig. 4.2 in this study indicated that there are always long time constants associated with the relaxation of the temperature of the Stycast walls of the empty cell; these are shown in Fig. A.1 alongside the full-cell mechanical relaxation data from Fig. 4.5. There are several differences. First, the change in the thermal and mechanical time constants appear to follow different power laws in temperature. Second, for $T > 75\,\mathrm{mK}$ the thermal time constants are an order of magnitude larger than the mechanical time constants. Thirdly, and perhaps most importantly, there appears to be no feature in the empty-cell thermal time constant at 75 mK, where the onset of the rise in the full-cell mechanical time constants begins.

Figure A.2 shows the real geometry of the ^{4}He-TO system and the location of the materials and thermal quantities of the system.

Since the relative magnitudes of the slow relaxation and fast change in f in Fig. 4.4 A and B indicates that it is indeed the slow relaxation of the solid ^{4}He that is contributing predominantly to the relaxation (as opposed to the slow thermalization of the Stycast chassis), there are two possibilities. The first is that the helium has a complicated temperature relaxation function $T_{4He}(t)$, whose precise form depends on the various quantities in the system (Kapitza

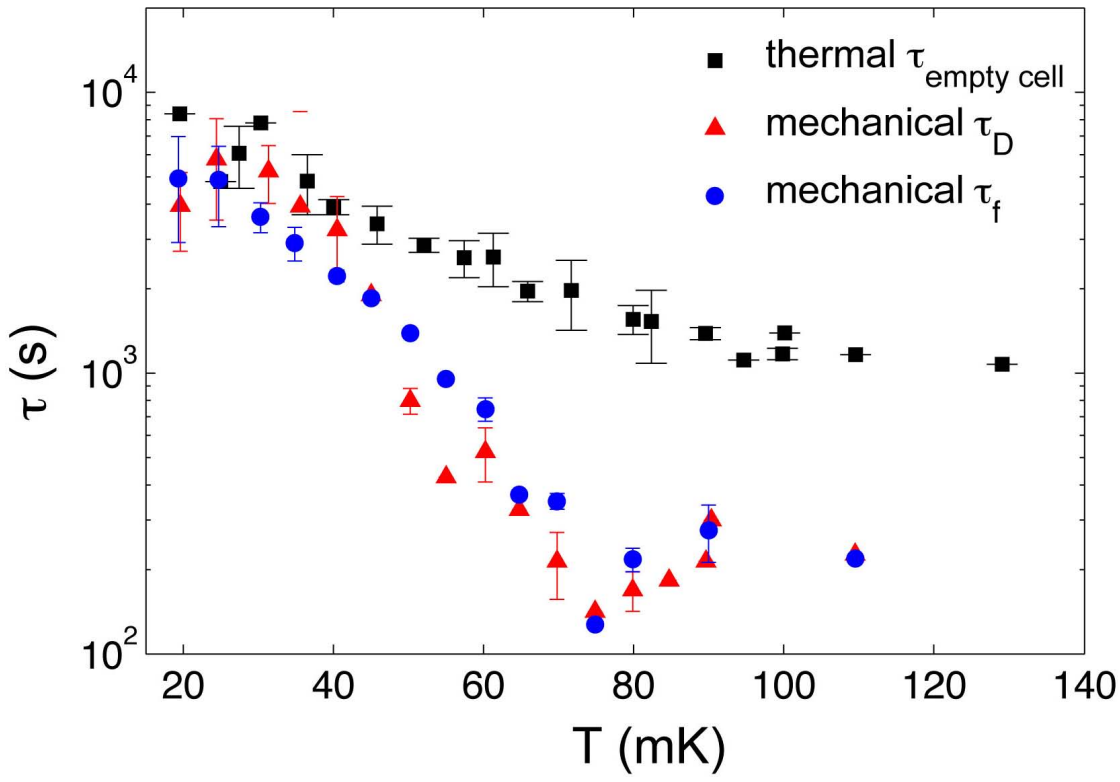

Figure A.1: The time constant for thermal relaxation of the empty cell (black squares) compared to the mechanical time constants for the relaxation of the dissipation (red triangles) and frequency (blue circles) of the full cell containing solid helium.

and thermal boundary resistances, thermal conductivities, heat capacities), and that the dissipation and frequency relaxation data of Fig. 4.4 A and B and of Fig. 4.7 A and B are simply independent measurements of this temperature relaxation function, according to the functionals $D\left[T_{4He}\left(t\right)\right]$ and $f\left[T_{4He}\left(t\right)\right]$, whose infinite-time curves would be the results shown in Fig. 4.1. To test this idea, one would need to measure directly the temperature of the helium within the $100-$ um- wide annular cavity, which is at present impossible.

However, there is a simple argument that shows that the complex relaxation dynamics of the solid ^{4}He we report (Figs.4.7 and 4.11) cannot be explained by the ^{4}He sample being out of thermal equilibrium with the mixing chamber

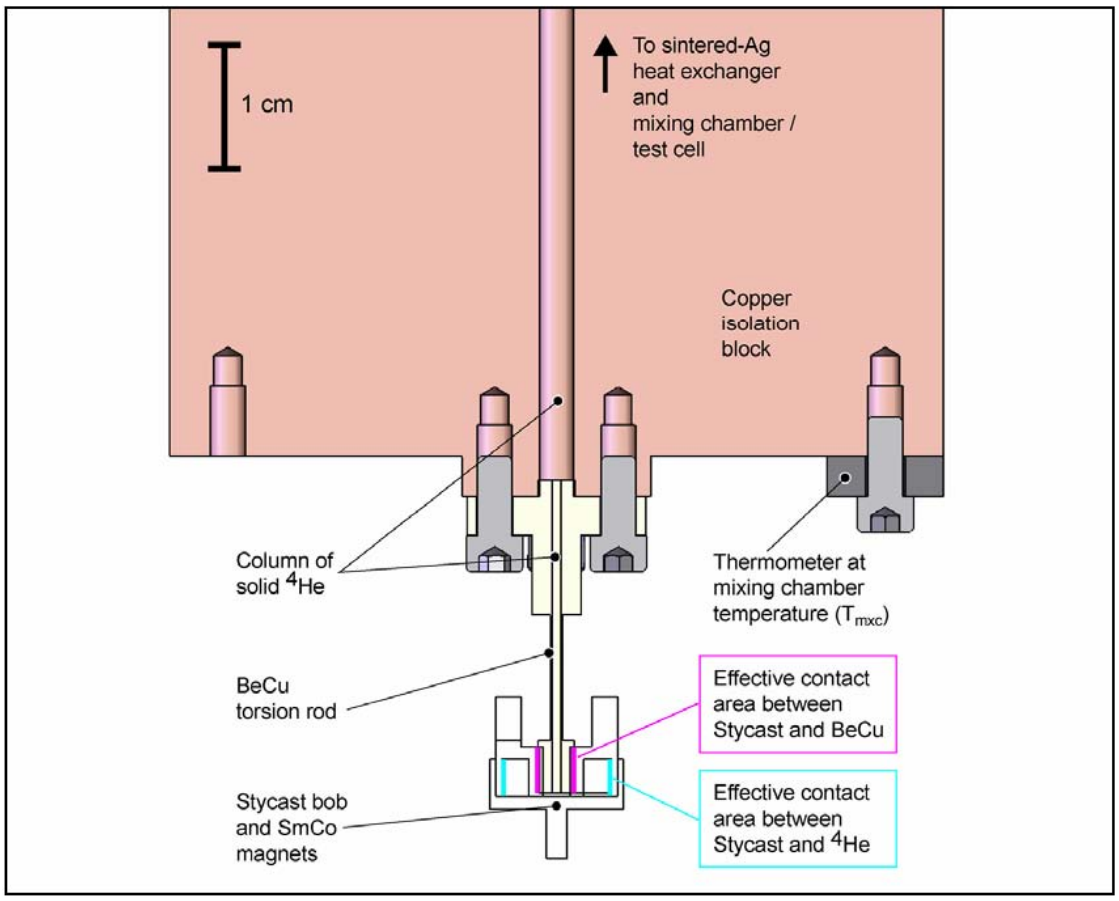

Figure A.2: Cross-sectional drawing (to scale) of materials in the torsional oscillator - ^{4}He apparatus. A correct thermal model of the system would include the temperature-dependence of the heat capacities and thermal conductivities of the copper isolation block, the BeCu torsion rod, the SmCo magnets, the solid ^{4}He, and the Stycast 1266 torsion bob, as well as the thermal boundary resistance at the interface between the Stycast and BeCu (shown in cross-section in magenta), the Kapitza resistance between the Stycast and the solid ^{4}He (shown in cross section in cyan), and the Kapitza resistance between the BeCu/Cu and the solid ^{4}He, whose interfacial area runs the entire length of the torsion rod and the central hole in the isolation block.

thermometer. For this argument, the time-dependent Davidson-Cole plot (Fig. 4.11) is an essential tool. The Davidson-Cole plot for the infinite-time curves $D\left[T_{4He}\left(t\right)\right]$ and $f\left[T_{4He}\left(t\right)\right]$ is shown in Fig. A.3A.

One usually thinks of this curve as being parametrized by the temperature of the helium, but if its temperature is changing as a function of time (and $T_{4He}\left(t\right)$

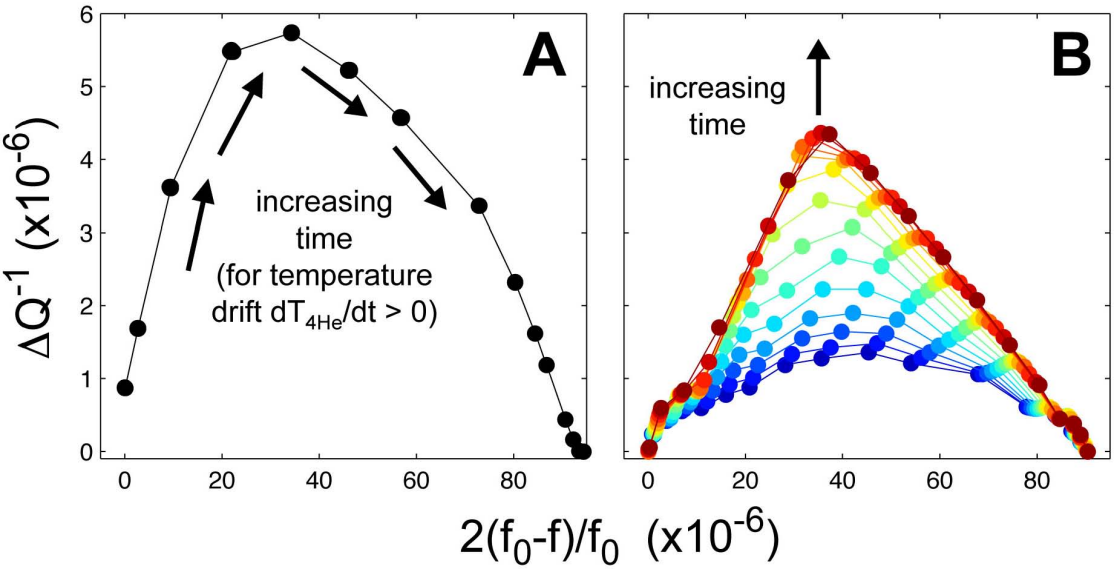

Figure A.3: **(A)** The time evolution of the Davidson-Cole plot for the dynamics described only by a changing $T_{4He}(t)$. The plot is shown for the case where the temperature increases with time (as would be expected if $T_{4He}(t)$ lagged the mixing chamber temperature T_{mxc} after an increase in T_{mxc}, as per the heating protocol outlined in 4.6). **(B)** The observed time evolution of the Davidson-Cole plot. These are the same data as Fig. 4.11; they reveal a more complicated relationship between the dynamics of the frequency and of the dissipation as the TO-^{4}He system evolves from its low-temperature state.

is changing slowly compared to Q/ω_0) one can regard as an equivalent parameter the time t. This means that the time-dependent Davidson-Cole plot would be indistinguishable from the static (infinite-time) plot – as a function of time the system would simply be moving along the single curve (depicted with a sequence of arrows in Fig. A.3A). The data from Fig. 4.11, reproduced in Fig. A.3B, demonstrate that this is not the case and lead us to the second conclusion: far richer relaxation dynamics exists in solid ^{4}He than would be produced by a mere delay in thermalization of the sample.

APPENDIX B

UNIFIED AGITATION AND TEMPERATURE

B.1 Automation of FID ringdowns

In order to acquire ~100 ringdowns that span the temperature range of the inertial anomaly without disturbing the sample by helium transfer, a high duty cycle was required. Each ringdown experiment spanned about 20 minutes, during which the temperature, oscillator ring-up, and detector dynamic range settings were controlled automatically by a Lab-VIEW program of nigh impenetrable complexity. During the ring-down, the resonant phase-locked loop (Fig. 2.7 on page 16) was switched automatically from the capacitors to the SQUID when the decaying signal dropped below the capacitor sensitivity at roughly 20 $^{um}/_{s}$. Fig. B.1 illustrates the sequence of a typical subset of the observations which were used to acquire the complete susceptibility maps.

B.2 Susceptibility at high velocity

We operate the torsion oscillator by applying a constant-magnitude oscillatory torque to the capacitive drive electrode at the resonance frequency, which - at a fixed temperature, and after transient effects decay - results in oscillation at constant RMS rim velocity. This rim velocity is what authors typically report in the literature to convey how much agitation the sample experiences during a given experiment. This is an important parameter to know when comparing experiments from various labs and operating conditions, because it is well known

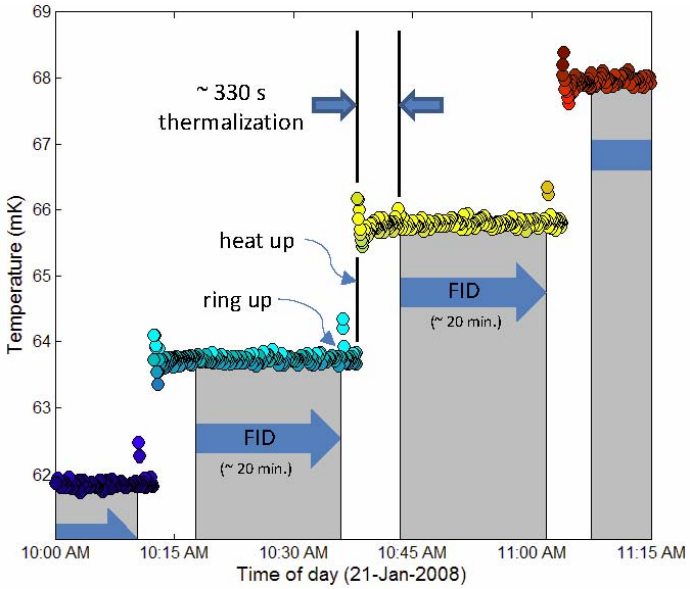

Figure B.1: Annotated mixing chamber temperature record, illustrating the automated procedure for thermalization and free-inertial-decay (FID) mapping. The oscillator amplitude typically decayed by more than 120 dB during each FID, and the resonance frequency increased by a maximum of about 50 ppm during the lowest-temperature FIDs.

that the purported supersolid signal is suppressed in samples driven at high agitation rates (i.e. at sufficiently high velocity).

However, it is important to note that at fixed (i.e. resonance) operation frequency, the oscillator's amplitude, velocity, and acceleration differ from each other only by proportionality constants. Therefore it is impossible to distinguish whether velocity is really the fundamental agitation parameter of interest (as, for instance, it would be relative to a true superfluid critical velocity) or whether the anomalous helium dynamics are instead suppressed fundamentally by perhaps an amplitude or acceleration dependence.

To elaborate, we note that the torque on the torsion oscillator body applies an inertial shear stress to the helium sample contained within, and it seems plausible that dynamic mechanical effects on the solid may be generated as a direct

result, and that these effects could generate the inertial anomaly. It is of course well known that the material exhibits just such a mechanical effect - namely the stiffening of the shear modulus - with largely an identical temperature profile to that of the inertial effect, and which demonstrates a shear stress or strain dependence as opposed to velocity [10]. However, the connection between the shear modulus stiffening and the inertial anomaly remains unknown. Within models that would directly connect the phenomena, it would probably be more useful to recast our measured susceptibility in terms of the oscillator inertial shear stress at the perimeter of the sample cavity (proportional to the measured acceleration) instead of the velocity.

However, following convention, we simply report our agitation magnitude in terms of the rim velocity, with the caveat that we do not mean to imply any necessarily fundamental role of velocity itself. Velocity may simply be a proxy measurement for a more fundamental parameter which is yet to be conclusively determined, with ramifications for linear response analysis presumed to eventually follow.

B.3 Power-law rates vs. Arrhenius activation

The internal dissipation rate is commonly modeled [36, 42] as an exponential function of temperature, $\tau \sim \exp\left(\frac{\triangle}{T}\right)$ - and might logically be extended to a model $\tau \sim \exp\left(\frac{\triangle_v}{v}\right)$. We find that the rate is actually given by power laws in v and T as is clear from the plots in Fig. , which show much better fits on log-log axes than on log vs. $1/T$ or $1/v$ axes.

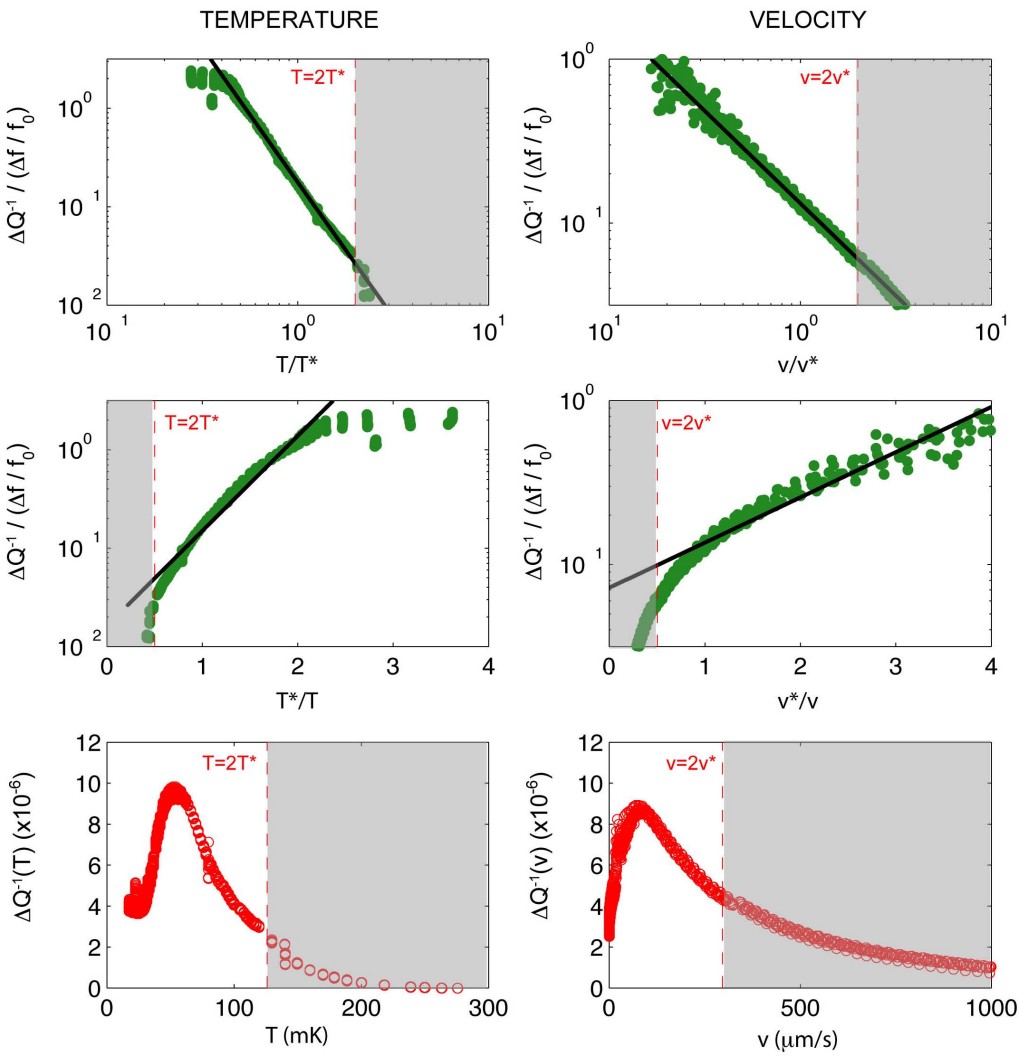

Figure B.2: The putative internal dissipative rate as a function of both temperature and velocity, illustrated with power-law fits *vs.* Arrhenius activation.

B.4 Velocity-temperature collapse

To get some feeling for the fit quality of collapsed ringdown data, Figure B.3 shows the predicted susceptibility surfaces for the incoherent sum of rates as noted in the text.

Alternatively, Figure B.4 shows the predicted susceptibility surfaces for some choices of ill-fitting parameters as noted.

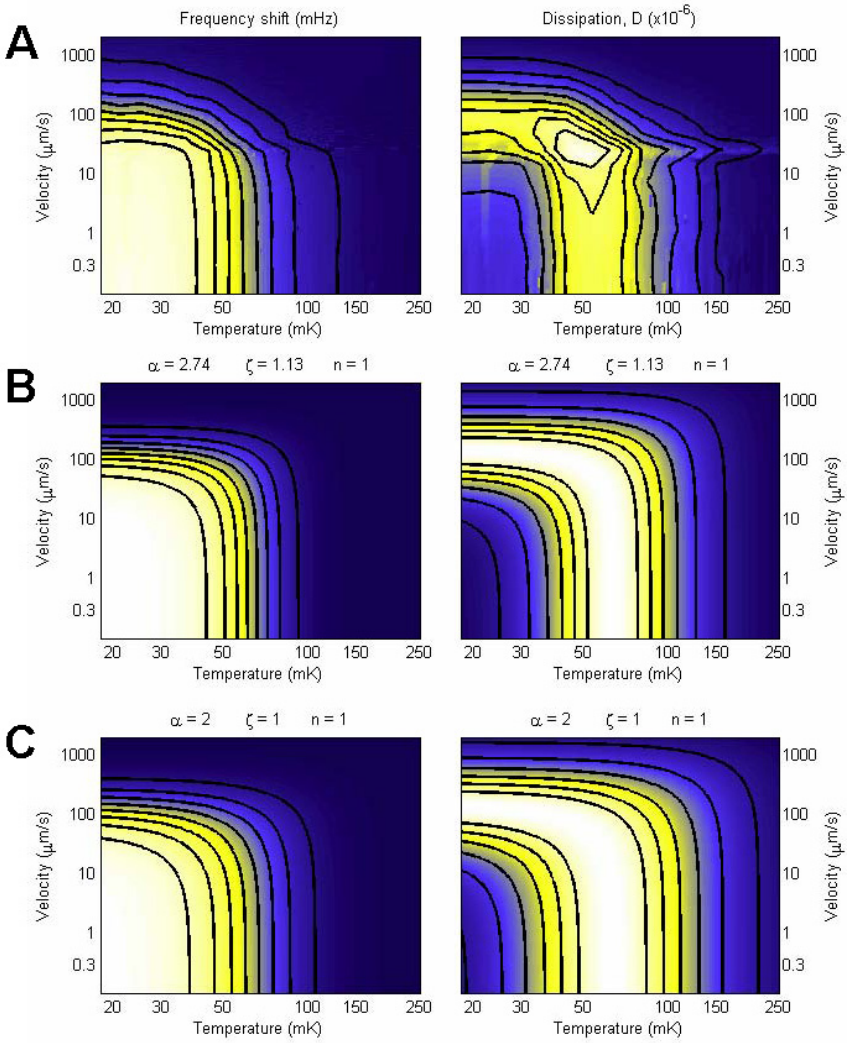

Figure B.3: Susceptibility surfaces measured **(A)** and predicted **(B)**, **(C)** for an incoherent sum of relaxation rates given by independent power laws of temperature and shear velocity. The exponents in **(B)** are simple integers as motivated by the T vs. $\sqrt{v}$ behavior in Fig. 5.6. The exponents in **(C)** are fitted to the data in Fig. 5.6 e and f, and their ratio is roughly 20% higher than in **(B)**. The dissipation superpeak is not predicted by this model.

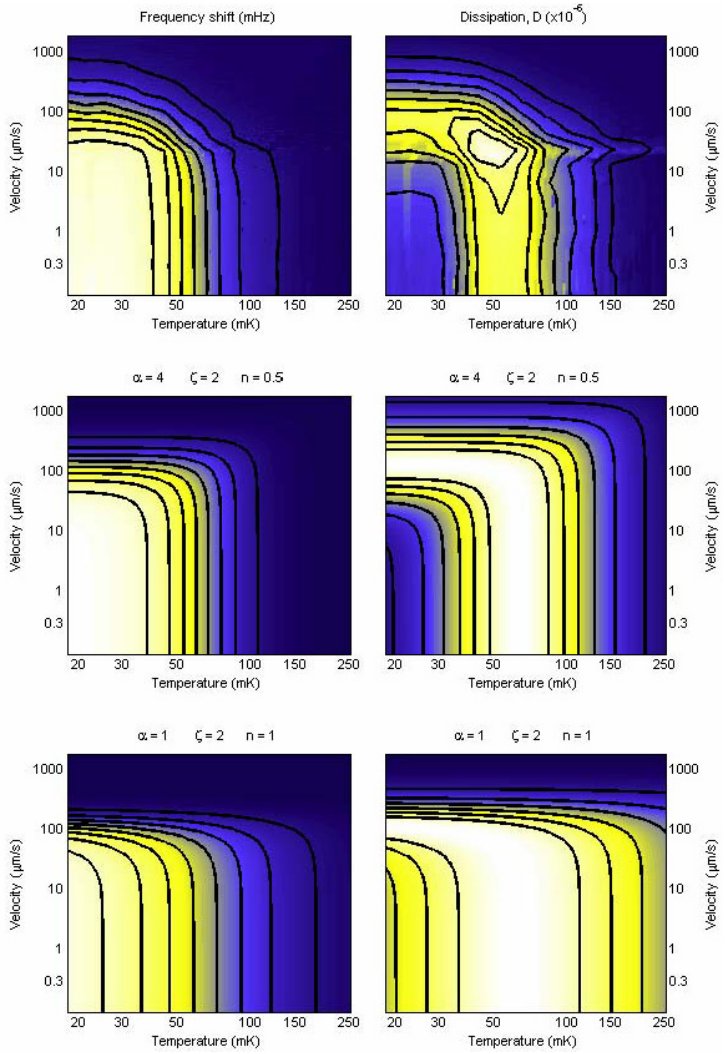

Figure B.4: Free-inertial-decay susceptibility data, and badly-fit models.

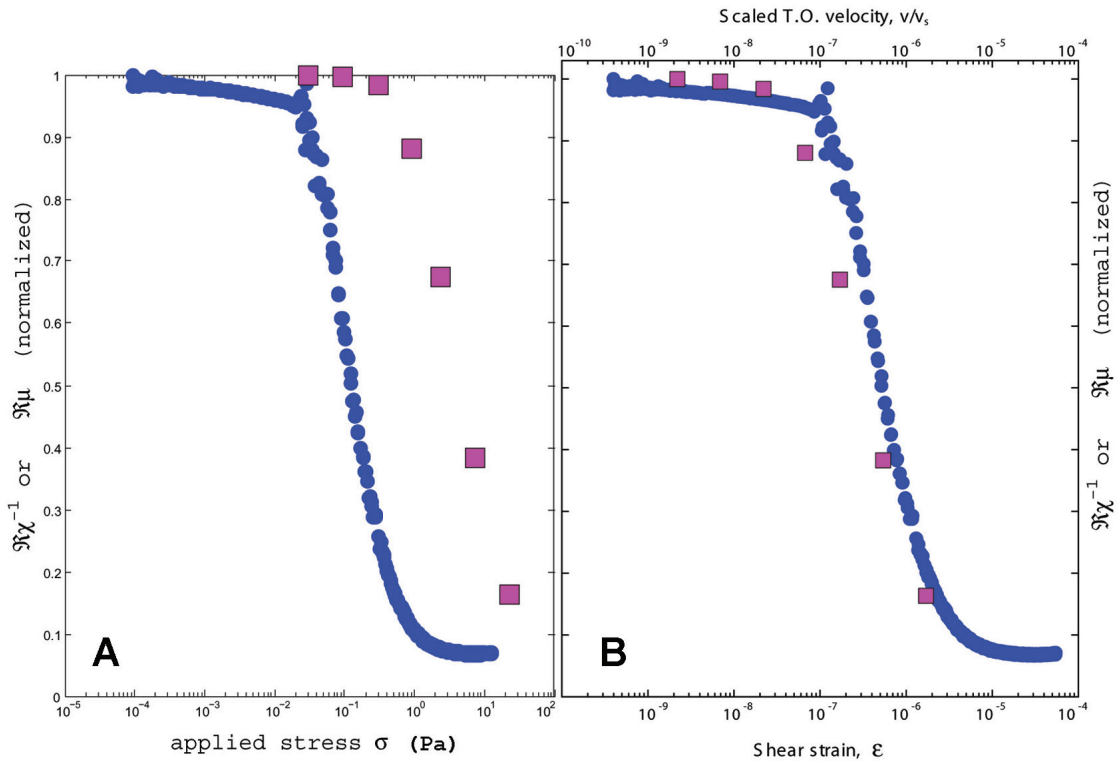

Figure B.5: **(A)** Real susceptibility of our torsion oscillator sample (blue dots) and the real part of the shear modulus, from [10] (purple squares), as a function of the inertial or applied shear stress. The data do not agree particularly well, as was noted also in [11]. **(B)** The same data as in **(A)**, except that the torsion oscillator frequency shift is now plotted as a function of rim velocity *scaled* by the bulk sound speed. A fairly robust agreement is observed empirically, but a mechanism by which this could be physically justified is unknown.

APPENDIX C

NANOPOROUS CHIP MICROFABRICATION

Fig. C.1 shows a schematic of the nanoporous chips mounted in a high-pressure copper cell that is thermally anchored to the mixing chamber. This schematic is meant to show all the functional parts of the nanoporous devices, from the nano-to-macroscale, which are otherwise difficult to capture in a single scale schematic. In particular, note that the fill line (which is blocked at the 1K pot) supplies a large bulk solid helium bath, which then has access to one of the porous reservoirs (the "source"). The "drain" reservoir only has access to helium via transport through the microcavities, which should contain solid helium when pressurized. The etch-access holes seen in Fig. 6.5 are sealed by a top layer of Apiezon-N grease.

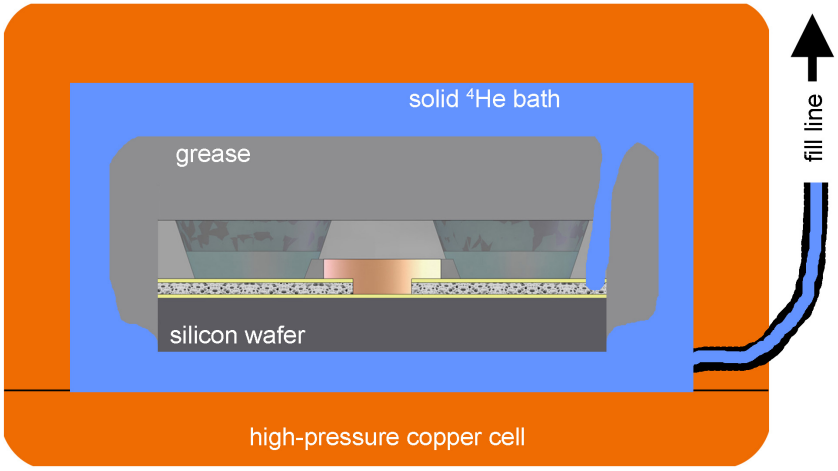

Figure C.1: Schematic cross-section showing nanoporous chip mounted in high-pressure copper cell. Electrical feedthroughs not shown. Microcavity shown at center in light orange, to scale relative to the porous reservoir thickness (lateral extent not to scale).

C.1 Porous glass film deposition

After some experimentation with various chemistries and furnace profiles, the following recipe and the temperature ramp shown in Fig. C.2 was found to give high-quality porous films. This recipe is essentially a subsection of the process described on page 102.

Start with these well-mixed, separated precursor solutions:

- "SOG" = 25%$_{wt}$ GR-650F glass flake from Techneglas; balance n-butanol
- "Porogen" = 25%$_{wt}$ Pluronic F88 block copolymer from BASF, 24%$_{wt}$ water; balance n-butanol

The porogen on its own is basically an advanced detergent and is quite stable. Its amphiphilicity seemed to widen the process latitude considerably over previously attempted (and unpredictable) recipes, particularly compared to triphenylsilanol. The SOG should be acquired fresh because the silanol groups have a finite shelf life. Both substances were available as rather large quantity free samples from their respective manufacturers.

The following recipe was found to work suitably:

1. Mix precursors in new clean plastic bottle overnight to achieve final solids loading of 25% in solution (this proportion controls the film thickness), with 36% loading of porogen relative to SOG (this proportion controls the porosity). 36% was sufficient to surpass the percolation threshold; higher porogen loading is expected to weaken the film.

2. Filter 3cc at a time into a new clean plastic bottle (changing 0.45 micron teflon syringe filters between each shot). Let the bottle settle for ~5 minutes.
3. Draw solution into a pipette from near the top of the fluid (the pipette tip should never drop near the bottom of the bottle, which tends to become contaminated with SOG particulate seeds dropping out of solution). Store the pipette in a beaker of n-butanol in-between extractions if spinning a series of wafers.
4. Dynamic dispense onto wafer (process step 4) @ 150 RPM for 4.0 sec.
5. Ramp at 1800 RPM/s to 5000 RPM, dwell 20 sec.
6. Soft-bake for 5 minutes each on successive hot plates: 95°C, 115°C, 170°C.
7. Chill plate at room temperature, then hard-bake in anneal tube (step 5).

It is important to pre-heat the oven to $\sim$ 300°C before inserting wafers; otherwise the temperature can oscillate wildly and cause porogen release and film collapse before vitrification.

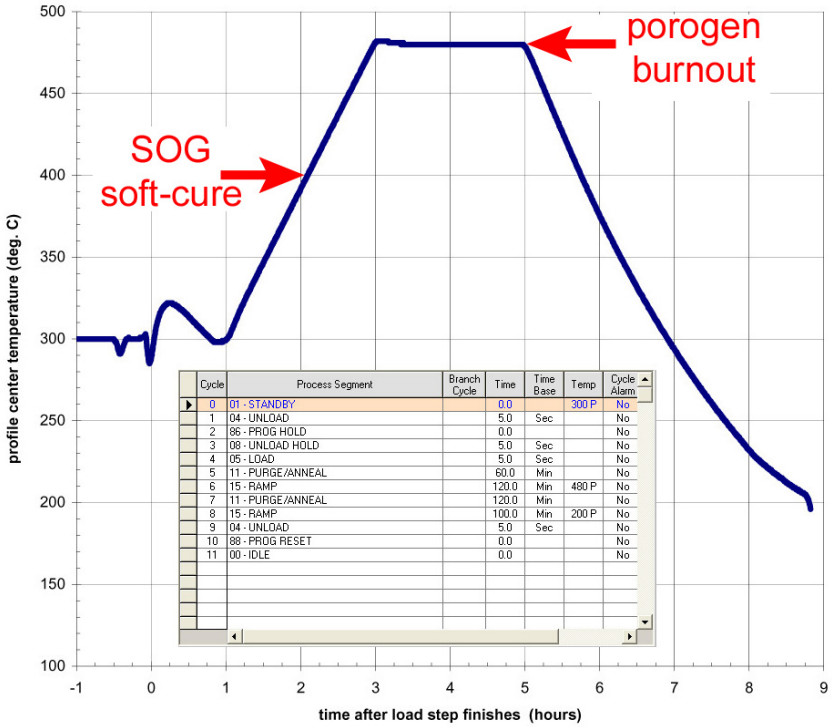

Cycle	Process Segment	Branch Cycle	Time	Time Base	Temp	Cycle Alarm
0	01 - STANDBY		0.0		300 P	No
1	04 - UNLOAD		5.0	Sec		No
2	86 - PROG HOLD		0.0			No
3	08 - UNLOAD HOLD		5.0	Sec		No
4	05 - LOAD		5.0	Sec		No
5	11 - PURGE/ANNEAL		60.0	Min		No
6	15 - RAMP		120.0	Min	480 P	No
7	11 - PURGE/ANNEAL		120.0	Min		No
8	15 - RAMP		100.0	Min	200 P	No
9	04 - UNLOAD		5.0	Sec		No
10	88 - PROG RESET		0.0			No
11	00 - IDLE		0.0			No

Figure C.2: Furnace temperature profile (and associated CNF anneal tube #1 recipe, inset) for vitrifying the glass matrix, and subsequently pyrolizing the block-copolymer porogen. This process (see [12]) is advantageous because the glass matrix is thermodynamically stabilized before the porogen is removed. This gave more reliable films than recipes which released the porogen before vitrification, which tended to collapse unpredictably.

APPENDIX D

FABRICATION DRAWINGS

Shop drawings that were particularly useful for the experiments described in this dissertation are included in this appendix. These as-submitted designs are of course highly specialized, and presumably require modification before being useful for different experiments. However, several components of these designs were both somewhat novel and extremely successful, and should be used in future apparatus design where applicable. In particular, the pressurized coax feedthrough assembly, flush-mounted pressure gauge, and liquid nitrogen cold trap designs are recommended.

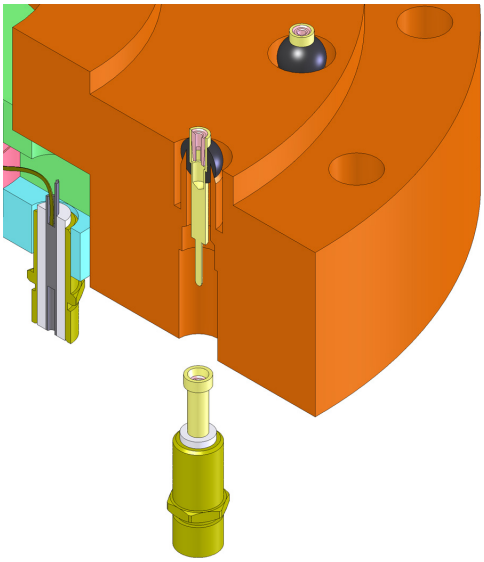

(a) Cross section cutaway schematic detail of high-pressure cell with microdot coax connector retracted below stycast-sealed coax feedthrough. The pressure gauge is partially visible at top left.

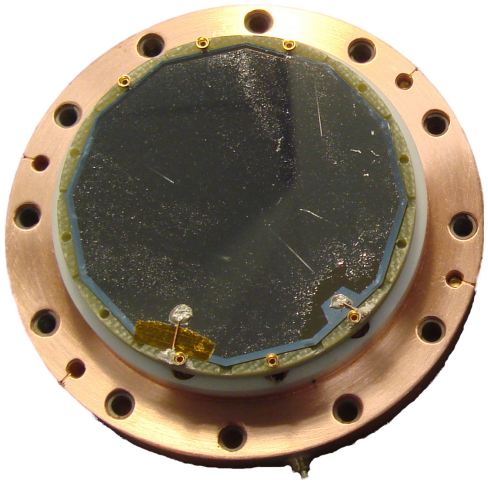

(b) Photograph of a nanoporous device installed in the cell (high-pressure cap removed). Wire-bonded device pins are inserted into sealed coax feedthroughs. Fill line braze boss is visible at photo bottom.

Figure D.1: High pressure cell - cutaway schematic and photograph.

D.1 Cryogenic pressurized coaxial feedthrough

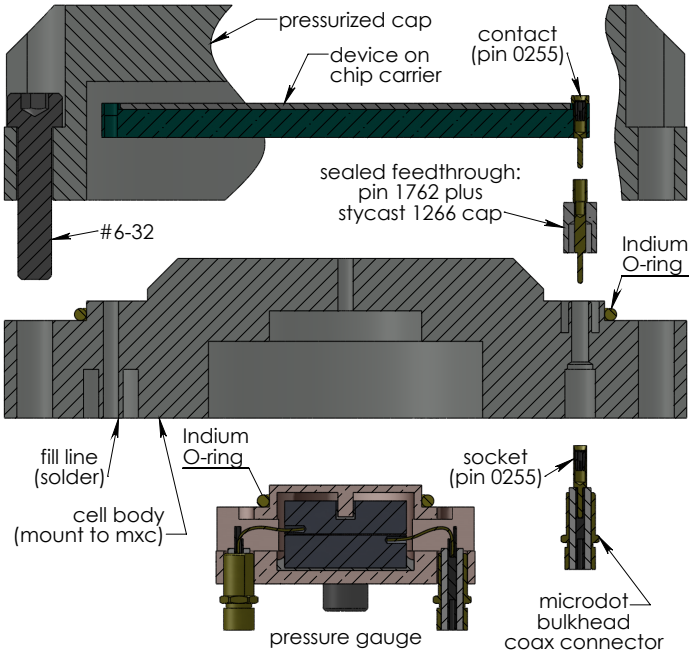

(a) Exploded overview of the high pressure cell.

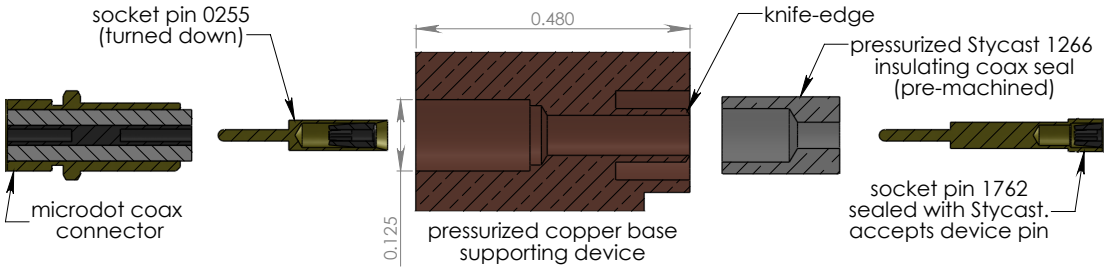

(b) Exploded view of the pressurized coaxial feedthrough. This design was extremely reliable once assembled, and is recommended. The spring-loaded pins are commercially available from Mill-Max. The crucial Stycast seal is created between a pre-machined Stycast socket, a knife-edge machined from the copper body, and a precision machined gold-plated pin receptacle. Once formed, the delicate parts of the feedthrough seal are flush or sunk below the cell body and cannot be easily disturbed. The remaining (screw-on) components of the feedthrough are replaceable.

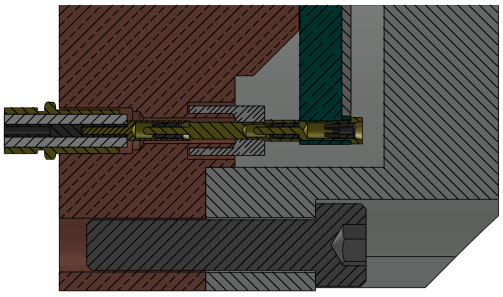

(c) Assembled view of pressurized coaxial pin feedthrough.

Figure D.2: Cross-section detail views of high pressure cell.

D.2 Nanoporous chip: wire-bonded chip carrier

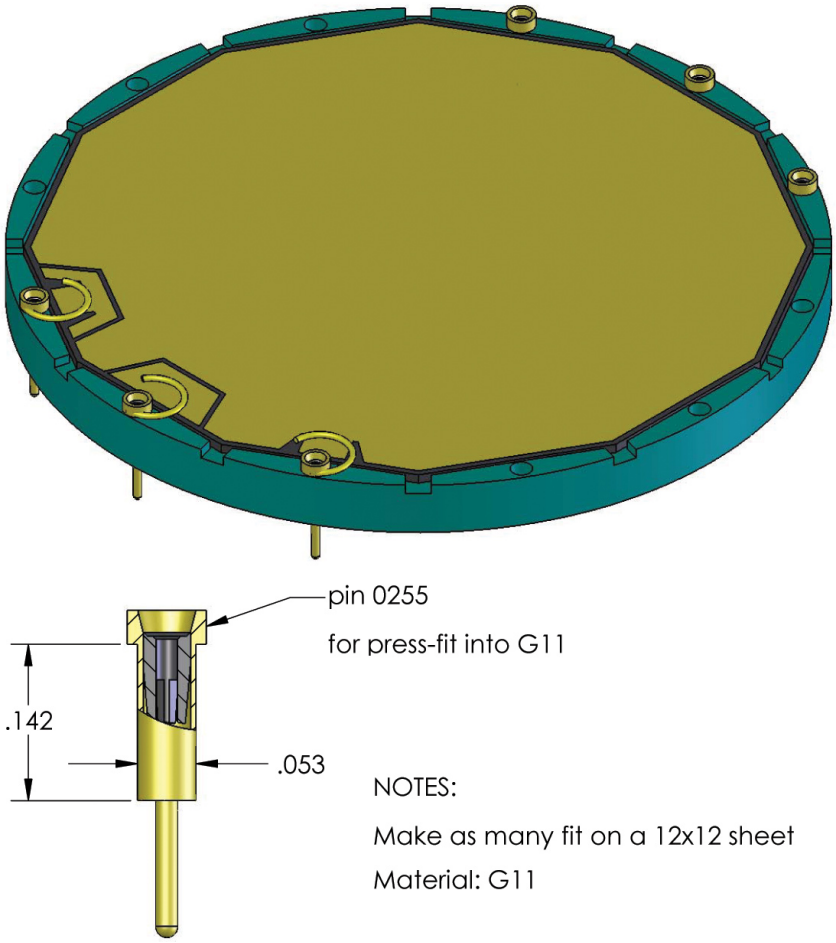

Figure D.3: Schematic view of a dodecagon-diced chip mounted to a fiberglass chip carrier. The device is wirebonded (via silver epoxy) to commercially available pins, which make mechanical and electrical contact to the sealed pin receptacles of the high-pressure cell (see Fig. D.2).

The carrier shown here is a 6-pin variant, with 3 pins allocated per device while the others pass through (allowing installation of two stacked 3-pin devices). The cell design (Fig. D.5) is easily modified to accept up to 12 sealed coax pins, and the gazebo (Fig. D.9) can accept a tall cap variant (Fig. D.7) that contains a stack of up to 4 devices. (The currently installed cell is, however, a 3-pin model that contains one device.)

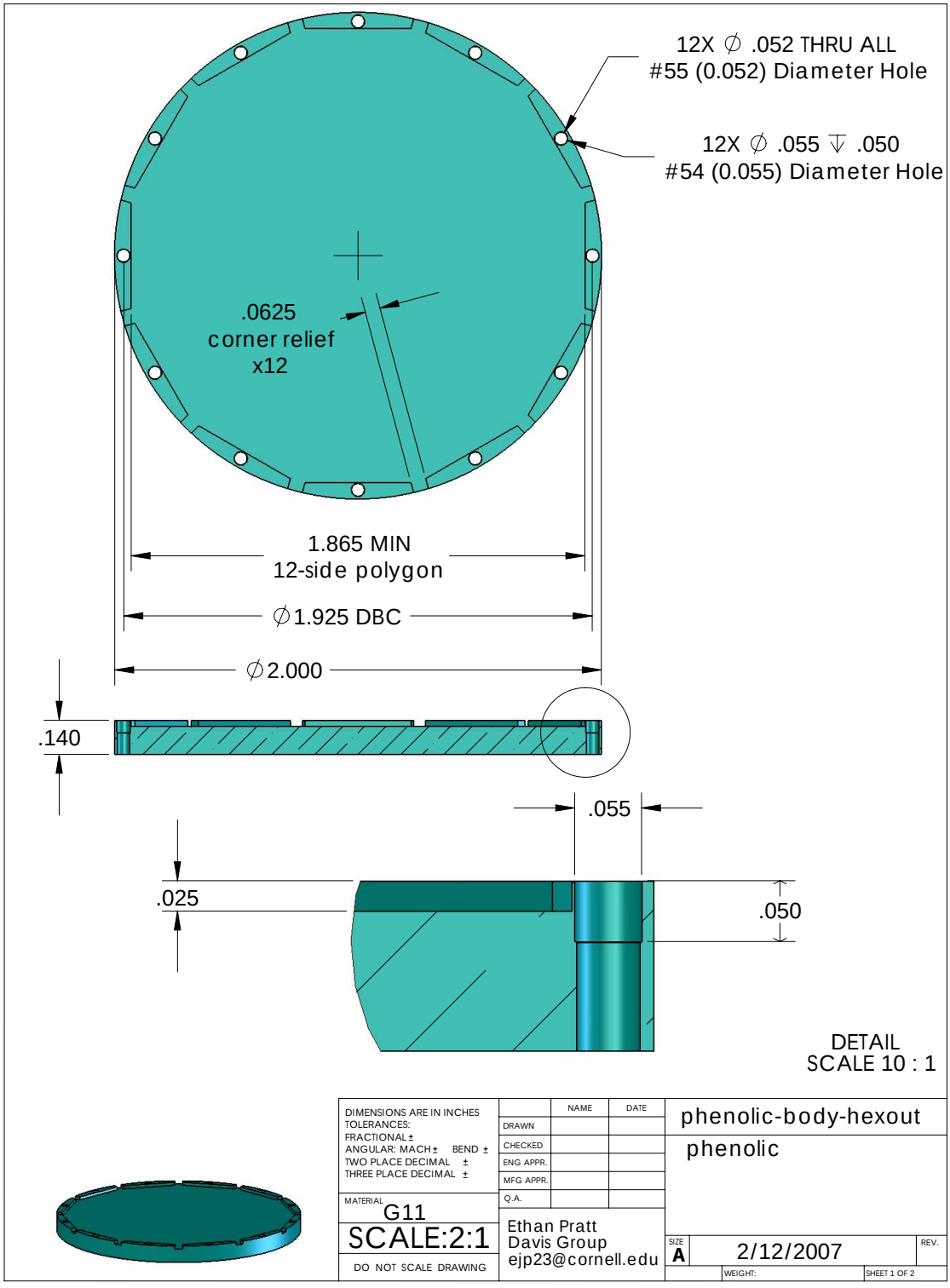

Figure D.4: Fiberglass chip carrier. Make several at once.

D.3 Nanoporous chip: high pressure cell

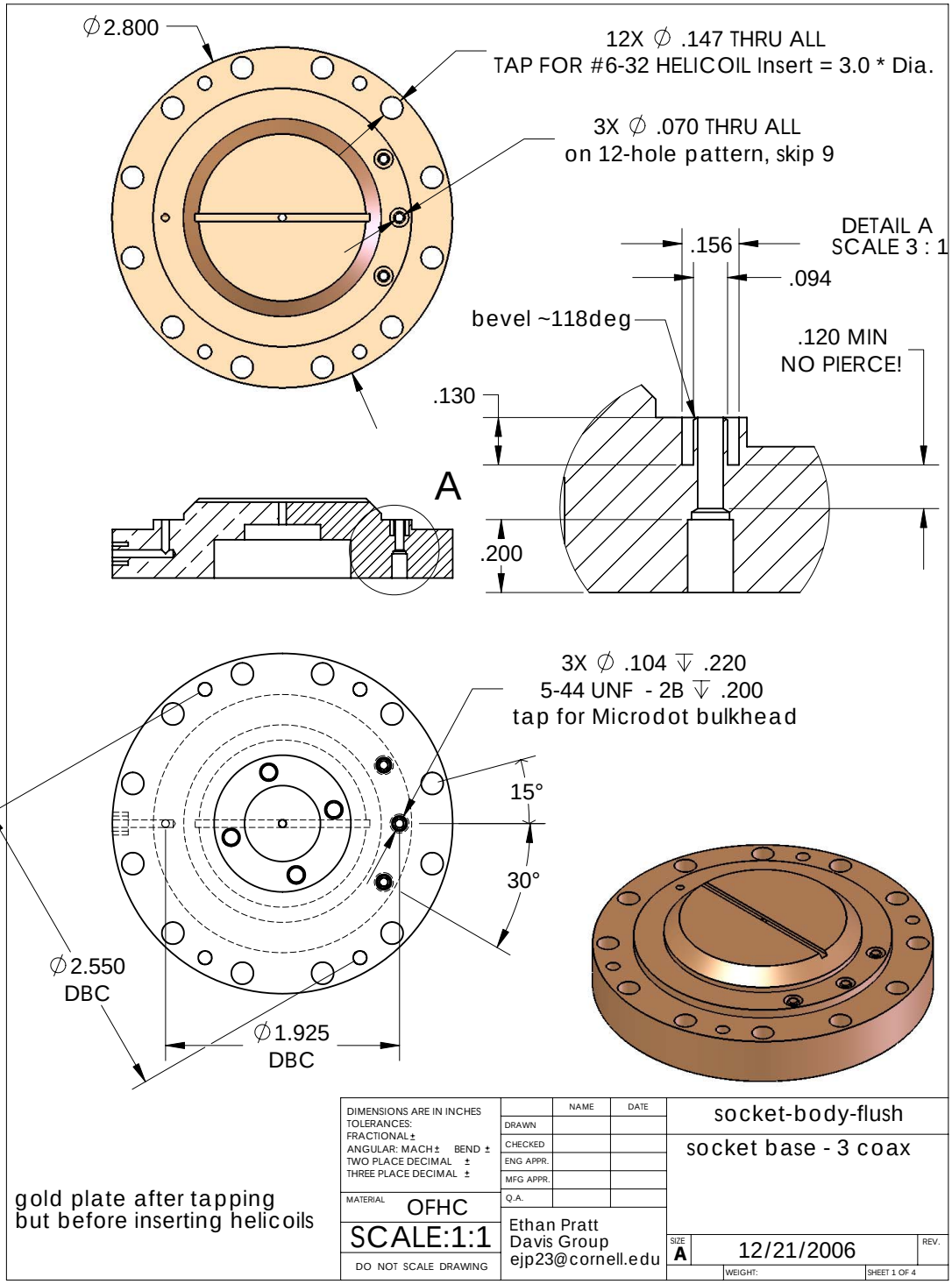

Figure D.5: High pressure cell - view through coax feedthrough.

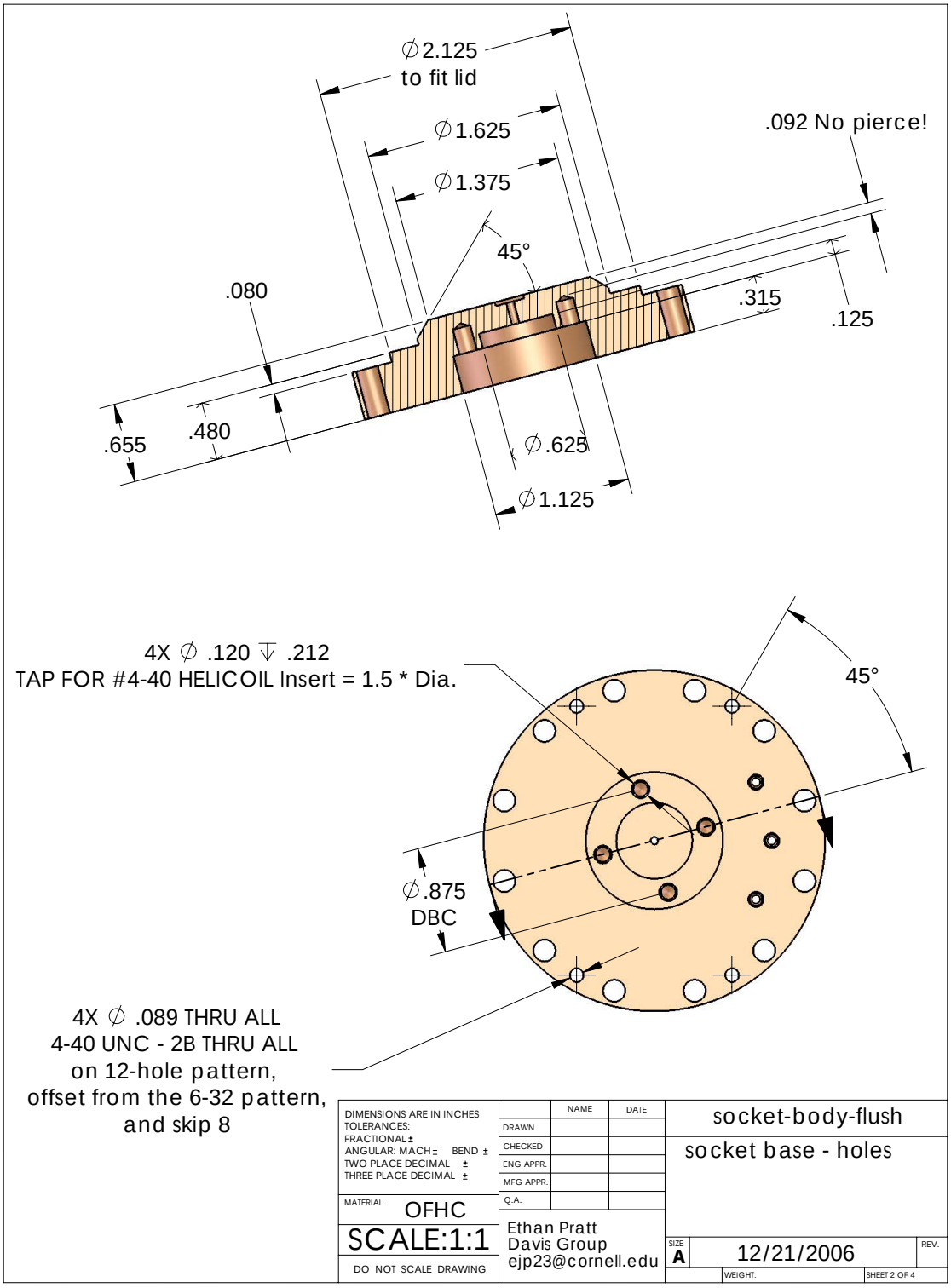

Figure D.6: High pressure cell - view through pressure gauge mounts.

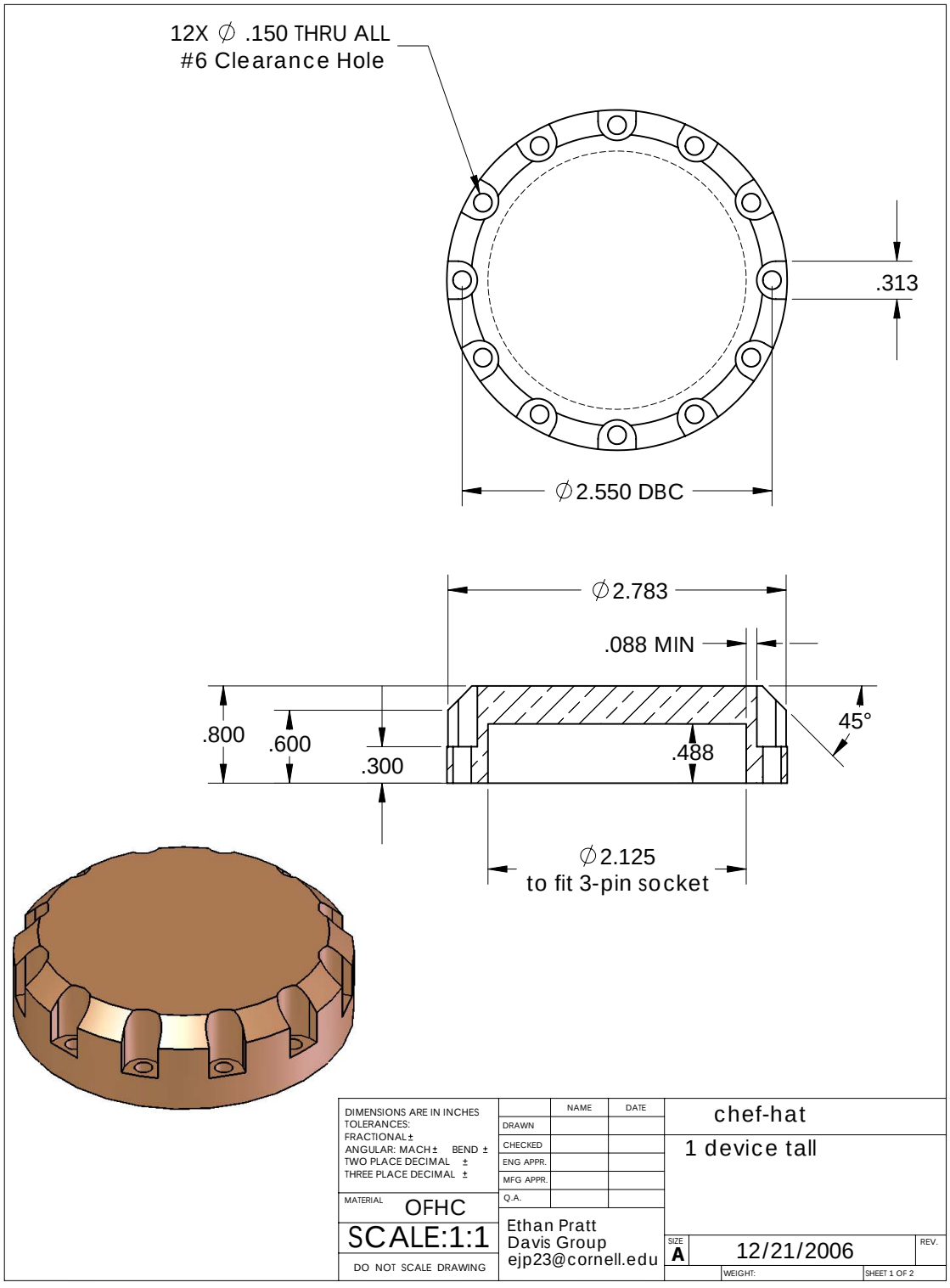

Figure D.7: High pressure screw-down cap (indium-sealed to cell).

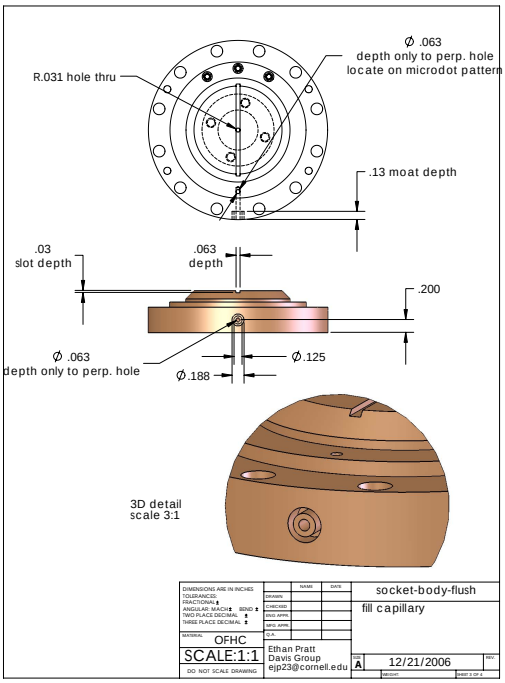

(a) External fill capillary braze boss detail.

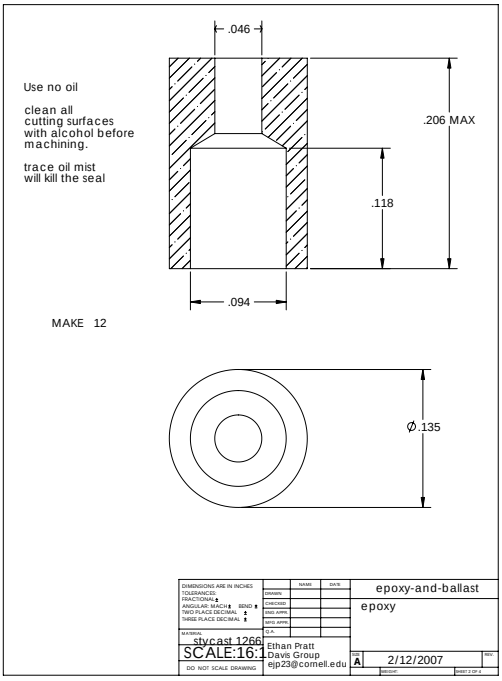

(b) Coax feedthrough component - pre-machined Stycast socket.

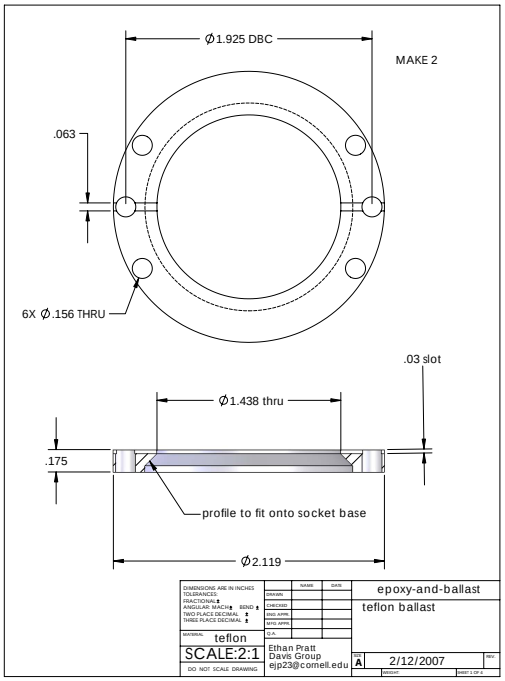

(c) Teflon ballast to reduce helium volume beneath chip carrier.

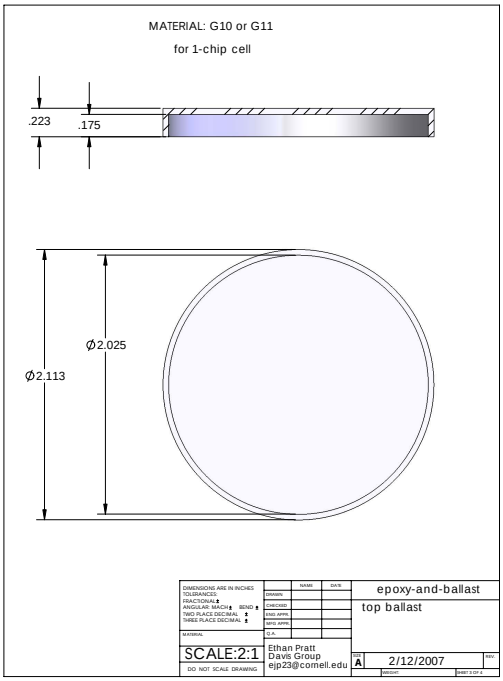

(d) Fiberglass ballast to reduce helium above chip carrier.

Figure D.8: Pressurized cell detail and components.

D.4 Nanoporous chip: cryogenic mounting frame ("gazebo")

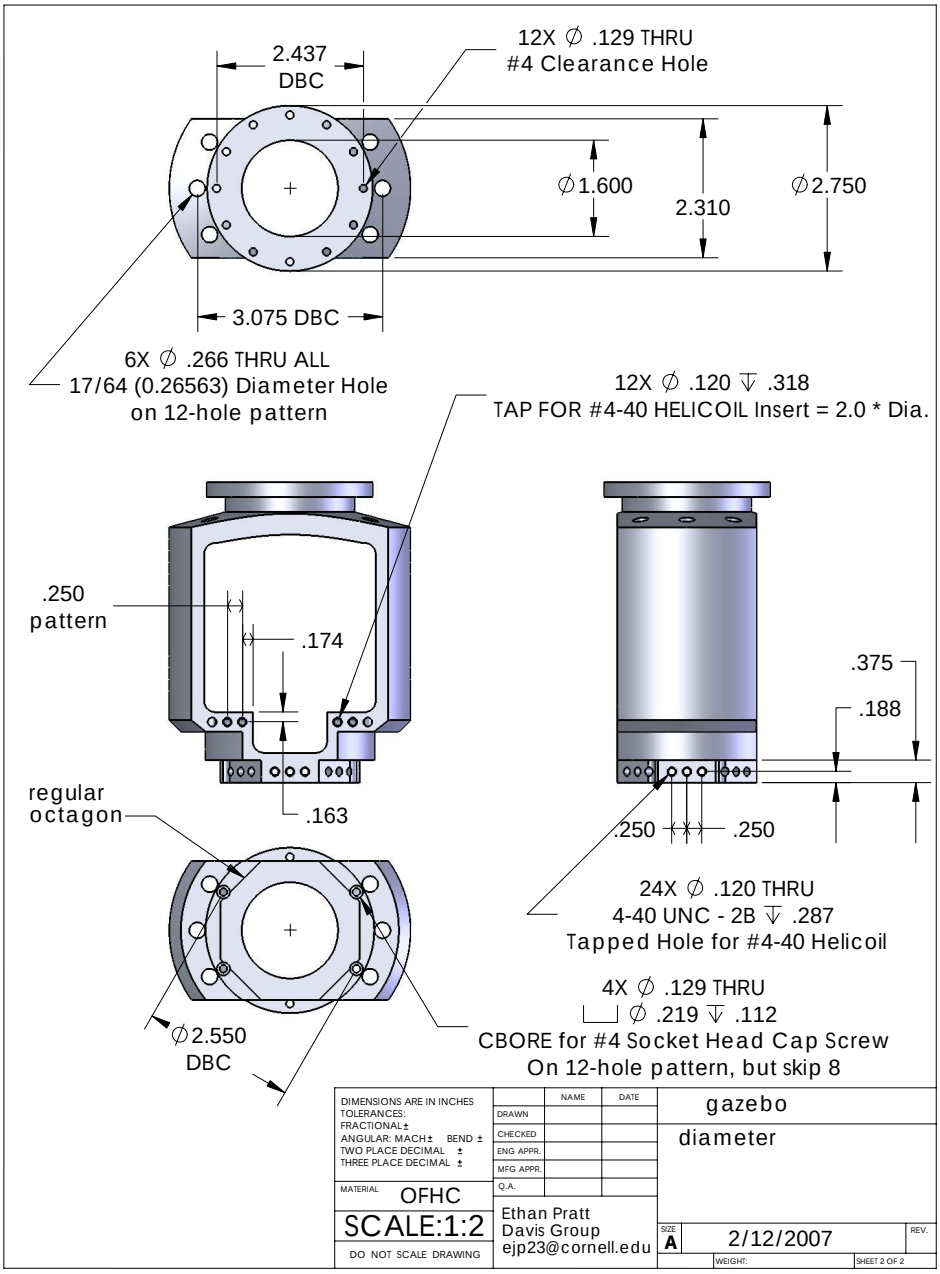

Figure D.9: Mounting platform for mixing chamber. See. Fig. 2.2 on page 11. This platform secures the high-pressure nanoporous cell, and also provides clearance, thermalization, and mounting for the torsion oscillator experiments.

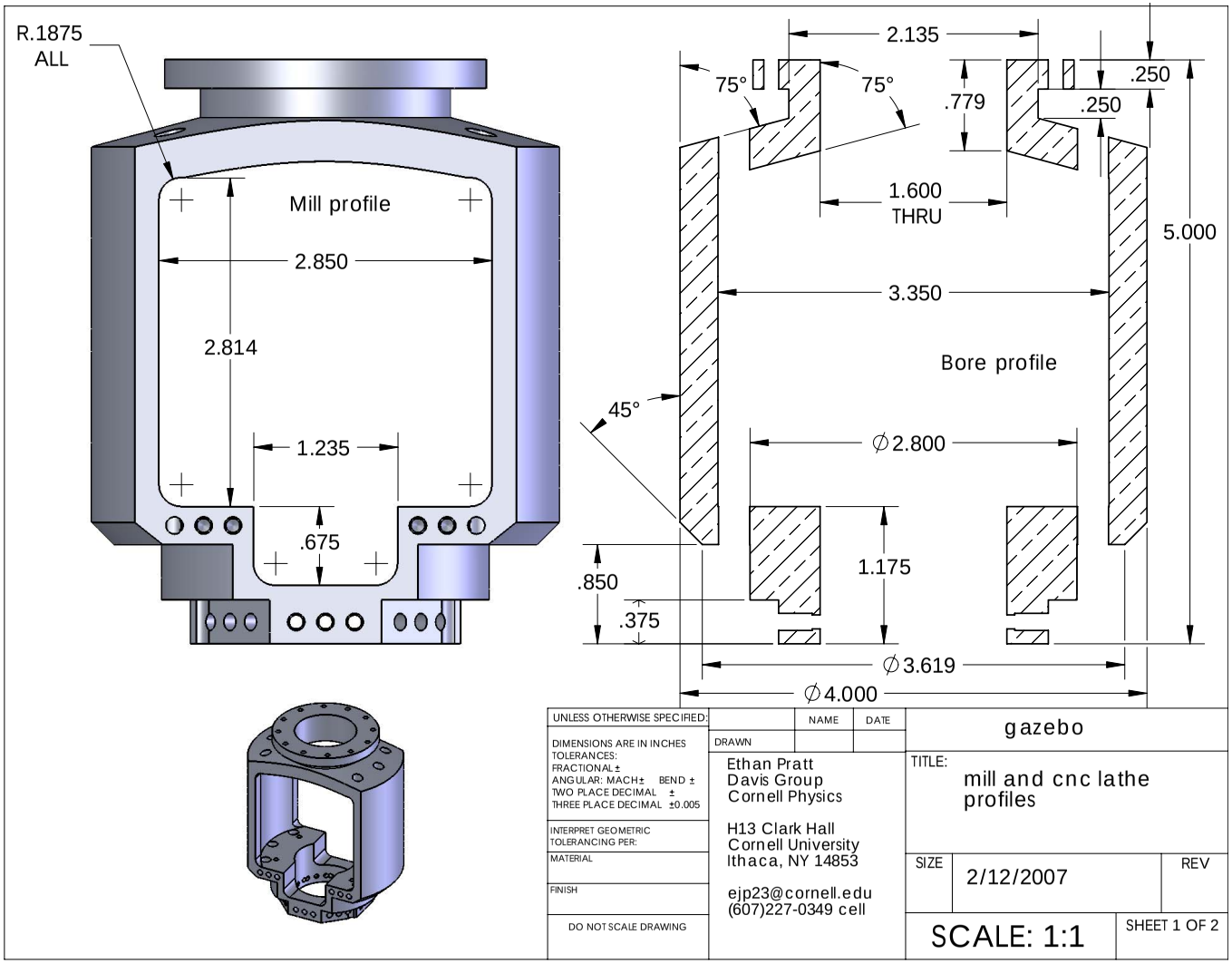

Figure D.10: Gazebo - CNC paths

D.5 Cryogenic capacitive pressure gauge

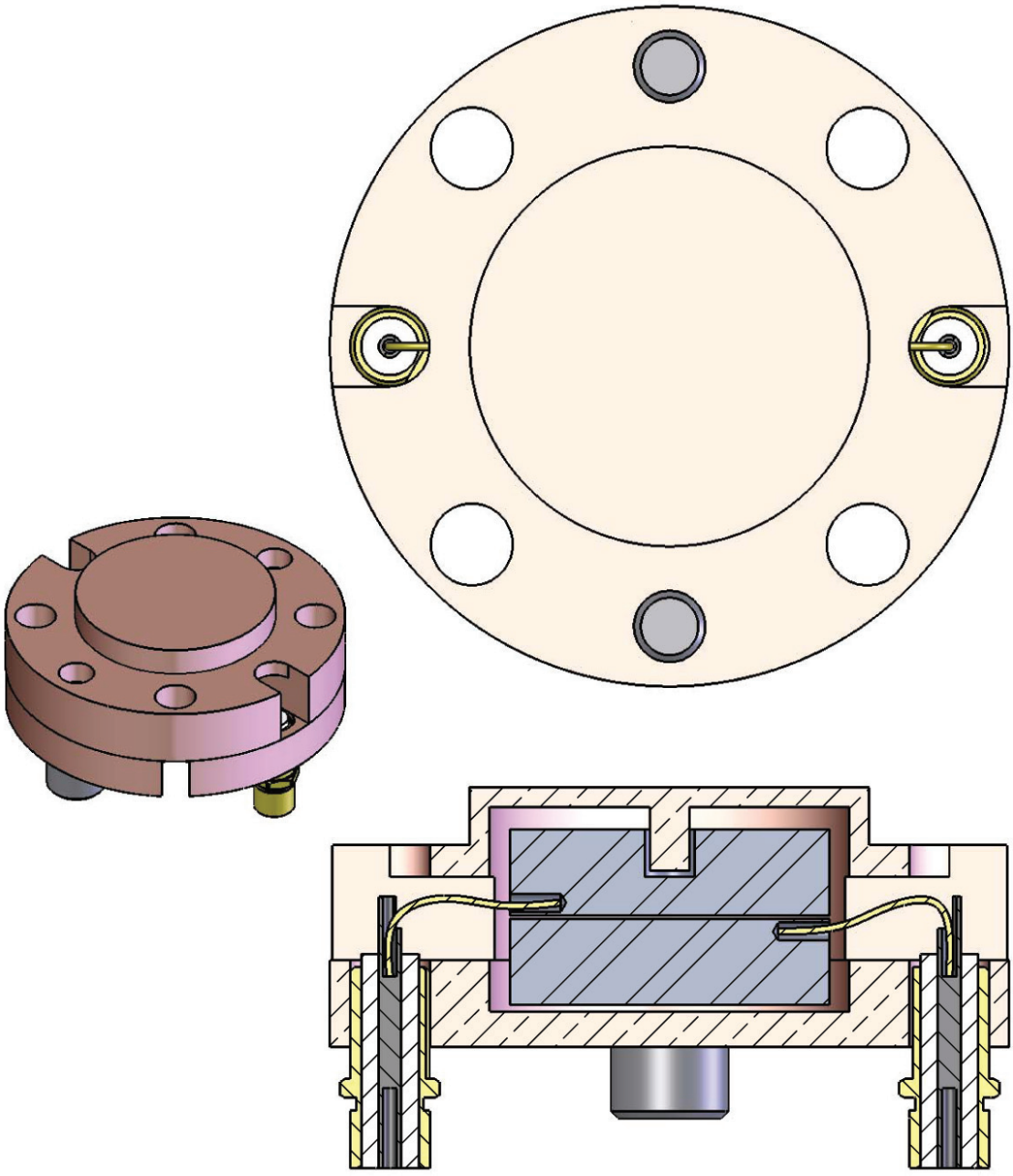

Figure D.11: Overview of assembled Straty-Adams-style pressure gauge. [13]

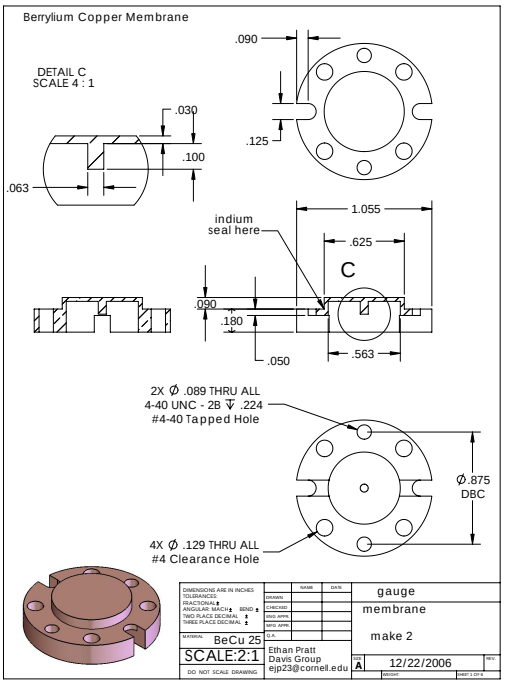

(a) BeCu membrane.

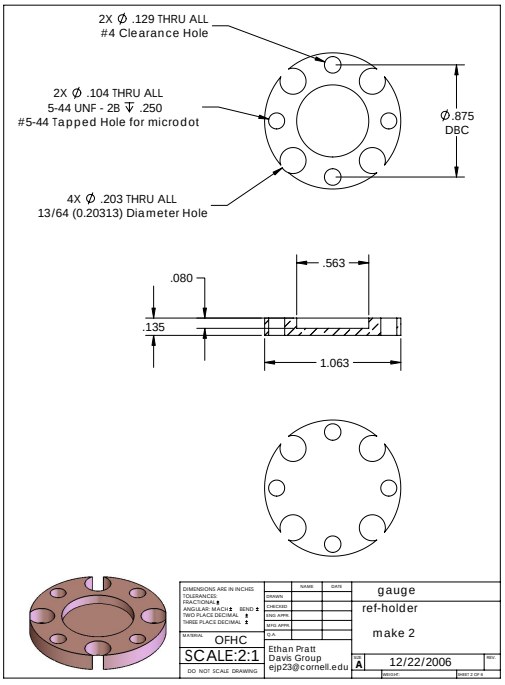

(b) Fixed-electrode chassis.

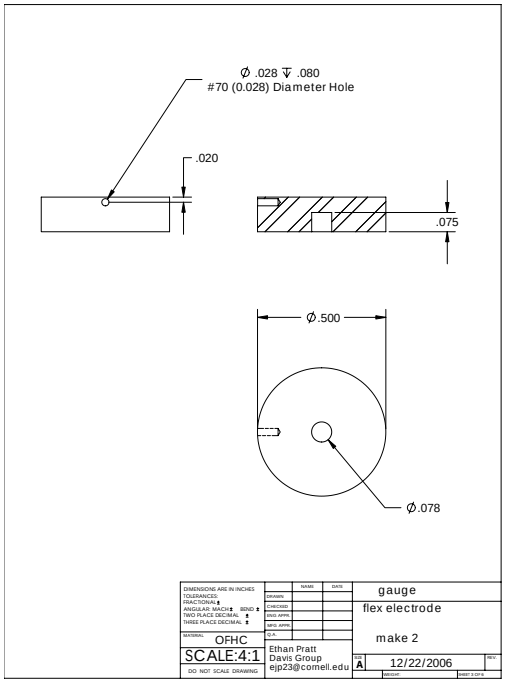

(c) Moving electrode (glued to BeCu membrane post).

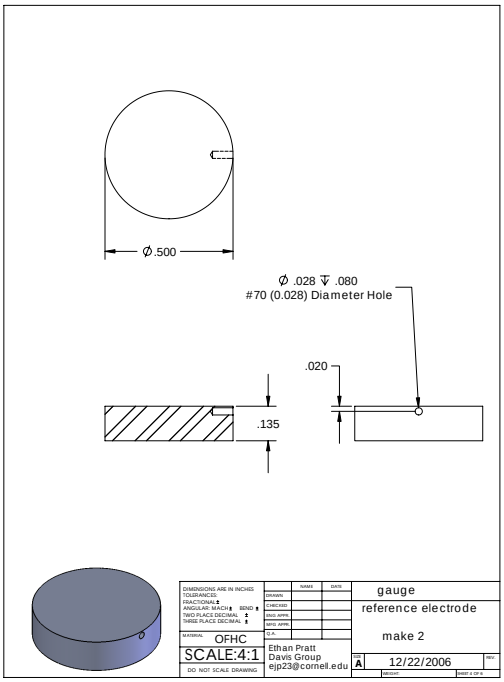

(d) Fixed electrode.

Figure D.12: Components of pressure gauge.

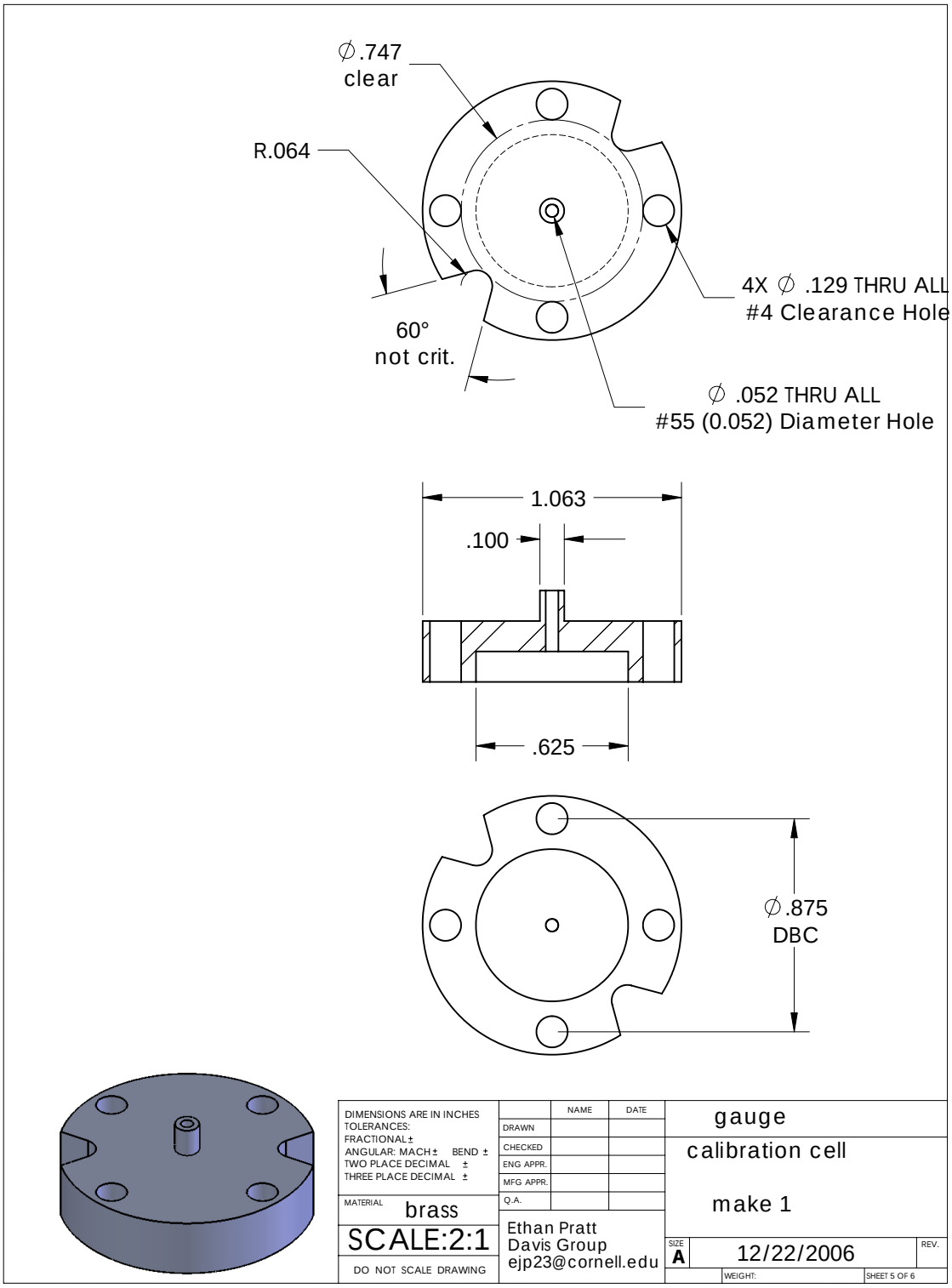

Figure D.13: Dummy cell for assembly and pressure test before final indium-gasket seal into sample cell. After the wires are soldered and electrodes shimmed and glued here, the gauge can be retracted intact from the dummy cell and moved to the experimental cell.

D.6 Liquid nitrogen cold trap

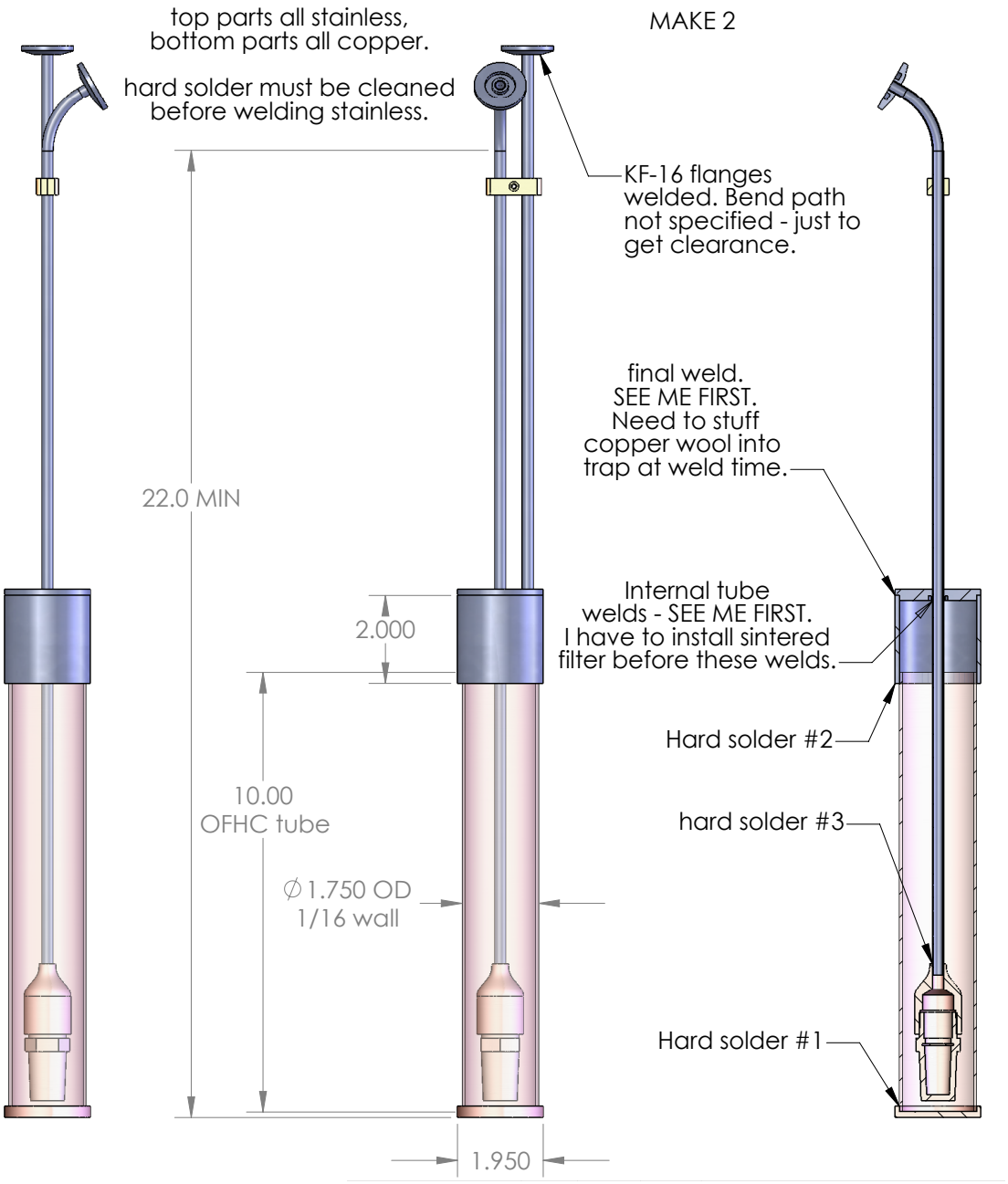

Figure D.14: Liquid nitrogen trap for dilution refrigerator mash. We had previously used traps that suffered from both poor thermalization (so that dirty mash would get through the trap within the first few minutes after insertion into the LN2 dewar), plus leaks through the indium-sealed bottom plate. This trap was designed to have excellent thermal contact between the flowing gas and the trap, and also to eliminate any cryogenic (e.g. indium) o-rings.

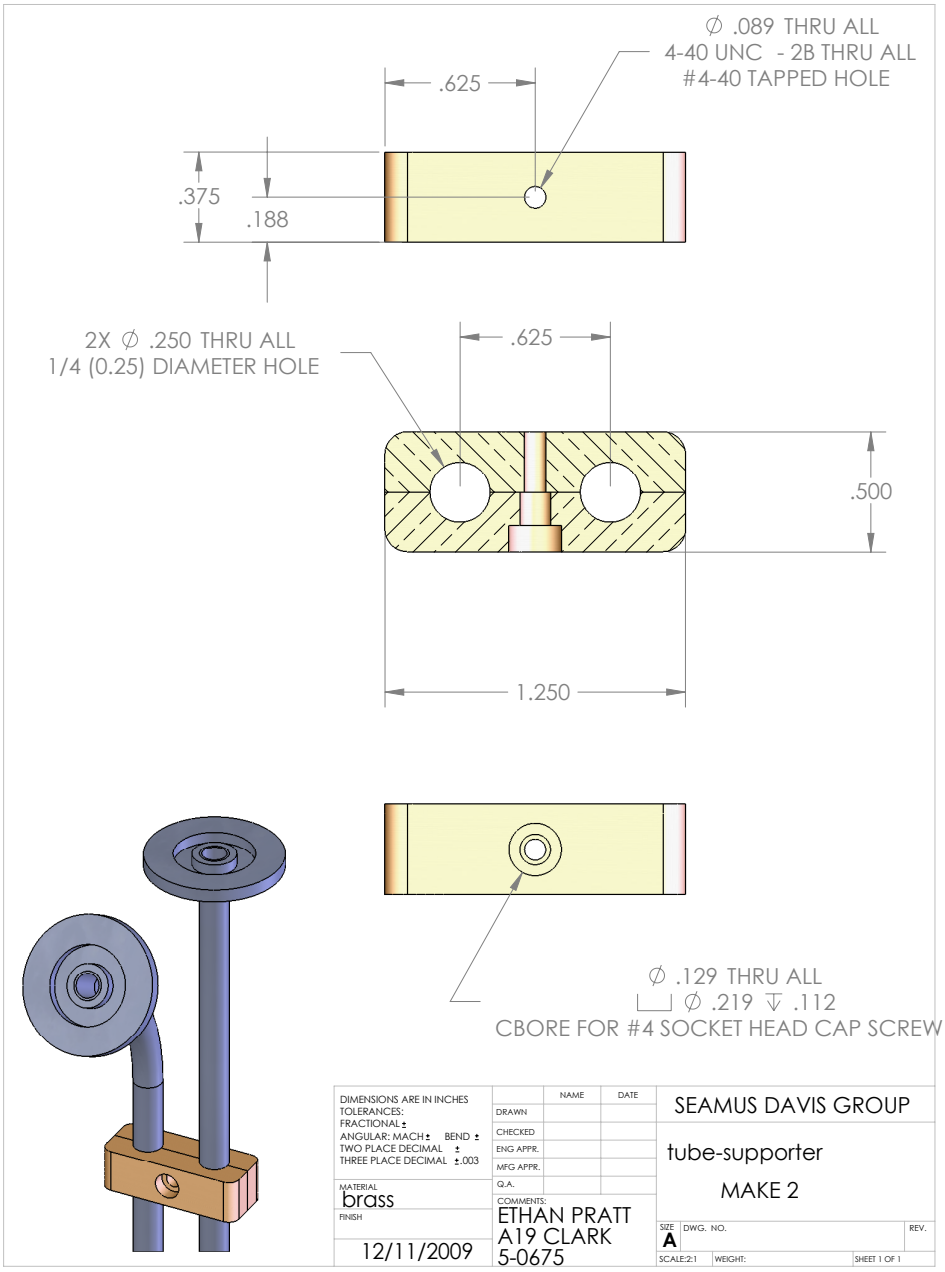

Figure D.15: Tube support collar.

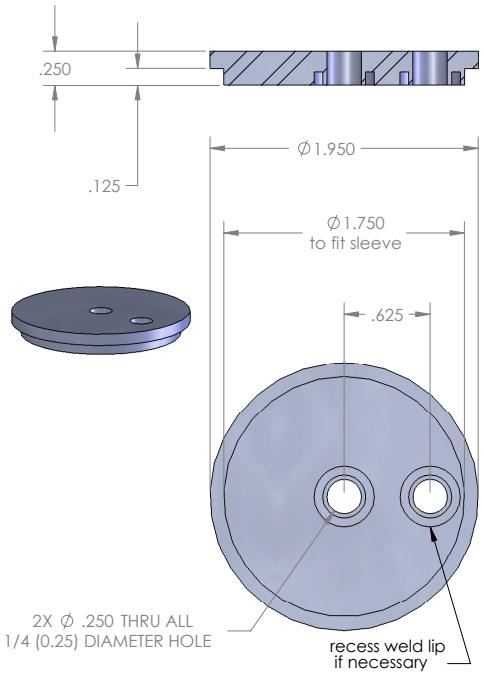

(a) Stainless top cap.

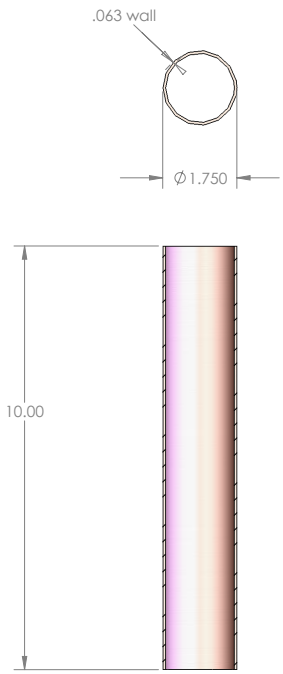

(b) Copper cylinder.

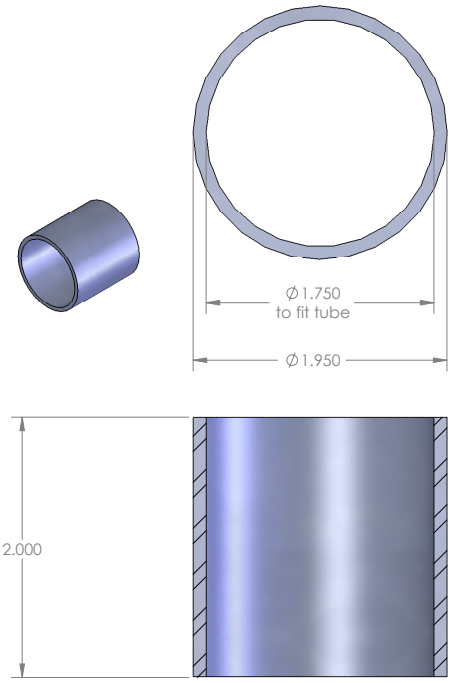

(c) Stainless collar.

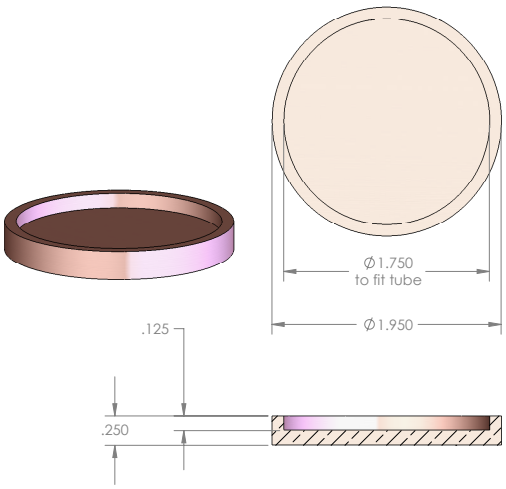

(d) Copper bottom cap.

Figure D.16: Components of the outer trap cylinder. The order of assembly is: hard soldering, cleaning, installing sparger, welding, pouring in copper pellets, pouring in charcoal. The final joint is welded stainless to stainless, so that no hard-soldering is required on captured joints that cannot be cleaned.

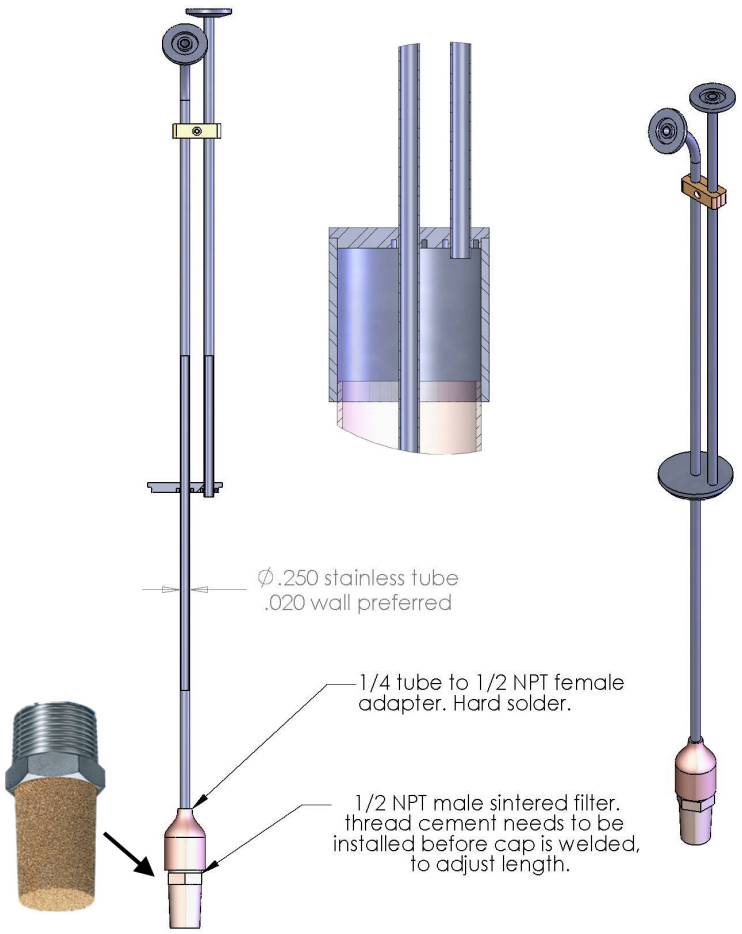

Figure D.17: Liquid nitrogen trap insert, final assembly of which is accomplished by welding the stainless cap to the stainless collar of the outer trap cylinder. The sintered bronze sparger is a SIKA-B J2235 silencer from GKN Sinter Metals (gkn-filters.com) with integrated NPT threads, providing a cold, porous, 80 μm filter path for the gas outlet. (Photograph from the GKN catalog.)

A shallow bed of copper pellets settled in the bottom of the copper cylinder rapidly thermalizes this sintered bronze sparger after immersion of the trap. The cylinder volume above the copper pellet bed is filled with activated charcoal. The copper pellets and charcoal can be poured down the inlet tube *after* the trap is fully assembled and welded (so no indium-sealed access is required).

These features were very successful; if new traps are fabricated based on this design, the only suggested change is to increase the diameter of the inlet tube.

BIBLIOGRAPHY

[1] Steven Brawer. *Relaxation in viscous liquids and glasses : review of phenomenology, molecular dynamics simulations, and theoretical treatment*. American Ceramic Society, 1985.

[2] D. J. Bishop and J. D. Reppy. Study of the superfluid transition in two-dimensional *he*4 films. *Phys. Rev. B*, 22(11):5171–5185, Dec 1980.

[3] G. Agnolet, D.F. McQueeney, and J.D. Reppy. Kosterlitz-thouless transition in helium films. *Physical Review B*, 39:8934–8958, 1989.

[4] R.M. Bowley, A.D. Armour, J. Nyéki, B.P. Cowan, and J. Saunders. Universal features of the superfluid transition of a thin 4he film on an atomically flat substrate. *Journal of Low Temperature Physics*, 113:399–404, 1998.

[5] K. A. Gillis, S. Volz, and J. M. Mochel. Superfluid flow dissipation in two dimensions. *Journal of Low Temperature Physics*, 61:173–183, 1985.

[6] Ian K. Ono, Corey S. O'Hern, D. J. Durian, Stephen A. Langer, Andrea J. Liu, and Sidney R. Nagel. Effective temperatures of a driven system near jamming. *Phys. Rev. Lett.*, 89(9):095703, Aug 2002.

[7] A.S.C. Rittner, W. Choi, E.J. Mueller, and J.D. Reppy. Absence of Pressure-Driven Supersolid Flow at Low Frequency. *Arxiv preprint arXiv:0904.2640*, 2009.

[8] E. Kim and M. H. W. Chan. Observation of Superflow in Solid Helium. *Science*, 305(5692):1941–1944, 2004.

[9] Cao Lie-zhao, D. F. Brewer, C. Girit, E. N. Smith, and J. D. Reppy. Flow and torsional oscillator measurements on liquid helium in restricted geometries under pressure. *Phys. Rev. B*, 33(1):106–117, Jan 1986.

[10] James Day and John Beamish. Low-temperature shear modulus changes in solid 4he and connection to supersolidity. *Nature*, 450(7171):853–856, 12 2007.

[11] A. C. Clark, J. T. West, and M. H. W. Chan. Nonclassical rotational inertia in helium crystals. *Physical Review Letters*, 99(13):135302, 2007.

[12] S. Yang, P.A. Mirau, C.S. Pai, O. Nalamasu, E. Reichmanis, J.C. Pai, Y.S. Obeng, J. Seputro, E.K. Lin, H.J. Lee, Jianing Sun, and David W. Gidley. Nanoporous ultralow dielectric constant organosilicates templated by triblock copolymers. *Chem. Mater*, 14(1):369–374, 2002.

[13] G. C. Straty and E. D. Adams. Highly sensitive capacitive pressure gauge. *Review of Scientific Instruments*, 40(11):1393–1397, 1969.

[14] T. Timusk and B. Statt. The pseudogap in high-temperature superconductors: an experimental survey. *Reports on Progress in Physics*, 62:61–122, 1999.

[15] D.J. Thouless. The flow of a dense superfluid. *Annals of Physics*, 52:403–427, 1969.

[16] A. F. Andreev and I. M. Lifshitz. Quantum theory of defects in crystals. *Soviet Physics JETP-USSR*, 29(6):1107, 1969.

[17] L. Reatto. Bose-einstein condensation for a class of wave functions. *Phys. Rev.*, 183(1):334–338, Jul 1969.

[18] G. V. Chester. Speculations on bose-einstein condensation and quantum crystals. *Phys. Rev. A*, 2(1):256–258, Jul 1970.

[19] A. J. Leggett. Can a solid be "superfluid"? *Phys. Rev. Lett.*, 25(22):1543–1546, Nov 1970.

[20] Mark W. Meisel. Supersolid 4he: an overview of past searches and future possibilities. *Physica B: Condensed Matter*, 178(1-4):121 – 128, 1992. Proceedings of the Korber Symposium on Superfluid 3He in Rotation.

[21] D.R. Tilley and J. Tilley. *Superfluidity and Superconductivity*. Taylor and Francis, 1 edition, 1990.

[22] D. S. Greywall. Search for superfluidity in solid *he*4. *Phys. Rev. B*, 16:1291–1292, 1977.

[23] P. G. van de Haar, C. M. C. M. van Woerkens, M. W. Meisel, and G. Frossati. An experiment to detect vacancies and their possible bose-einstein condensation in solid 4he. *Journal of Low Temperature Physics*, 86:349, 1992.

[24] Gabriel A. Lengua and John M. Goodkind. Elementary excitations and a

collective mode in hcp4he. *Journal of Low Temperature Physics*, 79:251–287, 1990.

[25] D. J. Bishop, M. A. Paalanen, and J. D. Reppy. Search for superfluidity in hcp [*sup*4]*he*. *Physical Review B (Condensed Matter)*, 24(5):2844–2845, 1981.

[26] E. Kim and M. H. W. Chan. Probable observation of a supersolid helium phase. *Nature*, 427(6971):225–227, 2004.

[27] Ann Sophie C. Rittner and John D. Reppy. Observation of classical rotational inertia and nonclassical supersolid signals in solid [sup 4]he below 250 mk. *Physical Review Letters*, 97(16):165301, 2006.

[28] Y. Aoki, J. C. Graves, and H. Kojima. Oscillation frequency dependence of nonclassical rotation inertia of solid [sup 4]he. *Physical Review Letters*, 99(1):015301, 2007.

[29] Andrey Penzev, Yoshinori Yasuta, and Minoru Kubota. Annealing effect for supersolid fraction in 4he. *Journal of Low Temperature Physics*, 148:677–681, 2007.

[30] Motoshi Kondo, Shunichi Takada, Yoshiyuki Shibayama, and Keiya Shirahama. Observation of non-classical rotational inertia in bulk solid 4he. *Journal of Low Temperature Physics*, 148:695–699, 2007.

[31] E. Kim, J. S. Xia, J. T. West, X. Lin, A. C. Clark, and M. H. W. Chan. Effect of he-3 impurities on the nonclassical response to oscillation of solid he-4. *Physical Review Letters*, 100(6):065301, 2008.

[32] S. Sasaki, R. Ishiguro, F. Caupin, H. J. Maris, and S. Balibar. Superfluidity of Grain Boundaries and Supersolid Behavior. *Science*, 313(5790):1098–1100, 2006.

[33] James Day and John Beamish. Pressure-driven flow of solid helium. *Physical Review Letters*, 96(10):105304, 2006.

[34] M. W. Ray and R. B. Hallock. Observation of unusual mass transport in solid hcp [sup 4]he. *Physical Review Letters*, 100(23):235301–4, 06 2008/06/13/.

[35] A. C. Clark, J. D. Maynard, and M. H. W. Chan. Thermal history of solid

he-4 under oscillation. *Physical Review B (Condensed Matter and Materials Physics)*, 77(18):184513, 2008.

[36] Z. Nussinov, A. V. Balatsky, M. J. Graf, and S. A. Trugman. Origin of the decrease in the torsional-oscillator period of solid [sup 4]he. *Physical Review B (Condensed Matter and Materials Physics)*, 76(1):014530, 2007.

[37] A.F. Andreev. Supersolidity of glasses. *JETP Letters*, 85:585–587, 2007.

[38] S.E. Korshunov. Two-level systems and mass deficit in quantum solids. page arXiv:0906.4627v2, 2009.

[39] P. W. Anderson. Two new vortex liquids. *Nat Phys*, 3(3):160–162, 03 2007/03//print.

[40] P. W. Anderson. Bose fluids above t[sub c]: Incompressible vortex fluids and "supersolidity". *Physical Review Letters*, 100(21):215301, 2008.

[41] L. Pollet, M. Boninsegni, A. B. Kuklov, N. V. Prokof'ev, B. V. Svistunov, and M. Troyer. Superfluidity of grain boundaries in solid [sup 4]he. *Physical Review Letters*, 98(13):135301, 2007.

[42] C.-D. Yoo and Alan T. Dorsey. Theory of viscoelastic behavior of solid [sup 4]he. *Physical Review B (Condensed Matter and Materials Physics)*, 79(10):100504, 2009.

[43] Massimo Boninsegni, Nikolay Prokof'ev, and Boris Svistunov. Superglass phase of [sup 4]he. *Physical Review Letters*, 96(10):105301, 2006.

[44] Jiansheng Wu and Philip Phillips. Minimal model for disorder-induced missing moment of inertia in solid [sup 4]he. *Physical Review B (Condensed Matter and Materials Physics)*, 78(1):014515, 2008.

[45] Jacques Bossy, Jonathan V. Pearce, Helmut Schober, and Henry R. Glyde. Excitations of nanoscale quantum liquids under pressure and the bose glass phase. *Physical Review B*, 78:224507, 2008.

[46] Giulio Biroli, Claudio Chamon, and Francesco Zamponi. Theory of the superglass phase. *Physical Review B (Condensed Matter and Materials Physics)*, 78(22):224306, 2008.

[47] Joshua T. West, Oleksandr Syshchenko, John Beamish, and Moses H. W. Chan. Role of shear modulus and statistics in the supersolidity of helium. *Nature Physics*, 5:598–601, 2009.

[48] James Day, Oleksandr Syshchenko, and John Beamish. Intrinsic and dislocation-induced elastic behavior of solid helium. *PHYSICAL REVIEW B*, 79(21), JUN 2009.

[49] Ann Sophie C. Rittner and John D. Reppy. Probing the upper limit of nonclassical rotational inertia in solid helium 4. *Physical Review Letters*, 101(15):155301, 2008.

[50] J. T. West, X. Lin, Z. G. Cheng, and M. H. W. Chan. Supersolid behavior in confined geometry. *Physical Review Letters*, 102(18):185302, 2009.

[51] Janis research company.

[52] J. Clarke and A. Braginski, editors. *The SQUID Handbook, vol. 1*, volume 1. Wiley-VCH, 2004.

[53] Y. Aoki, M. C. Keiderling, and H. Kojima. New dissipation relaxation phenomenon in oscillating solid [sup 4]he. *Physical Review Letters*, 100(21):215303, 2008.

[54] V. N. Grigor'ev, V. A. Maidanov, V. Yu. Rubanskii, S. P. Rubets, E. Ya. Rudavskii, A. S. Rybalko, Ye. V. Syrnikov, and V. A. Tikhii. Observation of a glassy phase of [sup 4]he in the region of supersolid effects. *Physical Review B (Condensed Matter and Materials Physics)*, 76(22):224524–6, 12 2007/12/01/.

[55] Pei-Chun Ho, Ian P. Bindloss, and John M. Goodkind. A new anomaly in solid 4he. *Journal of Low Temperature Physics*, 109:409–421, 1997.

[56] B. K. P. Scaife. *Principles of dielectrics*. Clarendon Press and Oxford University Press, 1989.

[57] Kenneth S. Cole and Robert H. Cole. Dispersion and absorption in dielectrics i. alternating current characteristics. *The Journal of Chemical Physics*, 9(4):341–351, 1941.

[58] D. W. Davidson and R. H. Cole. Dielectric relaxation in glycerol, propylene

glycol, and n-propanol. *The Journal of Chemical Physics*, 19(12):1484–1490, 1951.

[59] R. M. Bowley, A. D. Armour, and K. A. Benedict. Refinement of the dynamic theory of superfluid helium films. *Journal of Low Temperature Physics*, 113:71–87, 1998.

[60] Nobutaka Shimizu, Yoshinori Yasuta, and Minoru Kubota. Possible vortex fluid to supersolid transition in solid 4he below 75 mk. *arXiv Preprint*, 0903.1326v3, 2009.

[61] A.F. Andreev. Momentum deficit in quantum glasses. *arXiv Preprint*, 0809.1990v2, 2009.

[62] Vinay Ambegaokar, B. I. Halperin, David R. Nelson, and Eric D. Siggia. Dynamics of superfluid films. *Phys. Rev. B*, 21(5):1806–1826, Mar 1980.

[63] Vinay Ambegaokar, B. I. Halperin, David R. Nelson, and Eric D. Siggia. Dissipation in two-dimensional superfluids. *Phys. Rev. Lett.*, 40(12):783–786, Mar 1978.

[64] D. J. Bishop and J. D. Reppy. Study of the superfluid transition in two-dimensional *he*4 films. *Phys. Rev. Lett.*, 40(26):1727–1730, Jun 1978.

[65] Sergio Gaudio, Emmanuele Cappelluti, Gianluca Rastelli, and Luciano Pietronero. Finite-size berezinskii-kosterlitz-thouless transition at grain boundaries in solid [sup 4]he and the role of [sup 3]he impurities. *Physical Review Letters*, 101(7):075301, 2008.

[66] Benjamin Hunt, Ethan Pratt, Vikram Gadagkar, Minoru Yamashita, Alexander V. Balatsky, and J. C. Seamus Davis. Evidence for a superglass state in solid 4he. *Science*, 324(5927):632–636, 2009.

[67] M. J. Graf, Z. Nussinov, and A. V. Balatsky. The glassy response of solid he-4 to torsional oscillations. *Journal of Low Temperature Physics*, (not yet published), 2009.

[68] L. Pollet, M. Boninsegni, A. B. Kuklov, N. V. Prokof'ev, B. V. Svistunov, and M. Troyer. Local stress and superfluid properties of solid [sup 4]he. *Physical Review Letters*, 101(9):097202, 2008.

[69] J. M. Parpia and J. D. Reppy. Critical velocities in superfluid *he*3. *Phys. Rev. Lett.*, 43(18):1332–1336, Oct 1979.

[70] Massimo Pica Ciamarra and Antonio Coniglio. Jamming at zero temperature, zero friction, and finite applied shear stress. *Physical Review Letters*, 103(23):235701, 2009.

[71] S. I. Shevchenko. One-dimensional superfluidity in bose crystals. *Soviet Journal of Low Temperature Physics*, 13:61, 1987.

[72] S.I. Shevchenko. Quasi-one-dimensional superfluidity in bose systems. *Soviet Journal of Low Temperature Physics*, 14:1011–1027, 1988.

[73] D.V. Fil and S.I. Shevchenko. Bose einstein condensation in a decorated lattice - an application to the problem of supersolid he. *Low Temperature Physics*, 34:351–356, 2008.

[74] C.P. Lindsey and G.D. Patterson. Detailed comparison of the williams-watts and cole-davidson functions. *J. Chem. Phys*, 73:3348–3357, 1980.

[75] Ben Hunt. personal communication.

[76] John Beamish. personal communication.

[77] Jung-Jung Su, Matthias J. Graf, and Alexander V. Balatsky. A glassy contribution to the heat capacity of hcp 4he solids. *Journal of Low Temperature Physics*, (to be published), 2009.

[78] D. G. Fesko and N. W. Tschoegl. Time-temperature superposition in thermorheologically complex materials. *Journal of Polymer Science Part C: Polymer Symposia*, 35:51–69, 1971.

[79] A. V. Balatsky, M. J. Graf, Z. Nussinov, and S. A. Trugman. Entropy of solid [sup 4]he: The possible role of a dislocation-induced glass. *Physical Review B (Condensed Matter and Materials Physics)*, 75(9):094201, 2007.

[80] John Toner. Quenched dislocation enhanced supersolid ordering. *Physical Review Letters*, 100(3):035302, 2008.

[81] M. Boninsegni, A. B. Kuklov, L. Pollet, N. V. Prokof'ev, B. V. Svistunov, and M. Troyer. Luttinger liquid in the core of a screw dislocation in helium-4. *Physical Review Letters*, 99(3):035301, 2007.

[82] A.C. Clark and M.H.W. Chan. Specific heat of solid helium. *Journal of Low Temperature Physics*, 138:853–858, 2005.

[83] X. Lin, A. C. Clark, and M. H. W. Chan. Probable heat capacity signature of the supersolid transition. *Nature*, 449(7165):1025–1028, 2007.

[84] X. Lin, A. C. Clark, Z. G. Cheng, and M. H. W. Chan. Heat capacity peak in solid [sup 4]he: Effects of disorder and [sup 3]he impurities. *Physical Review Letters*, 102(12):125302, 2009.

[85] PL Gammel, HE Hall, and JD Reppy. Persistent Currents in Superfluidˆ{3} He-B. *Physical Review Letters*, 52(2):121–124, 1984.

[86] JP Pekola, JT Simola, KK Nummila, OV Lounasmaa, and RE Packard. Persistent-Current Experiments on Superfluidˆ{3} He-B andˆ{3} He-A. *Physical Review Letters*, 53(1):70–73, 1984.

[87] Charles Boghosian and Horst Meyer. Density, coefficient of thermal expansion, and entropy of compression of liquid he4 under pressure below 1.4°k. *PHYSICAL REVIEW*, 152:200–206, 1966.